

Facultad de Física  
Departamento de Física Atómica, Molecular y Nuclear



VNIVERSITAT  
DE VALÈNCIA

# TRITIUM: Design, Construction and Commissioning of an In-Water Tritium Detector

Marcos Martínez Roig

PhD in Physics  
April 19, 2021

Under the supervision of:

José Díaz Medina  
Nadia Yahlali Haddou



*Dedicated to  
my family*

Sometimes it is the people no one imagines anything  
of who do the things that no one can imagine.

"Alan Turing"

I



# Acknowledgements

Al echar la mirada atrás a estos años de trabajo y formación como investigadora, siento que ha habido muchas personas que me han ayudado directa o indirectamente en esta aventura, por lo que no puede faltar este espacio para agradecer la ayuda que he recibido.

Durante estos 4 años han sido muchas las personas que me han ayudado. Espero no dejarme a nadie.

Ver memoria de "Detectores monolíticos y sensores compatibles con altos campos magnéticos para tomografía por emisión de positrones"

AGRADECER A:

- Gente de tritium Valencia: PEPE, NADIA, MIREIA, ANA, MARQUITOS, ANDREA.
- Gente del LARAM -> TERESA, VANESA, ROSA, CLODO
- Gente de Tritium -> GENTE DE PORTUGAL, Antonio y Jose Angel de extremadura, gente de francia...
- Gente que ha aportado al trabajo:
  - Gente de DUNE (Anselmo, Miguel, Justo)
  - Gente de NEXT (Vicente, Marc, Javier, la chica, etc...)

- Ingeniero electrónico David Calvo del IFIC
  - Gente del IFIMED (Ana Ros, Jhon Barrio y Gabriela Llosa del IFIMED, Rita, Jorge, Marina)
  - Gente de Espectrometría Gamma (El hombre y su mujer, Cesar, Ion, el doctorado, etc)
  - Gente de ATLAS (Urmila, Carlos Mariñas)
  - Gente del ICMOL (El que manda, Lidon)
  - Departamento de mecánica del IFIC (Manolo "Apellidos", Jose Luis Jordan, Jose Vicente Civera Navarrete, Tchogna Davis, Daniel)
  - departamento de electrónica del IFIC (Jorge Nacher Arándiga, Manu ... y el otro )
  - Al departamento de informática (gente)
- Gente externa que ha ayudado
    - DAVID CANAL DE SAMTEC
    - A LUIS FERR... DE PETSYS..
  - Gente externa que no ha ayudado
    - Grupo de amigos del IFIC (nombrar a todos, tanto en el master como en el doctorado)
    - Familia
    - Amigos del pueblo
  - Al programa interreg sudoe -> Soporte financiero!

# Abstract

Tritium is one of the most frequently emitted radioisotopes in a nuclear power plant. Large quantities of tritium are normally produced in the water of their cooling system, which are finally emitted to the environment. Due to the fact that high quantities of tritium could be dangerous for human health and for the environment, there exist several legislations around the world which try to control this radioactive emissions in each country, like the Directive Europeen 2013/51/Euratom, which establishes the tritium limit in drinking water in Europe at 100 Bq/L, or the U. S. Environmental Protection Agency, in United States, whose tritium limit in drinking water is established at 740 Bq/L.

Nowadays, due to such a low energy emitted in the tritium decay, we need high sensitive detectors for measuring it like LSC. The problem with LSC is that it is a off-line method whose measurement process can take up to 3 or 4 days, too much time if there are any problem with the NPP.

Detectors based on solid scintillators is a promissing idea for building a tritium detector that works in quasi-real time. This type of detectors has been developed so far succesfully but without achieving enough sensibility for measuring the legal limits.

In this study the results of TRITIUM project is presented. In the

framework of this project we have developed a quasi-real time monitor for low tritium activities in water. This monitor is based on a tritium detector that contains several detection cells which we read in parallel, several active vetos and a passive shielding for reduce the natural background of our system and an ultrapure water system to prepare the sample before we measure. Each detection cell is made up of hundreds of scintillating fibers read out by PMTs or SiPM arrays.

The final objective of this monitor will be the radiological protection around the nuclear power plant. This monitor will provide an alarm in case of an unexpected tritium release. It will be included in the early alarm system of Extremadura consisting of several detectors whose objective is to reduce the impact of Nuclear Power Plants to the environment.

**Keywords:** Tritium in water, Real-time monitor, Nuclear Power Plant, ENvironmental Safety, ...

# Nomenclature and Acronyms

Acronyms:

<i>ICRU</i>	— International Commission of Radioactivity Units and Measurements
<i>ICRP</i>	— International Commission on Radiological Protection
<i>ISR</i>	— International Society of Radiology
<i>UNSCEAR</i>	— United Nations Scientific Committee on the Effects of Atomic Radiation
<i>IAEA</i>	— International Atomic Energy Agency
<i>UN</i>	— United Nations
<i>EU</i>	— European Union
<i>EURATOM</i>	— European Atomic Energy Community
<i>CSN</i>	— Nuclear Safety Council
<i>REA</i>	— Network of automatic stations
<i>REM</i>	— Network of sampling stations
<i>quasi-real</i>	— Less than 10 minutes
<i>LSC</i>	— Liquid Scintillation Counting
<i>PMT</i>	— PhotoMultiplier Tub
<i>SiPM</i>	— Silicon PhotoMultiplier
<i>NPP</i>	— Nuclear Power Plants
<i>U.S.DOE</i>	— United States Department of Energy
<i>U.S.</i>	— United States
<i>PWR</i>	— Pressurized Water Reactor

<i>BWR</i>	— Boiled Water Reactor
<i>HWR</i>	— Heavy Water Reactor
<i>GCR</i>	— Gas-Cooled Reactor
<i>USA</i>	— United States of America
<i>LARAM</i>	— Laboratorio de Radiactividad Ambiental
<i>WHO</i>	— World Health Organization
<i>ALARA</i>	— As Low As Reasonably Achievable
<i>GL</i>	— Guideline
<i>EPA</i>	— Environmental Protection Agency
<i>LDL</i>	— Lower Detection Limit
<i>IC</i>	— Ionization Chamber
<i>BIXS</i>	— Beta Induced X-ray Spectrometry
<i>SDD</i>	— Silicon Drift Detector
<i>APD</i>	— Avalanche Photodiode
<i>EEC</i>	— European Economic Community
<i>CNRS</i>	— Le Centre National de la Recherche Scientifique, France
<i>PHWR</i>	— Pressurized Heavy Water Reactor
<i>UDL</i>	— Upper Detection Limit
<i>LWR</i>	— Liquid Water Reactor
<i>PMMA</i>	— Polymethyl Methacrylates
<i>CCD</i>	— Charge-Coupled Device
<i>HV</i>	— High Voltage
<i>QE</i>	— Quantum Efficiency
<i>CE</i>	— Collection Efficiency
<i>MPPC</i>	— Multi-Pixel Photon Counter
<i>G – APD</i>	— Geiger Avalanche Photodiode
<i>SSPM</i>	— Solid State PhotoMultiplier
<i>MRS – ADP</i>	— Metal-Resistor-Semiconductor Avalanche Photodiode
<i>MAPD</i>	— Micro-Pixel Avalanche Photodiode
$\lambda$	— Wavelength
$\lambda_p$	— Wavelength at which we have the maximum of the associated spectrum

$PDE$	— Photodetection Efficiency of the SiPM
$C_t$	— Terminal Capacitance of the SiPM
$G_{SiPM}$	— Gain of the SiPM
$V_{BR}$	— Breakdown Voltage of the SiPM
$\Delta TV_{op}$	— Temperature Coefficient (mV/ $^{\circ}C$ )
$q_e$	— Electron Charge
$\sigma_T$	— Total Uncertainty of the Measurement
$\sigma_{st}$	— Stadistical Component of the Uncertainty
$\sigma_{si}$	— Sistematically Component of the Uncertainty
$A_m$	— Activity Measured
$10 \mu\text{Sv}/\text{cm}$	— MicroSievert per Centimeter

### Atomic and nuclear symbols

${}_1^1\text{H}$	— Hydrogen
${}_1^2\text{H}$	— Deuterium (Non-Radiactive Hydrogen Isotope)
${}_1^2\text{D}$	— Deuterium (Non-Radiactive Hydrogen Isotope)
${}_1^3\text{H}$	— Tritium (Radiactive hydrogen Isotope)
${}_1^3\text{T}$	— Tritium (Radiactive hydrogen Isotope)
${}_6^{14}\text{C}$	— Carbon
${}_{19}^{40}\text{K}$	— Potassium
${}_{86}^{226}\text{Ra}$	— Radon
${}_2^3\text{He}$	— Isotope of the Helium(Non-radiactive, 1 neutrons)
${}_7^{14}\text{N}$	— Nitrogen
${}_6^{12}\text{C}$	— Carbon
${}_3^{6}\text{Li}$	— Lithium Isotope
${}_3^{7}\text{Li}$	— Lithium
${}_5^{10}\text{B}$	— Boron
${}_8^{16}\text{O}$	— Oxygen
${}_{86}^{222}\text{Rn}$	— Radon
${}_{19}^{40}\text{K}$	— Potassium

## X

$^{137}_{55}\text{Cs}$	— Cesium
n	— Free Neutron
$\text{H}_2\text{O}$	— Usual Water
$\text{D}_2\text{O}$	— Heavy Water
HT	— Air tritium molecule
HTO	— Water tritium molecule
OBT	— Organic tritium molecule
$T_{1/2}$	— Half-life Time of a Radioactive Element
$\beta$	— Beta Decay
$\bar{\nu}_e$	— Electron Antineutrino
$e^-$	— Electron
$\gamma$	— Gamma
$\sigma$	— Cross Section of a radioactive process
$\eta_{det}$	— Intrinsic Detector Efficiency
$F_{sci}$	— Active surface of the Plastic Scintillator
$\varepsilon_{det}$	— Specific Detector Efficiency
mip	— Minimum Ionizing Particle
$Q_\beta$	— Energy released in a radioactive decay

Units:

mSv/yr	— Millisievert per Year
mrem	— Millirem
STP	— Standard Temperature ( $0^\circ\text{C} = 273\text{K}$ ) and Pressure (1 atm)
W	— Watt
h	— Hour
g CO <sub>2</sub> /kWh	— Grams of CO <sub>2</sub> per Kilowatt Hour
L	— Liter
Bq	— Becquerel, Nuclear Decay Number per Second
Bq/L	— Becquerel per Liter
Ci	— Curies

$Ci/L$	— Curies por Liter
$yr$	— Year
$Ci/yr$	— Curies per year
$GW$	— GigaWatt
$\mu S/cm$	— MicroSivers per Centimeter
$kcps$	— Kilo Counts per Second
$pF$	— picoFarads
$A$	— Ampere (C/s).
$C$	— Coulomb.
$V$	— Voltage.
$T$	— Temperature ( $^{\circ}C$ ).
$Vol$	— Volume ( $m^3$ ).

Añadir en un futuro:

$D&D$	— Decontamination and Decommissioning.
$DWS$	— Drinking Water Standars
$NA$	— Numerical Apertures



# Contents

<b>Acknowledgements</b>	<b>III</b>
<b>Abstract</b>	<b>V</b>
<b>Nomenclature and acronyms</b>	<b>VII</b>
<b>List of Figures</b>	<b>XXV</b>
<b>List of Tables</b>	<b>XXIX</b>
<b>1 Introduction</b>	<b>1</b>
1.1 Tritium and Nuclear Energy . . . . .	1
1.2 Tritium Properties and Radiological Hazards . . . . .	10
1.3 Current Legislation . . . . .	18
1.4 This thesis . . . . .	21

<b>2 Tritium Detection Systems</b>	<b>23</b>
2.1 State-of-the-Art . . . . .	23
2.2 TRITIUM Project . . . . .	28
<b>3 TRITIUM Design Principles</b>	<b>33</b>
3.1 Detector System Overview . . . . .	33
3.2 TRITIUM Detector . . . . .	36
3.2.1 Interaction of Particles with Matter . . . . .	38
3.2.2 Plastic Scintillators . . . . .	41
3.2.3 Light Detection in Photosensors . . . . .	49
3.2.4 Electronic Readout . . . . .	69
3.3 Ultrapure Water System . . . . .	82
3.3.1 Introduction to the Water System . . . . .	82
3.3.2 Water System Set Up . . . . .	83
3.4 Background Rejection System . . . . .	86
3.4.1 Passive Shield (Lead) . . . . .	88
3.4.2 Active Shield (Cosmic Veto) . . . . .	90
<b>4 TRITIUM Detector R&amp;D</b>	<b>95</b>
4.1 Introduction . . . . .	95

4.2 Characetrization of the Scintillating Fibers . . . . .	97
4.3 Characterization of the SiPM . . . . .	128
4.4 Characterization of the Ultrapure Water System . . . . .	133
4.5 Characterization of the Cosmic Veto . . . . .	137
<b>5 TRITIUM Monitor Prototypes</b>	<b>145</b>
5.1 Introduction . . . . .	145
5.2 Preliminary Prototypes . . . . .	147
5.2.1 TRITIUM-IFIC 0 . . . . .	147
5.2.2 TRITIUM-IFIC 1 . . . . .	151
5.3 Latest TRITIUM Prototypes . . . . .	155
5.3.1 TRITIUM-Aveiro 0 . . . . .	155
5.3.2 TRITIUM-IFIC 2 . . . . .	164
5.4 Modular TRITIUM Detector . . . . .	169
<b>6 Simulations</b>	<b>173</b>
6.1 Introduction . . . . .	173
6.2 Geant4 Environment . . . . .	174
6.3 Description of the Simulations Performed . . . . .	176
6.3.1 Tritium Source Shape . . . . .	176

6.3.2	Fiber Length . . . . .	177
6.3.3	Fiber Diameter . . . . .	177
6.3.4	Tritium-IFIC 2 . . . . .	178
6.3.5	Lead Shielding and Cosmic Veto . . . . .	181
<b>7</b>	<b>Results and Discussion</b>	<b>183</b>
7.1	Introduction . . . . .	183
7.2	Results from Laboratory measurements . . . . .	185
7.2.1	Experimental Results of TRITIUM-IFIC 0 . . . . .	186
7.2.2	Experimental Results of TRITIUM-IFIC 1 . . . . .	186
7.2.3	Experimental Results of TRITIUM-Aveiro 0 . . . . .	186
7.2.4	Experimental Results of TRITIUM-IFIC 1 . . . . .	187
7.3	Experimental Results in Arrocampo dam . . . . .	188
7.4	Results of the simulations . . . . .	189
<b>8</b>	<b>Conclusions and Prospects</b>	<b>191</b>
<b>Appendices</b>		
<b>A</b>	<b>Birks Coefficient Study</b>	<b>195</b>
<b>B</b>	<b>Signal Processing in NIM Modules</b>	<b>197</b>

<b>C Electronical Schemes of PCBs Used for SiPM Characterization</b>	<b>199</b>
<b>D Ultrapure Water System</b>	<b>201</b>
<b>E Preparation of Liquid Radioactive Source of Tritium</b>	<b>205</b>
<b>F Electronic System of TRITIUM-Aveiro 0 prototype</b>	<b>207</b>
<b>Bibliography</b>	<b>209</b>



# List of Figures

1.1	Annual average distribution of the radioactive dose received by the population [1] . . . . .	2
1.2	Networks of automatic station and sampling station belonging of CSN of Spain. . . . .	6
1.3	Tritium sampling locations around Cofrentes NPP. . . . .	12
1.4	Tritium activity levels in surface water around Cofrentes NPP from January 2006 to November 2019. The white points are used for the detection limit and the green points are used for the measured activity, when it is above the detection limit. [9]	12
1.5	Tritium activity levels in groundwater around Cofrentes NPP from January 2006 to November 2019. [9] . . . . .	13
1.6	Tritium decay . . . . .	14
1.7	Energy spectrum of tritium electrons [31] . . . . .	15
2.1	Arrocampo dam, Almaraz NPP and Tajus river . . . . .	29
3.1	Scheme of the scintillator detector . . . . .	37

3.2	Domain regions of the three most probable types of interactions of gamma rays with matter. The lines show the values of Z and $h\nu$ where the two neighboring effects are equally likely. [76, 77]	39
3.3	Jablonsky diagram. [76]	43
3.4	Stokes shift. [76]	44
3.5	Emission spectrum of BCF-12 fibers of Saint-Gobain. [78]	47
3.6	How photons are collected in a fiber with single clad. [78]	48
3.7	Scheme of a PMT. [76]	52
3.8	Quantum efficiency spectrum for the PMT used (R8520-ZB277). [83]	53
3.9	Hamamatsu commercial voltage divider electronic circuit. Upper circuit with negative supply and lower circuit with positive supply. [83]	54
3.10	Energy band scheme for (a) insulator, (b) semiconductor and (c) conductor. [77]	57
3.11	Crystal lattice and energy band scheme formed by a silicon with (left) a pentavalent dopant that creates an n-type semiconductor (right) a trivalent dopant that creates a p-type semiconductor. [77]	59
3.12	(Above) Schematic of the charge distribution and electric field created in a pn-junction. (Bottom) Commonly used symbol for a diode. [84]	59
3.13	Scheme of a APD and electrical symbol used. [85]	62

3.14 Using persistence on the oscilloscope to show several pulses with different heights. Each height associated with a different number of SiPM pixels lit at the same time. . . . .	63
3.15 (Left) Electronic scheme of a SiPM and (right) output current of a SiPM as a function of the reverse voltage. It show that the quenching mechanism is essential for working with SiPMs [90] . . . . .	64
3.16 Electronic scheme of the electronic voltage divider circuit used for working with PMTs without its internal gain.). . . . .	70
3.17 Schemes of different electronic configuration used to measure with PMT. . . . .	72
3.18 Different situation that can happen when we do time coincidences with PMTs. . . . .	76
3.19 Signal amplified and logical gate (input signals of MCA). . . . .	77
3.20 Different parts of PETSYS system. [103] . . . . .	78
3.21 Three PCBs used for the SiPM characterization and LED emission spectrum. . . . .	81
3.22 Scheme of water purification system. . . . .	84
3.23 Lead Bricks and their arrangement in the lead shielding. . . . .	89
3.24 Lead Bricks and their arrangement in the lead shielding. . . . .	89
3.25 Cosmic veto and Tritium-IFIC 2 prototype in an aluminum mechanical structure developed by IFIC's mechanical engineering department. . . . .	91

3.26 Hard cosmic events detected with the cosmic veto of TRITIUM: a) Affecting to the tritium measurement, b) Does not affecting to the tritium measurement. c) Hard cosmic muon rate. . . . .	92
3.27 Emission energy spectrum of the plastic scintillation used for the cosmic vetos. [111] . . . . .	93
3.28 Different layers used to cover of the cosmic veto. . . . .	94
4.1 Unsuccessful results of using commercial techniques to cut fibers. . . . .	99
4.2 Microscopes used to check the results. . . . .	99
4.3 Cutting device developed in the TRITIUM experiment and additional part to make precise measurements of fiber length. .	100
4.4 Result of the polishing process. a) Fiber end after cutting with TRITIUM devices b) Fiber end after cutting with TRITIUM devices and polishing with Thorlabs technic. . . . .	102
4.5 Polishing machine developed in TRITIUM experiment. . . . .	103
4.6 Polishing table of the polishing machine . . . . .	105
4.7 Electronic system of Polishing machine. . . . .	107
4.8 Set up used to test the effect of the polishing machine. . . . .	108
4.9 Energy spectrums used to test the effect of the Polishing machine . . . . .	109
4.10 Set up used for fiber characterization. . . . .	111

4.11 Emission spectrum measured for the LED model 435-03 from Roithner LaserTechnik GmbH Company. . . . .	112
4.12 Difference between the results obtained in both tests carried out to check the light-tight quality of the system. . . . .	113
4.13 Response of the PMT based on its high voltage using the PCB with which we get no internal gain from the PMT. . .	114
4.14 Linearity tests of the PMT response . . . . .	116
4.15 Number of photons/ns reaching the PMT for No Clad fibers. .	120
4.16 Average of 10 samples for each fiber type (no clad, single clad and multiclad fibers). . . . .	121
4.17 Wetting property produced by the cleaning process. [] . . .	124
4.18 Energy spectrums used to test the effect of the Cleaning process	126
4.19 Counts per second at several high voltage and fixed thresholds and several thresholds and fixed high voltage. . . . .	139
4.20 Energy spectrum measured with the cosmic veto. . . . .	140
4.21 Energy spectrum of cosmic vetos for several distance between cosmic detectors. . . . .	141
4.22 Linear fit of the counts per second measured with the cosmic veto with several distance between its cosmic detectors. . . .	142
5.1 Bundle of 35 fibers, whose length is 20 cm, used in Tritium-IFIC 0 prototype . . . . .	148
5.2 Tritium-IFIC 0 Prototype. . . . .	149

5.3	PMMA vessel used to check photon loss due to fiber bundle curve. . . . .	151
5.4	Teflon structure used to arrange the fibers of Tritium-IFIC 1 prototype in a matrix of 8 · 8. . . . .	152
5.5	Teflon vessel of Tritium-IFIC 1 prototype . . . . .	153
5.6	A general view of Tritium-IFIC 1 prototype . . . . .	154
5.7	Tritium-Aveiro prototype. . . . .	156
5.8	Teflon structure and fiber bundle used in Tritium-Aveiro 0 prototype. . . . .	156
5.9	Transmission spectrum of light (in the visible range) in a piece of PMMA of X thickness measured in the ICMOL laboratory. . . . .	158
5.10	Electronic scheme of the PCB designed to power the PMTs of Aveiro prototype and the graphical user interface developed to control it. . . . .	160
5.11	Simplified electronic scheme used to process and analyze the signal of Tritium-Aveiro 0 prototype. . . . .	161
5.12	Graphical user interface used to manage the counter system. . . . .	163
5.13	Two different situations of the electronic chain response. A.- Event accepted since veto has not detected it. B.- Event rejected since veto has detected it . . . . .	164
5.14	Tritium-IFIC 2 prototype. . . . .	165
5.15	Tritium-IFIC 2 teflon vessel. . . . .	166

5.16 Graphical User Interface (GUI) of PETSYS. . . . .	167
5.17 A schematic design of the Tritium detector. . . . .	169
5.18 A tritium detector design based on the Tritium-IFIC 2 prototype. . . . .	171
6.1 Distribution of the scintillating fibers in the simualtion of Tritium-IFIC 2 prototype. . . . .	179
6.2 Simualtion of Tritium-IFIC 2 prototype. PMTs (black), the optical grease (blue), PMMA windows (white), tritiated water (green) and scintillating fibers (yellow) . . . . .	181
D.1 Scheme of the ultrapure water system. . . . .	201
D.2 Different stages of filtration of the ultrapure water system. . . . .	202
D.3 Doble phase reverse osmosis stage and containers used to store the outlet water of the ultrapure water system. . . . .	203
D.4 Siemens PLC, software for remote control of ultrapure water system. . . . .	203
D.5 General photo of the complete ultrapure water system. . . . .	204
D.6 Raw water, reject water and ultrapure water obtained with this system. . . . .	204



# List of Tables

1.1	Annual average distribution of the effective dose received by the population due to natural radioactive [2][3]. . . . .	2
1.2	Emission of tritium per year from different types of nuclear reactors. Pressurized Water Reactor (PWR), Boiled Water Reactor (BWR), Heavy Water Reactor (HWR) and Gas-Cooled Reactor (GCR) [13] . . . . .	7
1.3	Most common nuclear reactions of artificial tritium production [13] . . . . .	11
1.4	Penetration depth for decay electron of mean (5, 7 keV) and maximum (18, 6 keV) energies in different media (tritium gas and air at standard conditions of temperature (273 K) and pressure (1 atm), STP, and water) [32] . . . . .	15
1.5	Legal limit of tritium in drinking water established in each country. . . . .	20

2.1	State-of-the-art in the tritium detection for different techniques. This table show the measured quantity, low detection level (LDL) and the sample form for four different technics, liquid scintillator counter (LSC), Ionization Chamber (IC), Calorimetry and the beta induced X-rays Spectrometry (BIXS)	24
2.2	Results of different scintillator detector for tritiated water detection . . . . .	26
3.1	Critical angles asociated to different interfaces created with polystyrene, $n_0 = 1.6$ , and other materials . . . . .	49
3.2	Properties of BCF-12 fibers from Saint-Gobain Inc. [78] . . . . .	50
3.3	Characteristics of SiPM S13360-6075 from Hamamatsu Photonics [87]. . . . .	65
3.4	Classification of natural radioactive series [106][107]. . . . .	87
3.5	Properties of plastic scintillator blocks from Epic-Crystals. [111]	93
4.1	Average and standard deviation (due to fiber position in setup) of photons per nanosecond that reach the PMT for 0.1 mA LED intensity. . . . .	117
4.2	Average, standard deviation and relative standard deviation of 10 different samples of no clad fibers. . . . .	119
4.3	Average, standard deviation and relative standard deviation of 10 different samples of single clad fibers. . . . .	119
4.4	Average, standard deviation and relative standard deviation of 10 different samples of multi clad fibers. . . . .	119

4.5 Relative standard deviations ( $\sigma_t$ , $\sigma_{pos}$ and $\sigma_{con}$ ) measured in this test. . . . .	121
4.6 Average and standard deviation of 10 different fibers of 10 cm. . . . .	123
4.7 Collection efficiency of each fiber type for 10 centimeters, $CE_{10}$ , and 1 meter, $CE_{100}$ . . . . .	123
4.8 Chemical components and turbidity measured in the raw water sample. . . . .	134
4.9 Measurements of the conductivity for several samples of each water type (raw water, pure water and reject water). . . . .	135
4.10 Measurements of the activity for several samples of both water types (raw water and pure water). . . . .	137



# Chapter 1

## Introduction

### 1.1 Tritium and Nuclear Energy

Radioactivity has been present in the Universe since its inception. It was an important element of the Big Bang<sup>1</sup>, which occurred about  $14 \cdot 10^9$  years ago. It was also present during the formation of the earth,  $4.5 \cdot 10^9$  years ago, which explains why the different layers that make up the earth contain radioactive elements.

Therefore, humanity has been exposed to radioactivity since its origin, whether present in the earth's crust or in the universe (external natural irradiation). Even the human being himself is radioactive as radioactive elements are contained in the human body such us  ${}^3\text{H}$ ,  ${}^{14}\text{C}$  or  ${}^{40}\text{K}$ , introduced into the body through food or water ingestion or air inhalation (internal natural irradiation). The annual average of the radioactive dose received by the population is presented in Figure 1.1 and Table 1.1.

---

<sup>1</sup>The Big Bang is the most acceptable hypothesis that explains the formation of the universe and its development over time so far.

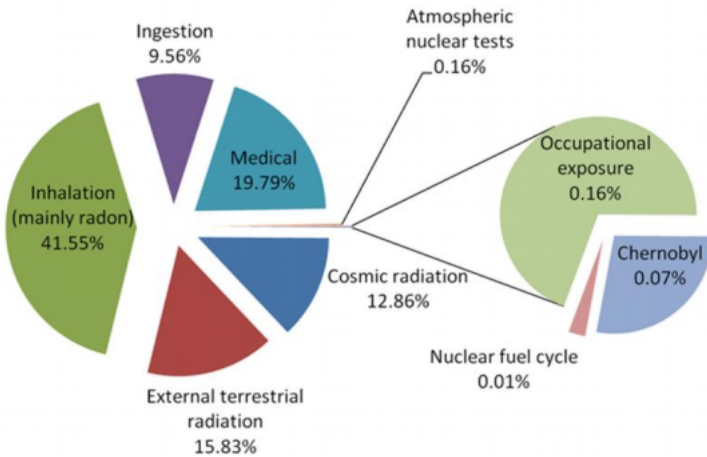


**Figura 1.1** – Annual average distribution of the radioactive dose received by the population [1]

Radiation source	Eff. dose (mSv/yr)	Typical range (mSv/yr)
Cosmic (external)	0.39	0.3 – 1.0
terrestrial (external)	0.48	0.3 – 0.6
Inhalation (internal)	1.26	0.2 – 10
Ingestion(internal)	0.29	0.2 – 0.8
Total	2.42	1 – 12.4

Table 1.1: Annual average distribution of the effective dose received by the population due to natural radioactive [2][3].

As can be seen in Figure 1.1, most of the radioactive dose received by the population is due to both, internal and external natural radiation, called natural radiation, whose effective dose<sup>2</sup> is estimated in 2.42 mSv/yr as can be seen in Table 1.1. It can also be appreciated in Figure 1.1 that the most important part of the artificial radiation received comes from medical purposes.

Since the discovery of radioactivity, made by Hènri Becquerel in 1896, a lot of technology based on nuclear concepts has been developed and applied to several fields such as energy production, research, medicine, industry, etc.

Due to the introduction of radioactivity in the society, various anthropogenic radioactive sources have appeared in the environment, resulting in increased levels of radioactive elements in the environment, called radioactive background.

As our knowledge about radioactivity and our measurement techniques have advanced, the negative effects of radioactivity have been observed and characterized as it will be shown in section 1.2. Because of that, it is important to control the level of radioactive background to which the population is exposed and to ensure that its levels is kept below of a safe limit. For this task, several organization has been created to manage the radioprotection in the world.

In the first place, the definition of concepts and units was necessary to quantify the negative effects of radioactivity and, for that, the International Commission of Radiological Units and Measurements, ICRU [4], was created during the first international conference of radiology held in London, in 1925.

Secondly, the International Commission on Radiological Protec-

---

<sup>2</sup>The effective dose is the radioactive dose absorbed by the population, taking into account the different radiosensitivity in each organ or tissue.

tion, ICRP [5], was created in 1928 by the International Society of Radiology, ISR [6]. The ICRP aims to make recommendations and provide guidance on different aspects of protection against radioactivity. The ICRP does not have the legal capacity to enforce its recommendations, but these are widely taken into account in the legislation of most countries.

In the third place, the United Nations Scientific Committee on the Effects of Atomic Radiation, UNSCEAR [2], was created in 1955, whose objective is to estimate and report the levels and effects of ionizing radiation on the population and the environment. These estimates are taken into account by governments around the world to establish their limits and safety standards.

Fourth, the International Atomic Energy Agency, IAEA [1], was created in 1957, which is though to promote the peaceful use of nuclear energy and to avoid its use for any military purpose such us nuclear weapons. Although it is an independent agency, it must to report to the United Nations, UN [7].

Fifth, at the level of the European Union, EU, the European Atomic Energy Community, EURATOM, was created in 1957, which is a international organization established by the EURATOM treaty. Its objective is to coordinate research programs for the peaceful use of nuclear energy and the sharing of knowledge, infrastructure and financing of nuclear energy.

Finally, at the national level in Spain, the Nuclear Safety Council, CSN for its acronym in Spanish, was created in 1980 [3]. The CNS is the only institution in Spain with legal power to manage everything related to nuclear safety and radiological protection and its objective is to reduce to the maximum the excess of radioactivity in the environment due to anthropological origins.

For this task, the CSN has created several networks consisting of several detectors of radioactivity that are in charge of controlling the levels

of radioactivity in the environment and checking the impact of radioactivity facilities to it. Two of the most important networks are the network of automatic stations and network of sampling stations:

On the one hand, the network of automatic stations [8], REA for its acronym in Spanish, shown in Figure 1.2a, which consists of several gamma detectors<sup>3</sup> distributed in Spain that measure the radioactive dose in real time. The REA is used for the immediate detection of radiological problems and the application of quick response.

On the other hand, the network of sampling stations [9], REM for its acronym in Spanish, shown in Figure 1.2b, which consists of several points of interest in Spain where samples are taken and transported to a laboratory to be measured. About twenty Spanish laboratories are integrated into this network, whose objective is to characterize the concentration and evolution of various radioisotopes present in the radioactive background of Spain and to quantify the impact of radioactive facilities on the environment.

There are other networks that measure different parameters such as the concentration of  $^{226}\text{Ra}$  in the air and the measurements of all the networks are adapted to the EUROTAM treaty [10].

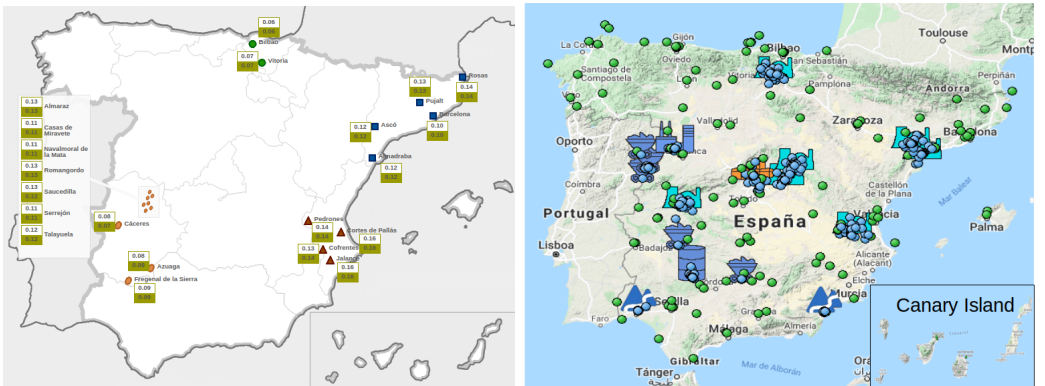
The objective of this thesis and the objective of the *TRITIUM* project is to develop a monitor capable of automatically measuring low levels of tritium in water in quasi-real time<sup>4</sup>. This monitor is destined to be finally included in the REA.

Tritium is one of the radioactive isotopes routinely measured in REM tests. Its detection is based on low-energy beta radiation measurements of the radioactive decay of tritium, mainly through the liquid scintil-

---

<sup>3</sup>Detectors that only measure gamma radioactivity

<sup>4</sup>Quasi-real time is an approximation of real-time measurements. It means a relatively small time, like ten minutes.



(a) Measured points of the REA [8]. The white box is the daily average of the gammadots are located around nuclear facilities. dose and the green box is the monthly averageGreen dots are uniformly distributed in of the gamma dose. (b) Measured points of the REM [9]. Green dots are uniformly distributed in Spain.

**Figura 1.2** – Networks of automatic station and sampling station belonging of CSN of Spain.

lation counter technique, LSC. Due to the limitations of the current methods, which will be shown in section 2.1, the objective of the *TRITIUM* project is to build a tritium detector based on scintillating fibers that will be put directly in contact with the sample (water). The photons produced in these scintillating fibers will be readout using photosensors, either photomultiplier tubes (PMTs) or silicon photomultipliers (SiPMs).

The *TRITIUM* collaboration is an international group consisting of a consortium of 6 different southwestern European institutions of 3 different countries: Portugal, France and Spain. The final emplacement of the *TRITIUM* monitor is the Arrocampo dam, Extremadura, Spain, whose water is used for the cooling system of the Almaraz fission nuclear power plant, hereinafter called nuclear power plant, NPP. This detector will be installed 4 km downstream from the Almaraz Nuclear Power Plant.

The monitor will be used to ensure that the tritium levels of the Arrocampo dam water are below of the legal limit specified in the EU-

RATOM treaty [10], which is 100 Bq/L as it will be shown in section 1.3. It will be used indirectly to verify the correct operation of the Almaraz NPP, located 4 km above the river since a malfunctioning of it will produce a variation in the tritium activity.

Tritium is one of the most frequently produced radioisotope in a NPP, as it has been verified in the United States Department of Energy complex, (U.S. DOE) [11], [12] and in several research facilities in China [13] and places around them (ground water, surface water and process waste water).

Tritium is normally produced in the water used in the nuclear reactor cooling system or the moderator of some NPPs. It is produced by neutron capture of the deuterium, existing in the heavy water ( $D_2O$ ), semi-heavy water ( $HDO$ ) or the deuterium created by neutron capture in usual water ( $H_2O$ ). All these processes have a large probability to happen due to the huge neutron flux in the nuclear reactor, of the order of  $10^{14} \text{ n cm}^{-2}\text{s}^{-1}$  [14]. This tritium is finally released partially or totally to the environment, whose quantitu depends on the reactor type as it is shown in Table 1.2. The most common way that tritium is released to the environment is HTO [13].

Reactor type	Gaseous discharge (GBq/y)	Liquid discharge (GBq/y)
PWR	$3.70 \cdot 10^3$	$2.59 \cdot 10^4$
BWR	$1.85 \cdot 10^3$	$3.70 \cdot 10^3$
HWR	$7.40 \cdot 10^5$	$1.85 \cdot 10^5$
GCR	$7.40 \cdot 10^3$	$1.11 \cdot 10^4$

Table 1.2: Emission of tritium per year from different types of nuclear reactors. Pressurized Water Reactor (PWR), Boiled Water Reactor (BWR), Heavy Water Reactor (HWR) and Gas-Cooled Reactor (GCR) [13]

NPPs are operational since more than 60 years and, nowadays, they are essential for providing a large part of the electric power that is

used in the current world (more than 20% in Spain [15]). Although the Spanish government is projecting to progressively close all NPP there are other countries like China [16] or United States, USA [17], which intend to promote their use.

On the one hand, NPPs are an interesting investment since it is one of the cheapest source of energy production. It is a stable, as it doesn't depend on meteorological parameters and it doesn't emit greenhouse gases. Although there are other alternative energy sources which are being developed quickly (photovoltaic, wind, tidal energy, etc.), even other concepts of energy production and saving (local production, solar roofs, energy efficiency, smart cities, etc.), today they are not developed enough to fully cover the population needs.

On the other hand, NPPs still have some problems such as the contamination of fresh water from uranium mining, the nuclear waste produced, the nuclear proliferation or the risk of radioactive contamination from accidents as happened in the past: Chernobyl, Fukushima or Three Mile Island [18].

In any case it is not important if we agree or not with nuclear energy source. The only important thing is that the nuclear energy production in the world is not going to stop in the next decade, in fact, it will increase as the United States Energy Information Administration (U.S. EIA) expect [19]. Therefore the development of different types of alarm systems is a good investment. Safety is not a negotiable aspect and there must be mechanisms that warn us of any malfunction of a nuclear power plant.

In addition, it is important to highlight that the developed monitor could be used to verify the correct operation of a nuclear power plant, but it is not our objective. Our much broader objective is to ensure that the levels of tritium in the analyzed water are below the Spanish legal limit. It means

that this monitor could be used in many different places with radioactive facilities like the future fusion power plants<sup>5</sup>, nuclear research facilities<sup>6</sup> or tracking the movement of tritium contaminated plumes in ground water [22].

---

<sup>5</sup>The International Thermonuclear Experimental Reactor, ITER, will need up to several tens of kilograms of tritium to function, which correspond to various TBq of tritium.

<sup>6</sup>Tritium is one of the main emissions from these sites [20], [21].

## 1.2 Tritium Properties and Radiological Hazards

Tritium is the only radioactive isotope of hydrogen. It was first time produced in 1934 from neutron capture of deuterium by Ernest Rutherford, Mark Oliphant and Paul Harteck [23] and it was first time isolated in 1939 by Luis Walter Alvarez and Robert Cornog [24], who checked that tritium is a radioactive element.

Tritium is naturally produced in the environment through the interaction of cosmic rays and gaseous elements of the upper atmosphere like nitrogen ( $^{14}\text{N}(\text{n}, ^3\text{H})^{12}\text{C}$ ) [25] and oxygen ( $^{16}\text{O}(\text{n}, ^3\text{H})^{14}\text{N}$ ) [26]. Around 99% of this tritium form water (HTO) and reaches the earth's surface as rain with an estimated production rate of  $4 \cdot 10^6 \text{ Ci/yr}$  ( $1.48 \cdot 10^8 \text{ GBq/yr}$ ), producing a tritium concentration of  $0.6 - 1.2 \text{ Bq/L}$  in precipitation [13, 25].

Tritium can be produced artificially in the environment from different anthropogenic sources [13, 25]. There is a large amount of tritium which was produced in military nuclear test explosions between 1945 and 1975, with an estimated total production of  $8 \cdot 10^9 \text{ Ci}$  ( $2.96 \cdot 10^{11} \text{ GBq}$ ) and a part of which remains to the date. In these nuclear explosions, tritium was produced mainly from the nuclear reactions  $^{14}\text{N}(\text{n}, ^3\text{H})^{12}\text{C}$  and  $^2\text{H}(\text{n}, \gamma)^3\text{H}$ . Tritium can be also produced by commercial producers of radioluminescent and neutron generator devices ( $1 \cdot 10^6 \text{ Ci/yr}$ ), nuclear power and defense industries (around  $2 \cdot 10^6 \text{ Ci/yr}$ ) and several research facilities and nuclear reactor for energy production ( $2 \cdot 10^6 \text{ Ci/GWyr}$ ), whose main production cross sections are shown in Table 1.3:

Tritium levels in the environment when anthropological radioactive sources are not involved are between  $1$  and  $4 \text{ Bq/L}$ . This is a higher value than the expected due to the cosmogenic background levels ( $0.6 - 1.2 \text{ Bq/L}$ , previously mentioned) [27]. It can be explained by the consequences of

Element	Origin	Nuclear reaction	Cross section (b)
$^2_1\text{H}$	Water coolant	$^2_1\text{H}(\text{n}, \gamma)^3_1\text{H}$	$5.2 \cdot 10^{-4}$
$^3_2\text{He}$	Helium coolant	$^3_2\text{He}(\text{n}, \text{p})^3_1\text{H}$	5330
$^6_3\text{Li}$	Moderator	$^6_3\text{Li}(\text{n}, \alpha)^3_1\text{H}$	940
$^{10}_5\text{B}$	Moderator, control rods	$^{10}_5\text{B}(\text{n}, 2\alpha)^3_1\text{H}$	3835

Table 1.3: Most common nuclear reactions of artificial tritium production [13]

nuclear weapons tests.

Tritium levels in rivers around a nuclear facility are between 1 and 10 Bq/L and even between 20 and 50 Bq/L at the water discharge site of NPPs [27], where the produced tritium is partially or totally released into the environment, mainly in the HTO water form.

The effect of NPP on tritium levels can be observed using the public measurements of the REM, explained in the section 1.1. For example, in the case of Cofrentes, which is the closest nuclear power plant to Valencia and the one in whose measurements are involved LARAM<sup>7</sup>, the tritium levels in the river are measured in three different places, marked on the map shwon in Figure 1.3. The first place, P1, is located in the river, 6 km upstream from the NPP, the second place, P2, is located 1 km downstream and the third place, P3, is located 5 km downstream. The level of Tritium measured in these three locations is shown over time in Figures 1.4a, 1.4b and 1.4c respectively.

In these figures, the detection limit and the measured activity are shown using white dots and green dots respectively. The measured activity is only displayed when it is larger than the corresponding detection limit. As it can be seen, the tritium level in the river increases due to the discharge

---

<sup>7</sup>LARAM is a Valencia laboratory specialized in environmental radioactivity measurements



**Figura 1.3** – Tritium sampling locations around Cofrentes NPP.

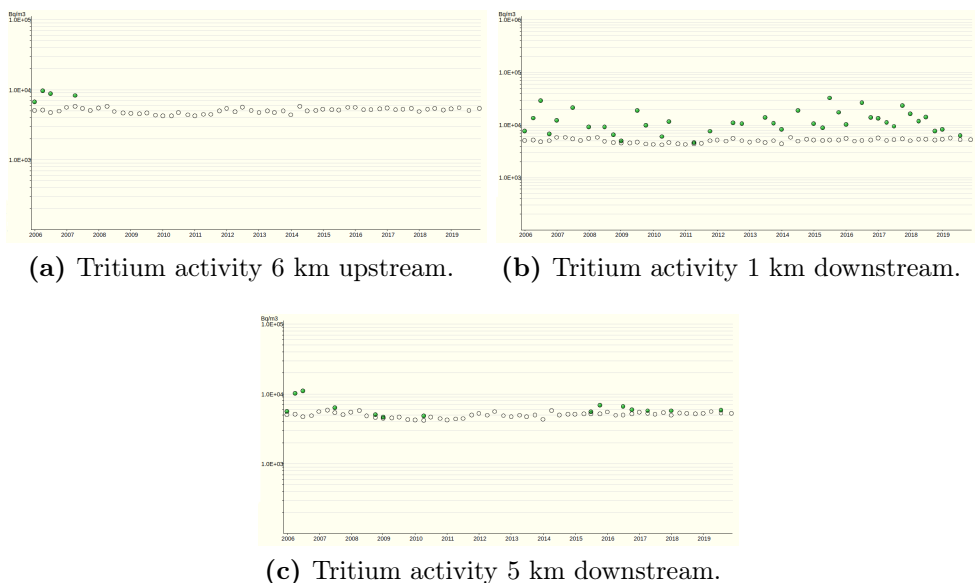
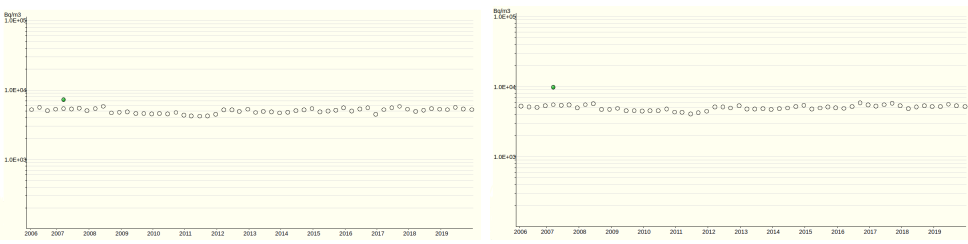


**Figura 1.4** – Tritium activity levels in surface water around Cofrentes NPP from January 2006 to November 2019. The white points are used for the detection limit and the green points are used for the measured activity, when it is above the detection limit. [9]

of the NPP and it is diluted again after 4 km downstream.

Two additional measurements of the tritium level in groundwater have been included, points S1 and S2 on the map in Figure 1.3, which are located 1 km before and 1 km after the NPP. Both tritium levels are shown in the figure 1.5a and 1.5b respectively, where it can be verified that the nuclear power plant has not affected them.



(a) Tritium activity 1 km before NPP. (b) Tritium activity 1 km after NPP.

**Figura 1.5** – Tritium activity levels in groundwater around Cofrentes NPP from January 2006 to November 2019. [9]

It is important to note that, although environmental tritium levels have been affected due to NPP, these levels are below the legal limit. The maximum level of tritium measured since of January 2, 2006 is around 32 Bq/L, below to the legal limit in Europe, 100 Bq/L.

Tritium is a radioactive element whose half-life time is  $T_{1/2} = 12.32$  years. It has one proton and two neutrons and decays exclusively through  $\beta$  radiation. It decay 100% directly to the ground state of Helium ( ${}^3_2\text{He}$ ), which is a stable nuclei, thorugh the decay scheme of equation 1.1:



In Figure 1.6 the scheme of tritium energy levels is shown. In this decay it is not possible to detect the neutrino because of its extremely weak interaction with matter ( $\sigma \propto 10^{-42} \text{ cm}^2$  [28]) and, since  ${}^3\text{He}$  has a much

larger mass than electrons and neutrinos, by conservation of energy and momentum, the energy that is taken by this daughter nucleus is very small. Therefore, the detection of tritium is through its decay electron.

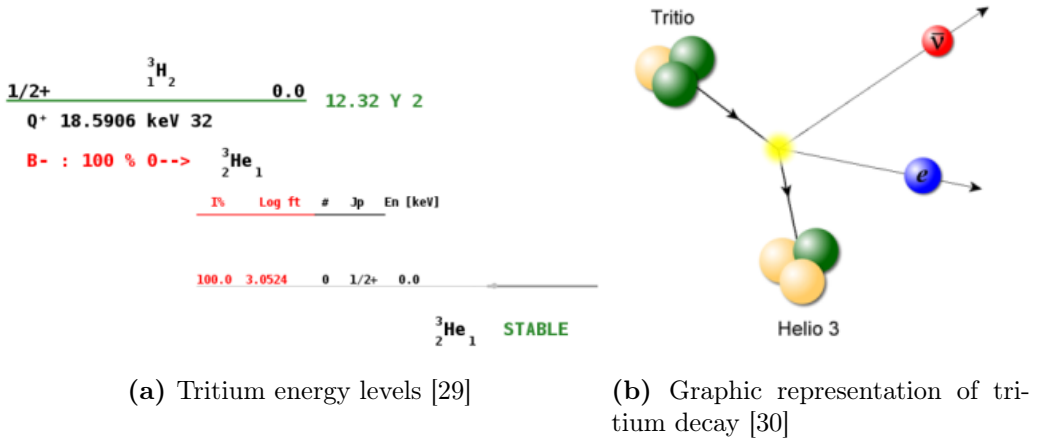


**Figura 1.6 – Tritium decay**

The energy released in the tritium decay is  $Q_\beta = 18.6$  keV, which is divided between the decay products. Therefore, the energy spectrum of the decay electrons is a continuum with a maximum value of 18,6 keV, as shown in Figure 1.7. This energy spectrum has an average of 5.7 keV and the most likely value is slightly below, around 4.5 keV.

The releasing energy of the tritium decay, is very little. In fact, it is the radioactive isotope with the lowest energy released in its  $\beta$  disintegration [25]. Consequently, the  $\beta$  particle which is emitted in this tritium decay will have a very small mean free path as it is shown in Table 1.4.

This short mean free path is a major issue in tritium detection, as it makes more difficult the electron detection, which will require a highly sensitive detector. However, it means that the tritium electrons has a low penetration in our body and easily stopped with our clothes or laboratory gloves, resulting in a low radiological hazard of external tritium.

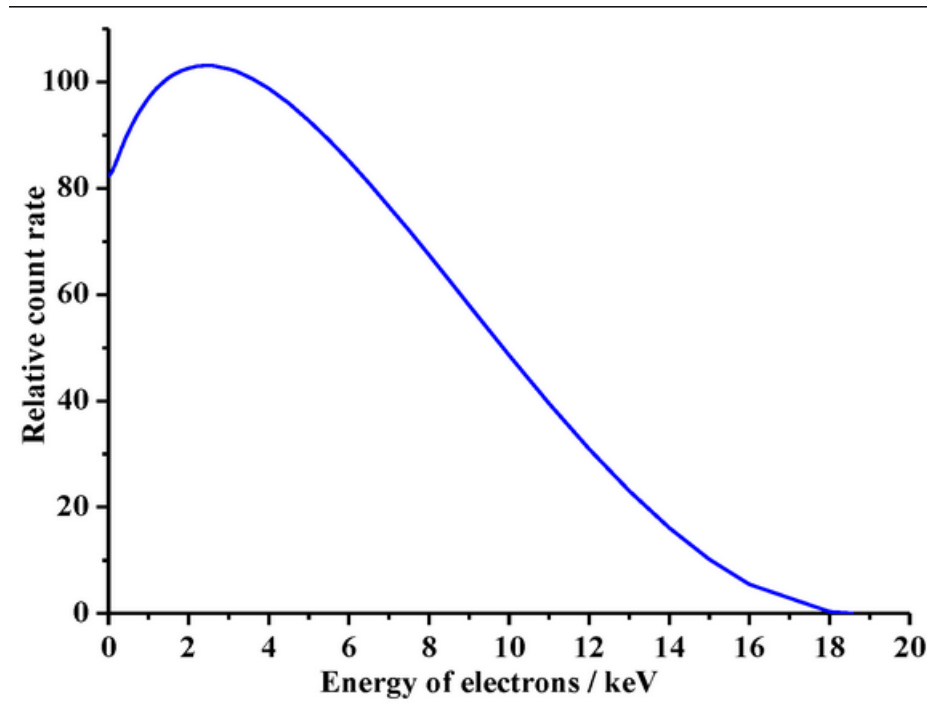


**Figura 1.7** – Energy spectrum of tritium electrons [31]

Material	P. Depth (5.7 keV)	P. Depth (18.6 keV)
${}^3_1\text{H}_2$	0.26 cm	3.2 cm
Air	0.036 cm	0.45 cm
Water, soft tissue (solid matter whose density is $1 \text{ g} \cdot \text{cm}^{-3}$ )	$0.42 \mu\text{m}$	$5.2 \mu\text{m}$

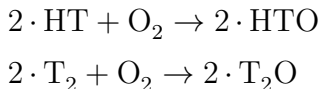
Table 1.4: Penetration depth for decay electron of mean (5, 7 keV) and maximum (18, 6 keV) energies in different media (tritium gas and air at standard conditions of temperature (273 K) and pressure (1 atm), STP, and water) [32]

Nevertheless, the danger of tritium increases when it is ingested or inhaled since it can bind anywhere that hydrogen can and perform the same chemical reactions, sometimes with higher rate if the tritium concentration is high enough to catalyze the reaction.

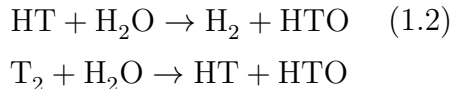
Tritium can be absorbed in our body in three different ways, gaseous tritium (mainly HT), tritiated water (mainly HTO) and organically bound tritium (called OBT).

The gaseous tritium, which is normally found mixed in the air, is the least important since less than a  $3 - 5 \cdot 10^{-3} \%$  is absorbed, which is insignificant [25]. However, it can be transformed into tritiated water through the oxidation and exchange reactions shown in the chemical schemes of equations 1.2, which has a more important effect on health [25]:

*Oxidation :*



*Exchange*



Tritiated water, which is normally found in drinking water or water in food, has a larger impact since the 99% of it is absorbed [25]. In addition, its biological life time of it is around 9.5 days ( $\pm 50\%$ ), time during which tritium will remain in our body [25, 27, 33].

This time corresponds to the water cycle in the body and, like this, it can vary due to various external parameters such as temperature, humidity, drinking habits, etc. or reduced with the use of diuretics [25].

Organically bound tritium, normally found in food, generally forms a covalent bond with a carbon and it corresponds to 5 – 10 % of tritium absorbed in the body. Although it is absorbed in less quantity in the body

than tritiated water, it can be more dangerous since it has a longer biological life time. The biological life time of this tritium type depends on the affinity of the organic molecule with the different biological tissues and it can vary from tens of days to hundreds of days (larger than the ICRP estimate) [27, 33, 34, 35].

There are many studies showing that tritium in living matter can cause the same effects than X-rays or  $\gamma$  rays, which are mutations, tumors, cancer, genetic effects, reproductive effects, etc [36, 37]. In fact, the consequences of tritium radiation can be worse than a similar  $\gamma$  radiations since its biological efficiency<sup>8</sup> is two or three times larger [36].

In summary, tritium is a naturally occurring radioactive element that can affect health if it is released excessively. Because of that, each country has developed a legislation, shown in section 1.3, to manage the release of tritium and ensure that these background levels are safe for health.

---

<sup>8</sup>The biological efficiency is used to quantify the damage produced in the living cells due to an external radiation.

## 1.3 Current Legislation

Due to the radiological risk of tritium, which has been shown in section 1.2, it is important to develop a legislation that limits the release of tritium to the environment ensuring that the levels are below a safe value for health.

The guidelines that impose the limit of radioactive elements in drinking water for many countries are based on the radiation protection methodology developed by the ICRP [38] and the recommendations of the world health organization, WHO [39].

The objective of the international radiation methodology is to protect people and the environment from the negative effects of ionizing radiations without limiting beneficial activities that involve radiation exposure. It is based on three main points, which are the justification (the benefit from radiological exposure must outweigh the detriment to health that it causes), the ALARA principle, "As Low As Reasonably Achievable" (the radiological exposure must be kept as low as possible considering social and economic factors) and dose limitation (limit that must never be exceeded).

While the ICRP recommends a maximum dose of 1 mSv/yr, excluding the natural background and medical interventions, the WHO is more conservative, recommending a maximum dose of 0.1 mSv/yr, which correspond to less than 5% of the annual dose due to background radiation, 2.42 mSv/year, Table 1.1.

The guideline reference level of each radionuclide in drinking water, GL, is usually calculated from these recommendations using the equation 1.3

$$GL = \frac{RDL}{DCF \cdot q} \quad (1.3)$$

Where RDL is the reference dose level, DCF is the dose conversion

factor (the normal used value for tritium is  $1.8 * 10^{-11}$  SvBq, provided by ICRP [40]) and q is an estimation of the annual volume of drinking water consumed (normally assumed two liters per day, 730 L/yr).

The GLD calculated for tritium in drinking water according to the ICRP and WHO recommendations is 76103 Bq/L and 7610 Bq/L respectively. It means that tritiated water with activities below these values is not harmful to health.

Based on these recommendations, each country has created organizations in charge of developing its own legislation on radionuclide limits. In Spain, the responsible organization of this task is the CSN.

Most of the countries in the world implement the RDL of 0.1 mSv/yr recommended by the WHO. The legal limit for tritium in drinking water in this case is 76.103 Bq/L but it is often approximated in different ways. Some countries like Switzerland [41] or some organizations like the WHO [39] rounded this value to 10,000 Bq/L. Others like some countries of Canada, such as Ontario and Québec, truncate this value to the first number 7,000 Bq/L [42, 43]. There are other countries like Russia which use the much more accurate approximation value of 7,700 Bq/L [44].

There are other countries like Australia that prefer to implement the RDL of 1 mSv/yr, recommended by the ICRP, whose legal limit is 76.103 Bq/L [45]. Other countries like Finland are based in the ICRP recommendations and use only the middle of this value, 0.5 mSv/yr, whose value is rounded to a legal limit of 30,000 Bq/L for tritium in drinking water [46].

There are two different exceptions to these recommendations:

1. On the one hand, most of the USA countires, such as California, use a RDL of 4 mrem (0.04 mSv), which corresponds to a legal limit of 20 nCi/L (740 Bq/L) [47]. This value was proposed by the United

States Environmental Protection Agency (US EPA) as a result of an analysis of the available information [48].

- On the other hand, most of the EU countries, such as France, Germany or Spain, impose an GL of 100 Bq/L, which is one of the most restrictive limit in the world [49, 50, 51]. This value arise from the consideration that it is an indicator of the presence of other radionuclides more dangerous than tritium. These limits are fixed by the EURATOM Council Directive [52].

All limits mentioned in this section are summarized in table 1.5.

Country/Agency	Legal limit of tritium (Bq/L)
ICRP	76, 103
WHO	10, 000
Switzerland	10, 000
Canada	7, 000
Russia	7, 700
Australia	76, 103
Finland	30, 000
United States	740
European Union	100

Table 1.5: Legal limit of tritium in drinking water established in each country.

## 1.4 This thesis



# Chapter 2

## Tritium Detection Systems

### 2.1 State-of-the-Art

Measurement of tritium activity is one of the systematic environmental controls that have been carried out for dozens of years in the vicinity of nuclear research facilities and nuclear power plants during their energy production lifetime.

Consequently, this measurement has been attempted with many different technologies so far in order to constantly improve the state of the art in tritium detection. The most used techniques are summarized in Table 2.1.

Nowadays, the most used technic for measuring tritium in water is the liquid scintillator counter, LSC. It consists of mixing a liquid sample (some ml for environmental measurements or less for higher activities) with liquid scintillator. In LARAM, laboratory of the University of Valencia, this mixture is usually made in a ratio of 50:50 [53] but it depends on the detection system and the samples used [54, 55]. In this technique, the  $\beta$

	LSC	IC	Calorimetry	BIXS
Measured quantity	Scintillation photons	Ionization current	heat	X-rays
LDL	$\sim$ Bq	10 – 100 kBq	$\sim$ GBq	$\sim$ MBq
Sample form	Liquid	Gas, vapor	All	All

Table 2.1: State-of-the-art in the tritium detection for different techniques. This table show the measured quantity, low detection level (LDL) and the sample form for four different technics, liquid scintillator counter (LSC), Ionization Chamber (IC), Calorimetry and the beta induced X-rays Spectrometry (BIXS)

energy that is emitted from the sample excites the molecular energy levels of the liquid scintillator which promptly decays emitting several photons with a well-known energy (fluorescence), usually in the visible spectrum. Finally these photons are detected with photosensors, which convert the optical signal into measurable electrical charge.

The liquid scintillator technique has a very good detection sensitivity for low activity levels of tritiated water ( $< 1\text{Bq/L}$ ) [56] but it has the problems of long measurement delays (up to 2 days) and of producing chemical waste, as liquid scintillator contains toluene which is toxic. In addition, this technique requires special staff for sampling, chain-of-custody and lab analysis which consume economical and time resources. In order to avoid the last problem some unsuccessful efforts have been made in order to build a monitor of tritium with LSC [57].

The ionization chamber (IC) is based on gas chamber (sample) which contains electrodes connected to different voltages. These electrodes collect the ionization current that is produced due to the  $\beta$  radiation. It is a simple and fast system, but it has the problem of high Low Detection Limit ( $> 10 \text{ kBq}$ ) and of requiring the samples to be in a state of gas or steam [58, 59].

The calorimetry is based on the measurement of the heat generated

in the detection medium (normally platinum) [60, 61]. The problem with this technique is that it has a too high LDL, of the order of GBq, and too long measurement time, 2 days or more.

The Beta Induced X-ray Spectrometry (BIXS) is based on the measurement of the bremsstrahlung radiation produced by the tritium decay electrons, using a NaI(Tl) crystal couplet to a PMT [62, 63] or Silicon Drift Detector (SDD) [64]. The problem with this technique is that it has too high LDL, of the order of MBq.

There are many more different methods for tritium detection, although they are less used or less experimentally developed, each one with their own advantages and limitations. For example, the Avalanche Photo-Diode, APD, [65], which we cannot be use in contact with water, the mass spectrometry [66], which needs to store the sample several months before taking the measurement or Cavity ring spectroscopy [67], which requires a special optical configuration that is not possible outside the laboratory.

It is necessary to keep in mind that all these techniques are offline methods that take too long to measure the activity of the samples, including the time for the sample collection and shipment to the laboratory. These techniques cannot be used for in-situ monitoring of tritium in water.

The liquid scintillation technique is, however, the only one with low enough Low-Detection-Limit to check the compliance of 100 Bq/L in tritium of the water samples, established by the EURATOM directive.

The purpose of the TRITIUM project is to develop an alternative method, based on solid scintillators, that allows to accomplish the requirements of in-situ monitoring of levels as low as the legal limit in Europe 100 Bq/L in quasi-real time. There are several studies that have developed with solid scintillators so far:

- First study was done by M. Muramatsu, A. Koyano and N. Toku-

naga in 1967 who used a scintillator plate read out by two PMTs in coincidence [68].

- The second study was carried out by the A. A. Moghissi, H. L. Kelley, C. R. Phillips and J. E. Regnier in 1969 that used one hundred plastic fibers coated with anthracene powder and read out by two PMTs in coincidence [69].
- Third study was performed by R. V. Osborne in 1969 who used sixty stacked scintillator plates read out by two PMTs in coincidences [70].
- Fourth study was done by A. N. Singh, M. Ratnakaran and K. G. Vohra in 1985, who used a scintillator sponge read out by electronic coincidence [71, 72].
- Fifth study was carried out by K. J. Hofstetter and H. T. Wilson in 1991, who did different experiments for testing different shapes of scintillator plastic like several sizes of beads, fibers, etc. The better result which Hofstetter got for solid plastic scintillator was a tritium detection efficiency of the order of  $10^{-3}$  [73, 74].

	Efficiency, $\eta_{det}$ ( $cps/(kBq/L)$ )	Surface $F_{sci}$ ( $cm^2$ )	Specific efficiency $\varepsilon_{det} =$ $\eta_{det}/F_{sci}$	LDL (kBq/L)
Muramatsu	$3.85 \cdot 10^{-4}$	123	$3.13 \cdot 10^{-6}$	370
Moghissi	$4.5 \cdot 10^{-3}$	$> 424.1$	$< 1.06 \cdot 10^{-5}$	37
Osborne	0.012	3000	$4 \cdot 10^{-6}$	37
Singh	0.041	3000	$1.37 \cdot 10^{-5}$	$< 37$
Hofstetter	$2.22 \cdot 10^{-3}$	$\sim 100$	$< 2.22 \cdot 10^{-5}$	25

Table 2.2: Results of different scintillator detector for tritiated water detection

The results of these experiments are summarized in Table 2.2. We can see in the first column that the intrinsic detector efficiency,  $\eta_{det}$ , is

very different in these experiments. As it is known that, in this type of detectors, one of the most important factor, which affects the efficiency, is the active surface of the plastic scintillator,  $F_{sci}$ , and we can see in the second column that it is very different in each detector, we use the specific detector efficiency (third column), in order to compare these experiments, that's, the intrinsic detector efficiency normalized to this active surface. Now we can check that, effectively, these specific efficiencies are quite similar. One of the best specific efficiency was obtained by Moghissi who used scintillating fibers. This is a good point which justify our choice about using scintillating fibers as a detection medium. Finally we can see in the last column that the LDL in all these experiments are of the same order of a few tens of kBq/L so developing a detector which overcome these LDL values is essential for the compliance of the EURATOM directive of 100 Bq/L of tritium in water for human consumption.

## 2.2 TRITIUM Project

As we have seen in section 2.1, the current technique that exist nowadays cannot be used for tritium monitoring in quasi-real time since they have either higher LDL than the limit established by Council Directive, 100 Bq/L, or they are a off-line method (too slow).

As a result of these limitations appear the *Tritium* project [75], whose title is "Design, construction and commissioning of automatic stations for quasi-real time monitoring of low radioactive levels of tritium in water".

This project has been funded by Interreg Sudoe program of the European Economical Community, EEC, in the 2016 call with the reference number SOE1/P4/EO214. The purpose of this project is the development of a tritium monitor in quasi-real time. This monitor consists of a ultra-pure water system, which prepare the sample before introducing it in our detector, the tritium detector, where the tritium measure will be done, the cosmic veto and the pasive shielding, which reduce the natural background of our tritium detector, and several types of electronic which control all these parts of the monitor, analyze the tritium measurement and will send an alarm if the configured limit (100 Bq/L) is overcome.

The difficulty when the measurement of tritium is done is to distinguish these signals from the background. This is because tritium signals are small since tritium events has low energy ( $\sim$  keV) and this is the energy range in the spectrum where there are more background counts (the lower energy in the spectrum, the more electronic noise). To reduce the background counts of TRITIUM monitor, coincidence techniques will be used.

Finally this monitor will be installed in the Arrocampo dam, Almaraz, Spain, where the Almaraz nuclear power plant release the water



(a) Arrocampo dam and Almaraz Nuclear Power Plant      (b) Tajus river along Spain and Portugal

**Figura 2.1** – Arrocampo dam, Almaraz NPP and Tajus river

which is used in their cooling system, Figure 2.1. This NPP has two nuclear reactors whose type is PWR. Arrocampo dam, shown in Figure 2.1a, is located near the Tajus river, which is the largest river in Spain, 1007 km. This river cross from Aragon (Spain) to Lisbon (Portugal) and flows into the atlantic ocean, shown in Figure 2.1b. This river is used for an important quantity of animals, plants and even humans because the water of this river is used as drinking water by the spanish and portuguese people. Therefore the international cooperation in order to maintain the quality of this water is very important.

As it has been said, the *Tritium* collaboration is a international group consisting of a consortium of 6 different southwestern european institution of 3 different countries: The University of Aveiro, in Portugal, The University of Bordeaux and the National Center for Scientific Research, CNRS (Section Aquitaine-Limousin), in France and the University of Extremadura, *Junta de Extremadura* and University of Valencia, in Spain.

#### FOTOOS PERSONAS TRITIUM

Each institution has focused in the development of a different part of all this project:

- First, the Extremadura group has developed and installed the ultrapure water system with which water with very low conductivity,  $\sigma \approx 10 \mu\text{Sv}/\text{cm}$  (two orders less than sample before the cleaning process,  $1000 \mu\text{Sv}/\text{cm}$ ) is achieved. This clean process is very important for two reasons. On the one hand, it is important for maintaining our detector very clean, which is a critical point. On the other hand, it's important because with this process the natural background is reduced since several natural radioactive isotopes that there are in this water (except tritium) are removed, such as  $^{222}\text{Rn}$ ,  $^{40}\text{K}$  or  $^{137}\text{Cs}$ . This system will be explained in section 3.3.
- Second, french group has developed the passive shielding where our detector will work inside. It is based in ultra radiopure lead with very low intrinsic activity. The objective of this passive shielding is to reduce the external natural background that affect to our system. Obviously, this shielding doesn't have to affect to the measurement of our system, this is why radiopure elements with very low intrinsic activity are used (lead in the TRITIUM case). This shielding will be explained in section 3.4.1.
- Third, The Portugal and Spain people has collaborated for designing, developing and building four different prototypes of tritium detector and active vetos for removing cosmic events. These prototypes and vetos will be explained in the chapter 5 and section 3.4.2 respectively.
- Lastly, The Portugal and Spanish people has also developed the simulations about this system. The environment chosen to develop these simulations is GEANT4, which is a simulation package. It consists in a extensive C++ library with which the geometry of our detector, the physical processes which happen there, etc. can be designed. This simulation will be explained in the chapter 6.

The tritium level to be measured follow the ALARA principle (As

Low As Possible Achievable) and to get it there are important characteristics which our tritium detector must have:

- *Compact.* This is important because in the place where this detector will be installed the useful space to be used is finite.
- *Thin active volume and large active area.* On the one hand, it have to be taken into account that, as it has been shown in Table 1.4 of the section 1.2, the mean free path of the  $\beta$  particle of tritium decay is very low so thin active volumes are needed. In the practice, Active thickness beyond the mean free path of the tritium will only contribute to the background. On the other hand, as it has been checked in section 2.1 the efficiency of this type of detector scales with the active area so it is needed to design our detector with the largest possible active area.
- *High sensitivity to tritium.* It has to be kept in mind that the tritium activities that will be measured are very low so it is needed to reduce as much as possible the non-detected tritium events.
- *High specificity to tritium.* The detector has to be able to distinguish the tritium signal of the signal of other radioactive elements which can be present in the initial sample.
- *Quasi-real time response.* It is important that our sistem can work in quasi-real time in order to detect any problem as fast as possible.
- *Rugged system.* Finally, It has to be take into account that the objective will be installing an automatical system which will work during a lot of years without specialized people so it is needed that our monitor are rugged.

In order to get the measurement in quasi-real time it is needed to work *in situ*, that's, in the same place that the sample is taken. Working *in situ* has some benefits for the detector such as faster and cheaper

maintenance since the sampling process, chain of custody, etc. are eliminated, more frequent measurements and safer monitor since the personal exposure dose is reduced, changes in activity levels can be detected quickly and possible errors due to specialized personnel are eliminated.

# Chapter 3

## Design Principles of the Tritium Monitor

### 3.1 Detector System Overview

The objective of the TRITIUM project is the design, development, construction and commissioning of an automatic station for real-time monitoring of low levels of tritium in water. To achieve this objective, the TRITIUM experimental group has developed a monitor that is based on several parts, listed below:

- The TRITIUM detector, which will be explained in chapter 5, is based on several modules that are read in parallel. Each module consists of hundreds of scintillating fibers, section 3.2.2, read by two coincident photosensors, section 3.2.3. These scintillation fibers are directly in contact with the water sample whose tritium level will be measured. The photosensors included in this study are photomultiplier tubes (PMT), section 3.2.3, and silicon photomultipliers (SiPM), section

### 3.2.3.

- The ultrapure water system, section 3.3, is used to condition the water sample before the measurement. This system removes all the organic particles that are dissolved in this water and all the particles whose diameter is greater than  $1 \mu\text{m}$  without affecting the level of tritium in the sample. It is important for two reasons, on the one hand because, as it has been seen in section 1.2, the mean free path of tritium in water is very short, 5 or  $6 \mu\text{m}$ , so it is important to avoid the deposition of this particles in fibers because this would prevent the tritium electrons from reaching the fibers. On the other hand some of this particles dissolved in the water sample are natural radioactive particles such as  $^{40}\text{K}$ , which increase the background of our detector so, due to the fact that the water sample has few tritium events, it is very important to reduce the background of our detector as much as possible.
- The background rejection system, section 3.4, is based on two different parts. On the one hand, a passive shield, section 3.4.1, which consists of a lead castle inside of which the TRITIUM detector will be located. It is used to eliminate the natural radioactive background that is found in the place where the TRITIUM detector will be located, generally the events with relatively low energy ( $< 200 \text{ MeV/nucleon}$ ). On the other hand, an active veto, section 3.4.2, which consists of two plastic scintillation blocks located inside of a passive shielding, above and below of the TRITIUM detector, which are read by several photosensors. The objective of this active veto is to remove the remaining high energy events ( $> 200 \text{ MeV}$ ) from the natural background, such as cosmic events, that can travel through the passive shield and affect to the tritium measurement. Contrary to what happens with low energy events, this events are difficult to stop so, the technique used to eliminate their contribution to the TRITIUM measurement consists of reading the TRITIUM detector in anti-coincidence with the active veto.

- A general electronic system that will be used to monitor all the different parts of this monitor and send an alarm if the legal limit of the tritium level, 100 Bq/s, is exceeded.

Each part of this monitor were subjected to several tests to ensure its correct operation and, after that, they were installed in the Arrocampo dam. The final objective will be to include this monitor in the network of automatic stations, REA, shown in section 1.1.

## 3.2 TRITIUM Detector

Due to the reasons discussed in section 2.1, the TRITIUM detector developed used to measure the tritium levels of water samples is a scintillator detector. It consists in a chain of three main elements:

- The scintillator, that is the material in charge of detecting the tritium event. A general particle (tritium in our case), ionizing radiation, hit this material and deposits part of their kinetic energy (or all, as in our case) in it through ionization and excitation processes. Part of this energy deposited is converted in photons, generally in the visible range.

The produced photons produced carry information about the particle detected, such as its energy, type, etc.

- The photosensor, which is the part of the detector in charge of detecting the photons produced by the scintillator that reach it (the more scintillated photons arrive to your photosensor, the better signal you have in your detector).

The most used photosensor in nuclear physics are PMTs and SiPMs which detects the photons produced in the scintillator (with an efficiency) and transforms it in electrons which are multiplied with a factor of around  $10^6$ . This millions of electrons form a electronic pulse whose properties has information of the photons that has been detected.

- The electronic system, which is the part of the scintillator detector in charge of processesing and analyzing (first analogically and then digitally) this electrical pulse of the photosensor. The output of the electronic system is useful information about the event detected such as a number, for instance the activity, or some kind of spectrum like energy spectrum.

In Figure 3.1 a scheme of a scintillation detector is shown. There, the scintillator material detects ionizing radiation and produces photons that will be guided by the reflector and the light guide to the photosensor. There, some of the photons that reach the sensible part of the photosensors will be converted and multiplied into millions of electrons that will form a electronic pulse. The output signal of the photosensor (electronic pulse) will be processed and analyzed by the corresponding electronics:

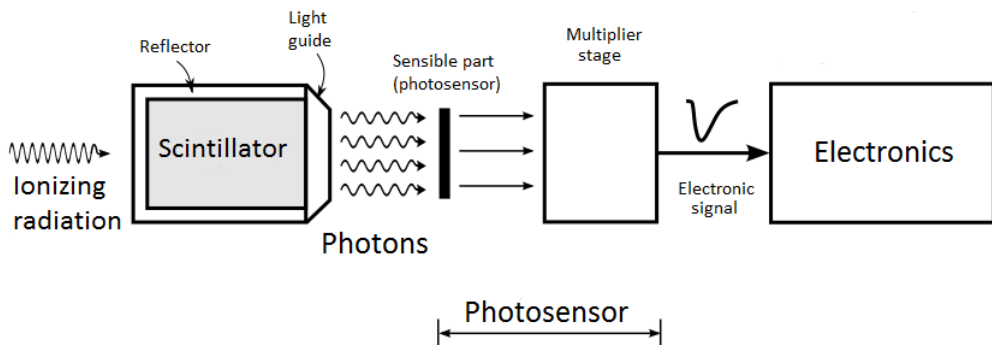


**Figura 3.1** – Scheme of the scintillator detector

### 3.2.1 Interaction of Fast Electrons and Photons with Matter

This section will explain the interaction of particles with matter. It will focus on the interesting particles and energy range for this thesis, which are electrons (0 – 18 keV) and photons in the visible range (approx. 380 – 750 nm).

On the one hand, electrons have charge so their interaction with matter is mainly produced with the orbital electrons of the matter through the Coulomb force. The electron trajectory is much more tortuous than other heavier particles because the mass of both interacting particles is equal, electrons. Furthermore, for the same reason, these electrons lost a significant amount of energy in each collision.

In order to speak about the total energy lost of particles in matter the specific energy loss is defined as  $S = -\frac{dE}{dx}$  which expresses the energy loss suffered by the particle per unit of trajectory. In the case of electrons, this total energy loss has two main contributions, the collisions (elastic and inelastic) and radiative processes (bremsstrahlung):

$$\frac{dE}{dx} \approx \left( \frac{dE}{dx} \right)_c + \left( \frac{dE}{dx} \right)_{br} \quad [76, 77] \quad \frac{\left( \frac{dE}{dx} \right)_{br}}{\left( \frac{dE}{dx} \right)_c} \approx \frac{EZ}{700} \quad [76] \quad (3.1)$$

Where  $E$  is the energy of the electron in MeV and  $Z$  is the atomic number of the absorbing material. Due to this energy loss, the electrons can only penetrate a material as far as they go before losing their total kinetic energy. This distance is known as range and, in the case of tritium electrons, its value is seen in Table 1.4.

On the other hand, photons don't have charge. Its possible inter-

actions with the matter are photoelectric effect, Compton effect, coherent scattering and pair production and the probability of each process depends on the energy of the photon,  $E_\gamma = h\nu$ , and the atomic number of the material, Z, as can be seen in Figure 3.2.

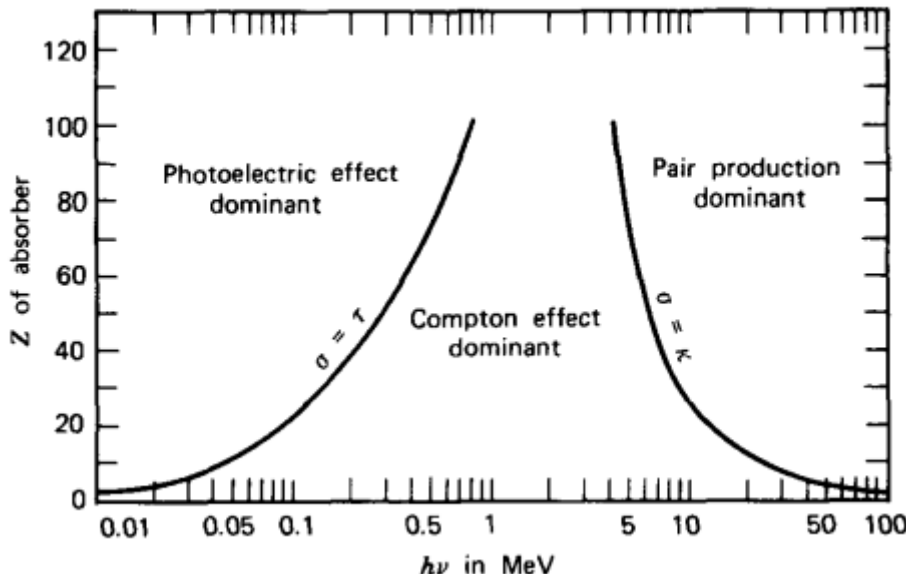


**Figura 3.2** – Domain regions of the three most probable types of interactions of gamma rays with matter. The lines show the values of Z and  $h\nu$  where the two neighboring effects are equally likely. [76, 77]

We have to take into account that the only relevant photons for this thesis are in the visible range, between 400 and 700 nm, that corresponds with energies of the order of the eV. Therefore the last effect, pair productions, will not be explained here because it requires a photon energy equal or more than 1.022 MeV.

The photoelectric effect occurs when a photon interacts with an orbital electron in the material, losing all its energy. This energy is absorbed by the electron that is released from the atom (ionization). The energy of the resulting electron,  $E_e$ , is:

$$E_e = E_\gamma - E_b \quad [76, 77] \quad (3.2)$$

Where  $E_b$  is the binding energy of the electron in this material. The probability of this effect depends on the number of available electrons in the matter through the variable Z, and the energy of the electron according to the following expression:

$$(Pr)_{Ph-eff} \approx \frac{Z^n}{E_\gamma^{3.5}} \quad [76] \quad (3.3)$$

As we can see in this expression and in Figure 3.2, the photoelectric effect is most probably if we use elements with high atomic number. This is the reason why elements with high atomic number are the best insulators against gamma radiation and this is the reason why the passive shielding of TRITIUM monitor consists of lead bricks ( $Z = 82$ ), shown in section 3.4.1. This is also the reason why elements with high atomic number like Sb ( $Z = 51$ ), Rb ( $Z = 37$ ) or Cs ( $Z = 55$ ), are used in the cathodes of PMTs.

The Compton effect occurs when the photon interacts with an orbital electron of the material, transferring part of this energy to the electron, which is released, and this photon is scattered at an angle  $\theta$  with respect to the original direction. If we neglect the binding energy, the energy transferred to this electron,  $E_e$ , is shown in the following equation:

$$E_e = \frac{\frac{E_\gamma^2}{m_0 c^2} (1 - \cos\theta)}{1 + \frac{E_\gamma^2}{m_0 c^2} (1 - \cos\theta)} \quad [76, 77] \quad (3.4)$$

Where  $m_0$  is the rest mass of the electron and  $c$  is the speed of the light in the vacuum. The probability of the Compton effect is proportional

to the atomic number (available electrons in the matter),  $Z$ , and decreases with the energy of the photon.

As we can see in Figure 3.2, in the energies of the photons belonging to the visible range of the electromagnetic spectrum (of the order of eV), the Compton effect is only more likely in very light materials, ( $Z < 4$ ). For heavier materials the photoelectric effect is the dominant effect.

Finally, in the coherent scattering, the atom is neither excitation nor ionization and the photon conserve all their energy in this collision. It is more probably for photons with low energies and materials with high atomic numbers and, as it will be shown in section 3.2.2, it explains why the produced photons are guided into the scintillating fibers.

### 3.2.2 Plastic Scintillators

The use of scintillators in radiation detection is one of the most used technics in nuclear physics. The scintillator is a material that is able to convert the kinetic energy of the incoming particles in light<sup>1</sup> which can be detected and quantified. It happens because the radiation excites and ionizes the scintillating atoms which, after that, are immediately de-exciting (with times of the order of picoseconds), emitting photons.

This conversion should be linear in a wide energy range of incoming particles and it is necessary that this material has good optical properties, such as being transparent to the wavelenght of their own emission and having a refractive index as close as possible to the glass for optimizing optical coupling with photosensors.

The photon emission in the scintillator is a statistical process, which means that two exactly same events will emit different number of

---

<sup>1</sup>The light is made up of photons in the visible energy range.

photons. It follow a poisson statistics so when we speak about the number of emmited photons we speak about the mean of the distribution.

There are two types of scintillators, organics and inorganics. Inorganic scintillators normally have a higher atomic number and density so their light output are higher. Due to these reasons they are better for gamma-ray spectroscopy (take into account Figure 3.2). Organic scintillators are generally faster and they are commonly used for beta spectroscopy and neutron detection. This section is focussed on organic scintillators since they are the ones used in the TRITIUM project.

Organic scintillators are based on a scintillator material, which produces light, dissolved in a base solvent. This solvent is normally based on aromatic hydrocarbons, that is, they are mainly composed of carbon and hydrogen atoms as we can see in the molecules of some of the most widely used scintillators,  $C_{18}H_{14}$ ,  $C_{24}H_{22}N_2O$  or  $C_{15}H_{11}NO$  whose average atomic numbers are between 3,5 and 5.

The scintillator molecules, in which the organic scintillators are based, have the so called  $\pi$ -electron structure. The energy levels of their electrons are commonly illustrated with a Jablonsky diagram, shown in Figure 3.3, which show the fundamental single state,  $S_{0i}$ , where the valence electrons are, the excited single states,  $S_{jk}$ , and the excited triple states,  $T_{lm}$ . The energy difference between  $S_1$  and  $S_0$  states is around 3 or 4 eV, energy range of the visible photons. As it is shown in the figure, each energy states are subdivided in smaller energetic sublevels whose distance between them are around 0.15 eV. This finer energy structure is due to the excitations of molecular vibrational modes and they are expresed with the second index of the energy states.

Because of the reason that the distance between all energy levels and sublevels are larger than the termal energy, 0.025 eV, non-exciting

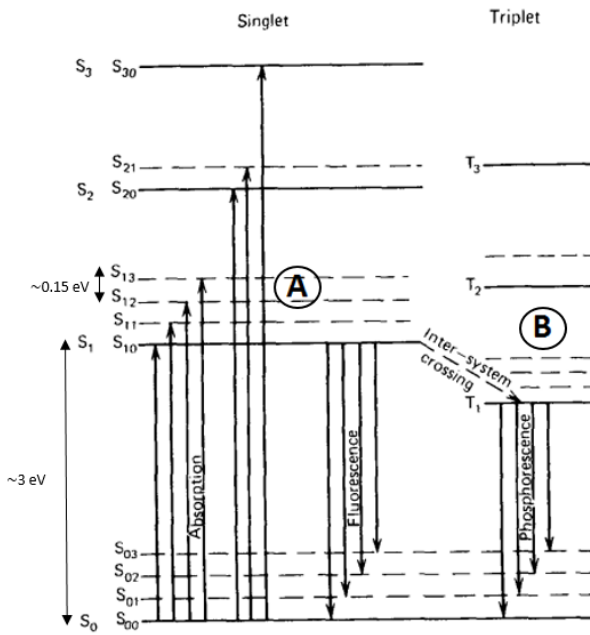


Figura 3.3 – Jablonsky diagram. [76]

electrons are in the lowest state  $S_{00}$  at STP<sup>2</sup>.

When a particle deposits their kinetic energy on a scintillator, their valence electrons are exited to higher single energetic states very fast (times of the order of picoseconds) which is expressed with upwards direction arrows in Figure 3.3 and they are quickly de-excited to the first single excited state,  $S_{10}$ , through non-radiative processes known as internal conversion.

Now, this electrons can de-excited to the fundamental single state,  $S_{00}$ , through three different physical mechanisms:

- The prompt fluorescence(process A in Figure 3.3), where the electron in the  $S_{10}$  energy level is de-excited to some sublevel of the fundamental state  $S_{0i}$ , emitting a photon with an energy equal to the energy

<sup>2</sup>Standar temperature and pressure conditions

difference of these levels (around 3 or 4 eV, visible light). This process happens immediately after the excitation of the scintillator molecules (around tens of nanoseconds after excitation). Each scintillator has a characteristic emission spectrum that defines its response due to the fluorescence mechanism.

Now we can understand why organic scintillators are practically transparent to their own fluorescence emission. This is because of the reason that there exist a quenching effect in each de-excitation process whereby there is a loss of radiated energy. Due to that, all emitted photons by the scintillator have less energy than the required energy for excitation. This effect is called Stokes shift and it is represented with a general spectrum in Figure 3.4.

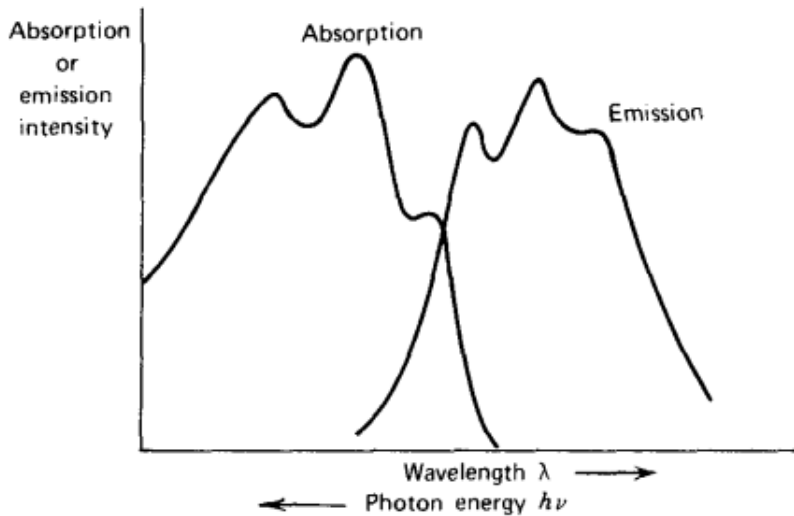


**Figura 3.4** – Stokes shift. [76]

The intensity of the fluorescence emission in an organic scintillator over time is a combination of two exponential functions, one associated with the lifetime of the level,  $\tau$  (on the order of nanoseconds), and the other associated with the energetic level population,  $\tau_1$  (on the order of picoseconds).

$$I = I_0 (e^{t/\tau} - e^{t/\tau_1}) \quad [76] \quad (3.5)$$

- The phosphorescence, where the electron that is in the first single excited state cross to a triple excited state (process B in Figure 3.3) with a process called "intersystem crossing". This is a metastable state with a much longer lifetime so electrons in this state are de-excited to the  $S_{0i}$  state, emitting a photon much later than phosphorescence. This process can happen up to  $10^{-3}$  seconds after scintillator excitation.
- Delayed fluorescence, which occurs when an electron is in a triple excited state but whose transition to the ground state is forbidden. In this case, this electron can interact with another that is in a similar state and return to the first single state and quickly de-excited to the ground state.



This emission has the same emission spectrum as immediate fluorescence, but occurs later.

The scintillating detectors generally use the prompt fluorescence light as useful signal so a good scintillator should increase it and reduce other possible physical mechanisms. One of the most important parameters in nuclear physics is the scintillation yield<sup>3</sup>, which is the the number of photons emitted by unit of absorbed energy. It depends on the type of particle and all mechanisms which don't produce prompt fluorescence, like phosphorescence or delay fluorescence or even internal conversion, contribute to reduce this parameter. This factor is normally given by the manufacturer for mips<sup>4</sup>.

---

<sup>3</sup>The scintillation yield is a way of expressing the efficiency of the scintillator in converting the energy deposited by the particle into photons.

<sup>4</sup>The MIP, Minimum Ionized Particles, is a particle that has the speed that generate minimum ionization, that's, for example, electrons with 500 keV or more

Plastic scintillators are organic scintillators that has been dissolved in a solvent and polymerized. They are easy to machine and can take any desired shape during construction. Among the forms most used today we can find blocks, thin sheets, cylinders, etc.

The chosen shape for TRITIUM detector is the fiber, specifically, commercial fibers BCF-12 from Saint-Gobain Crystals Inc company [78]. This type of fiber was chosen as the result of a comparative study [79] among some of the best-known commercial manufacturers, such as Kuraray [80].

The BCF-12 fibers consist of a scintillated core, whose material is polystyrene, one of the most used solvents for plastic scintillators [76], with the possibility of surrounding it of a cladding of polymethylmethacrylate (PMMA) (smaller refractive index than core in order to achieve a critical angle) or a multicladding (second cladding) with even smaller refractive index.

When a particle deposits all or part of its kinetic energy, some photons are produced in the fiber core as a result of the scintillating process. The number of photons produced depend on the scintillation efficiency, whose value is around 2.4% for the fibers used (BCF-12), which means that 8000 photons will be produced per MeV for a mip (scintillation yield). For instance, for tritium electron, this fibers will release a maximum of around 148 photons (when tritium electron has the maximum energy, 18.6 keV), probably less because electrons with these energies are not mips.

These photons will shape the useful part of the response of the scintillator (fluorescence). The energy (or wavelength) of these scintillated photons follows the distribution of their emission spectrum which, for the used fibers, is shown in Figure 3.5.

After the production of scintillated photons, these photons will be guided to the sensitive part of the photosensor where they will be detected

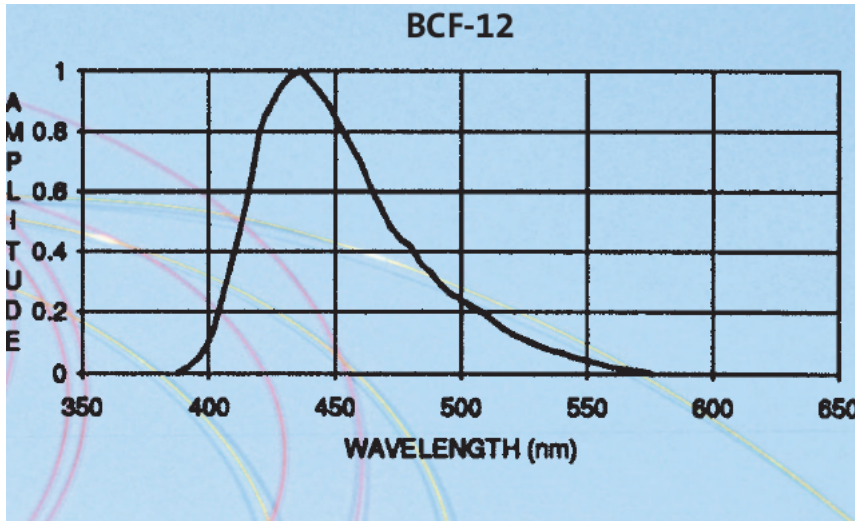


**Figura 3.5** – Emission spectrum of BCF-12 fibers of Saint-Gobain. [78]

with some probability. Fibers (and scintillators in general) use the optical property of Snell's law [81] to guide their photons to the desired part (ends of the fibers). It is based on the interface created between the core and the surrounding material. When a photon hits this interface, it is refracted (and therefore lost) following the Snell equation, 3.7. If the surrounding material has a lower refractive index than the core of the fiber, there exist a critical angle,  $\theta_c$ , at which, for angles equal or larger than this one, the photons will be totally reflected (and therefore conserved in the fiber for being guided). This effect is showed in Figure 3.6.

$$n_0 \operatorname{sen}(\theta_0) = n_1 \operatorname{sen}(\theta_1) \longrightarrow \theta_c = \operatorname{asen} \left( \frac{n_1}{n_0} \right) \quad (3.7)$$

There exist a parameter, called the trapping efficiency or photon collection efficiency, which define the efficiency of the scintillator to guide photons. For BCF-12 fibers with optical clad is between 3.44% and 7% per meter of fiber (depending if the event was detected near the fiber axis (minimum) or near the core-clad interface(maximum)) and for no clad fibers

BCF-12 surrounded by water, it is a bit larger but presents some problems as it will be seen.

Therefore, from these 148 photons initially created with the detection of the tritium electron with the maximum energy, only a maximum of around 41 photons (for maximum trapping efficiency) will be conserved in the 25 cm fiber length used in the TRITIUM detector. As can be appreciated, the output signal is very weak and this is the range of the spectrum where there is the most electronic noise. As will be seen in future chapters, a great effort has been made to minimize this electronic noise with various techniques.

In Figure 3.6 we can see how a scintillating fiber works.

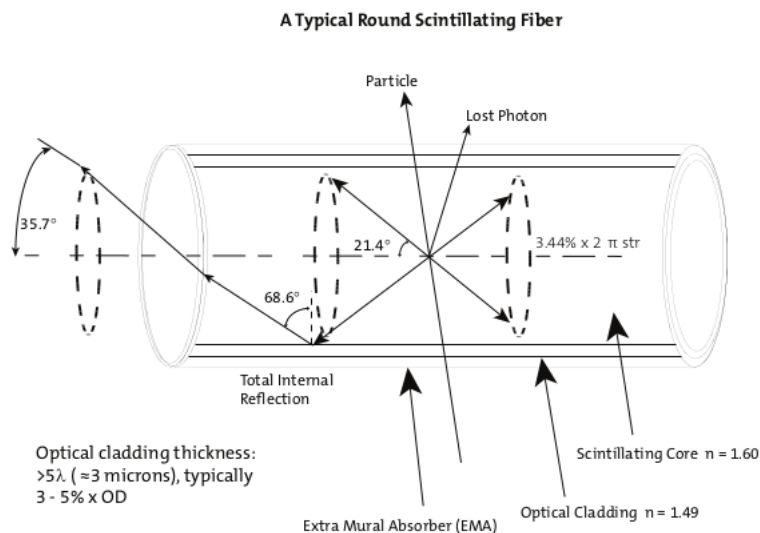


**Figura 3.6** – How photons are collected in a fiber with single clad. [78]

The cladding material is useful for protecting the core surface from dirt or aggressive external agents that can reduce the light collection but at the cost of losing some light because it increases the critical angle. Three different examples are shown in Table 3.1, where this effect is illustrated.

Material	Refractive index	critical angle ( $^{\circ}$ )
Air	1	42.98
Water	1.33	62.47
Cladding of PMMA	1.49	76.26

Table 3.1: Critical angles associated to different interfaces created with polystyrene,  $n_0 = 1.6$ , and other materials

In the practice, it's difficult to achieve a perfect air-core or water-core interface and it will affect to the light collection. Due to the reason that the commercial claddings are thicker (30  $\mu\text{m}$ ) than the mean free path of tritium in water ( around 5  $\mu\text{m}$ ) commercial cladding is not an available option for TRITIUM detector. Hence we will need to take special attention for achieving a water-core interface good enough. To overcome this problem, as we will see in section 4.2, we have used a special protocol developed in the ICMOL laboratories for preparing fibers before we use them for tritium detection.

Some of the most important parameters of the used scintillating fibers are summarized in Table 3.2.

### 3.2.3 Light Detection in Photosensors

So far we have created the scintillating photons in the core of the fiber, which have been guided to its ends. Now, what we need is the so-called photosensor, which is an element that is able to detect these scintillating photons. Photosensors have a sensitive part that is optimized to detect photons in a range of energy (normally inside of a visible range<sup>5</sup>) with enough efficiency. After that, the photosensors create an electronic signal that carries information about these photons detected, such as their number

---

<sup>5</sup>Photons whose wavelength is between 380 nm and 750 nm

Core material	Polystyrene
Core refractive index	1.60
Density (g/cm <sup>3</sup> )	1.05
Cladding material	Acrylic (PMMA)
Cladding refractive index	1.49
Cladding thickness ( $\mu\text{m}$ )	30
Numerical aperture	0.58
Trapping efficiency	3.44% minimum
No. of H atoms per cc (core)	$4.82 \cdot 10^{22}$
No. of C atoms per cc (core)	$4.85 \cdot 10^{22}$
No. of electrons per cc (core)	$3.4 \cdot 10^{23}$
Radiation lenght (cm)	42
Emission peak (nm)	435 (Blue)
Decay Time, (ns)	3.2
1/e Length (m)	2.7
Scintillator yield (# $\gamma$ /MeV)	$\sim 8000$
Operating Temperature	$-20^\circ\text{C}$ to $50^\circ\text{C}$

Table 3.2: Properties of BCF-12 fibers from Saint-Gobain Inc. [78]

or their detection time.

One of the most important things in the scintillation detector is that the emission spectrum of the scintillation (Figure 3.5 in our case) overlaps as much as possible with the detection efficiency spectrum of the photosensor used, specifically their higher peaks. In this case, the efficiency of this detector, which is proportional to the multiplication of both factors at the same photon energy, will be optimized (the largest).

There are a lot of different photosensors that can be used for this purpose, whose photon detection relies on totally different physical processes, such as photoelectron multiplier tubes (PMTs), silicon photoelectron multiplier (SiPM) or charge-coupled device (CCD). Each one of these will have different properties and we have to choose the one which fit better for

our objective.

Our main proposal for our scintillation detector will be to use SiPM arrays because they are very fast (of the order of nm) and have high photodetection efficiency (a maximum of around 50%) and high gains (multiplication factor of  $10^6$ ) with a low voltage supply. On top of that, one of the most important reason of this choice is that SiPM arrays are able to detect a single photon with high efficiency, which is very important since, as we have seen in section 3.2.2, just a few photons will arrive to the sensible part of the photosensor. We will test also the PMTs, which are the conventional choice, because they are still interesting since they have lower dark count rate than an equivalent SiPM and some similar properties like its gain.

## Photoelectron Multiplier Tubes (PMTs)

Photoelectron multiplier tube is one of the most used photosensors in nuclear physics during last decades. Its main objective, like all photosensors, is to detect the scintillating photons that reach its sensible part and convert it in an electronic signal large enough to be measured.

In Figure 3.7 we have a schematic drawing where we can see the PMT components and how it works. First of all, as we can see in Figure 3.7, we need to create electrons that will travel in the medium (electronic signal). To increase the amount of conserved electrons, we need to work inside a vacuum tube. Therefore, the PMT consists of a vacuum tube that has a glass window through which photons will penetrate inside.

The way in which PMT achieves their aim of detecting scintillating photons happen inside this vacuum tube and it is based in two different phases:

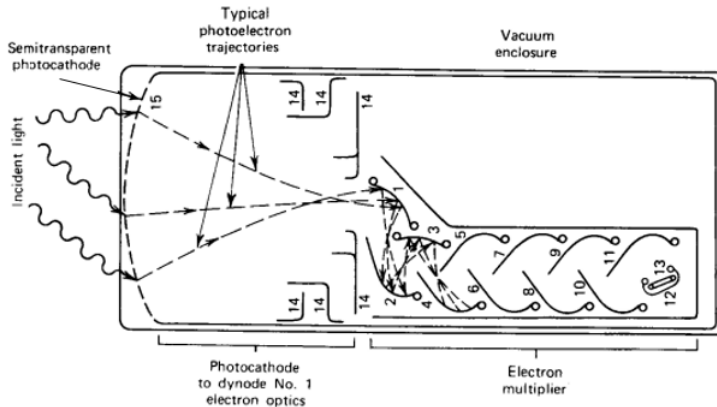


**Figura 3.7 – Scheme of a PMT. [76]**

- First, the PMT convert photons that reach its sensible part in electrons, called photoelectrons, with some probability through photoelectric effect. This sensitive part is the photocathode, which consists of a thin layer (thickness of the order of nanometers) deposited on the inner surface of the PMT windows. The material of the photocathode is chosen to increase the probability of producing photoelectric effect with the scintillating photons. The PMTs which we have used in this experiment are the model R8520-406 from Hammatsu [83]. The material of the photocathode in our case is Bialkali.

The response of the PMT at long wavelengths is limited mainly because the photon does not have enough energy to produce a photoelectric effect or the emitted photoelectron does not have enough energy to overcome the material-vacuum interface. The response of the PMT at short wavelengths is limited mainly due to absorption in the window material, quartz in our case. Due to both reasons, the response of the PMT will have a strong dependence with the energy of the photon and it's commonly expressed in the quantum efficiency (QE) spectrum which is the quotient between the number of photoelectrons produced at the cathode of the PMT and the number of photons reaching it. For our PMTs, is showed in Figure 3.8.

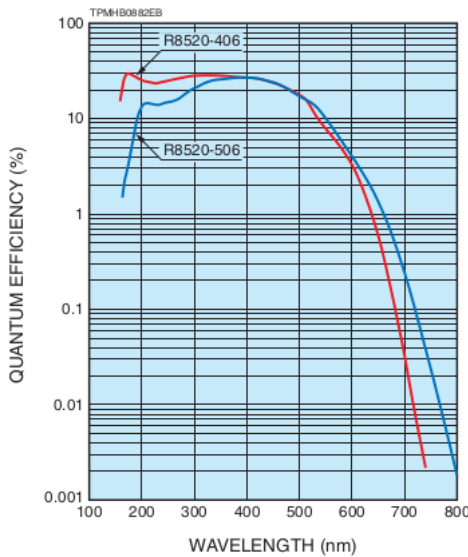


**Figura 3.8** – Quantum efficiency spectrum for the PMT used (R8520-ZB277). [83]

The maximum values of the PMT quantum efficiency is commonly between 20% and 30% [76] (a little bit less than 30% in our case [83]). If we compare the emission spectrum of our scintillating fibers, Figure 3.5, with the quantum efficiency spectrum of the PMTs that we have uses, Figure 3.8, we can see that the peaks of the spectrum are more or less in the same position (435 nm for the fibers and 420 nm for the PMT and approximately the same value for 435 nm). As I said in subsection 3.2.3, it is very important for increasing the overall efficiency of our scintillation detector.

- Next, Due to the reason that the number of photoelectrons in the photocatode is very small, we need a electron multiplication stage to achieve a large enough electronic signal to be processed by the electronic system.

This stage is based on three elements, focusing electrodes, dynodes and anode: They are metallic sheet whose shape and position are designed to optimize the collection of the electrons. The PMT needs

a high voltage (HV) which are distributed between all this elements, including the photocathode, in a increasing voltage way in order to attract and accelerate the electrons. This voltage division is achieved with an electronic circuit than can be fed with positive voltage (ground in the photocathode) or negative voltage (ground in the anode). The commercial electronic circuits of Hammatsu are showed in Figure 3.9.

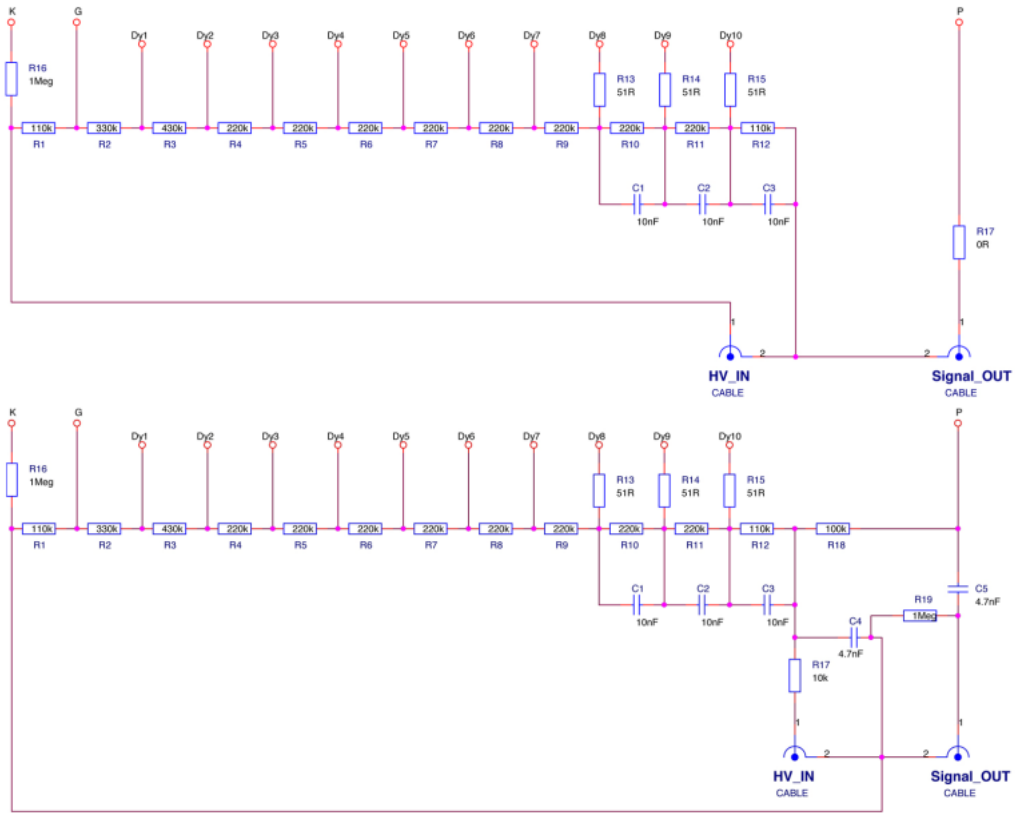


**Figura 3.9** – Hamamatsu commercial voltage divider electronic circuit. Upper circuit with negative supply and lower circuit with positive supply. [83]

The electronic circuit that can be supplied with negative voltage is faster due to the absence of the capacitances C4 and C5, but the other circuit, supplied with positive voltage, can be interesting for other tasks such as measurement of PMT currents. We will use both,

depends on the objective of the study.

Focusing electrodes are used to get the photoelectrons to reach the first dinode. Therefore, they have an collection efficiency (CE) that is defined as the quotient between the number of photoelectrons reaching the first dinode and the number of photoelectrons leaving the photocathode and whose value is around 80% for PMTs.

The dynodes is the part where the multiplication takes place. They have different voltage between each dynode in order to accelerate the electrons sufficiently so that, when the electron hit the each dynode, several electrons are emitted. The multiplication factor,  $\delta$ , is the multiplication of electrons in each dinode and its value is commonly around 5 and it has a strongly dependence with the HV. If we take into account that the PMT has N dynodes, commonly N=10 and we guess that each dynode has de the same gain,  $\delta$ , the overall gain of the PMT is:

$$G = CE \cdot \delta^N \quad [76] \quad (3.8)$$

If we use the numerical values mentioned in this section, we can see that the overall gain of a general PMT will be of the order of  $10^6$ . It is important to mention that this value depend strongly on the HV used.

We have to take into account that the uncertainty of the output signal with this gain is much greater than without it. That is the reason why, there are some times that it is interesting to work without gain such as when we try to count the number of photons that reach our PMT. We can achieve it with a small modification of the electronic voltage divider circuit 3.9. As we will see in section 3.2.4, it consists of short-circuiting all the dindes and the anode. In this way we are collecting the signal in the photocatode in which no amplification has occurred. We will use this voltage divider circuit without gain in our study with fibers.

Finally, when the amplification is used, the anode is the point where the collection of all the electrons produced in this multiplication process takes place and it is the one that gives rise to the output signal of PMTs.

Due to the fact that all intermediate factors (photoelectric effect and multiplication of electrons) are linear, the output signal of a PMT will be linear with the number of photons that reach its sensitive part. It will occur until a large number of photons reach the photocathode at the same time, where saturation will occur and linearity will be lost. This limit depend on the specifically PMT which we are using. This output signal has a spread of the order of tens of nanoseconds.

The multiplication of electrons can be described as a Poisson statistical process, so, for each electron in the first dinode, we will have  $G$  new electrons whose variance will be approximately  $\sqrt{G}$ .

Finally, we have to take into account that the photocathode can emit electrons whose origin doesn't belong to the scintillation light. This signal, which is named dark current, can happen due to several reasons like cosmic radiation, light from environment or thermoionic emission (the dominant) and, for our PMTs, this value will be around 2 nA according to Hamamatsu data sheet.

The calibration of the most important parameters (for our objective) of the PMTs used, which are dark current, gain for several HV and quantum efficiency, have been done at IFIC in the framework of NEXT experiment [82].

### Silicon Photoelectron Multiplier Array (SiPMs array)

The Silicon Photomultiplier (SiPM) is a photosensor, based on semiconductor materials, which has been developed in recent decades and they are replacing conventional PMTs in some experiments or applications. They have been designed to archive outstanding photon-counting capabilities better than conventional PMTs with high gain and high photodetection efficiency equal to or larger than conventional PMTs but with some important differences like insensitiveness to magnetic fields, low operating voltage, compactness among other differences.

### Semiconductor materials

Silicon is a semiconductor material and, like any semiconductor material, it has an electronic band structure that consists of two bands: Valence band and conduction band which are separated by a forbidden energy gap (with width of around 1 eV for semiconductors [77]) where there cannot be electrons (there are not available energy levels). These energy bands are based on many energy levels that are so close that we can consider a continuum. You can see a diagram of these bands in Figure 3.10.

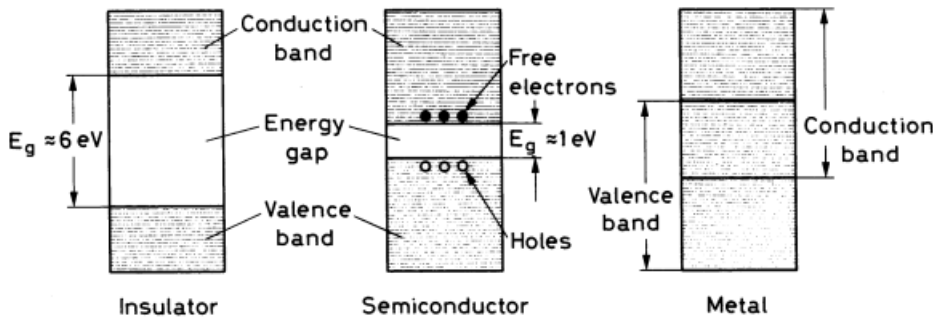


**Figura 3.10** – Energy band scheme for (a) insulator, (b) semiconductor and (c) conductor. [77]

Electrons in the conduction band, unlike those in the Valence band, can move freely in the material so they contribute to the electric current.

Silicon has four electrons in their valence band (tetravalent atom) so it forms four covalent bonds creating a crystal lattice ( $\text{Si}_2$ ). Normally a small quantity of impurities ( $10^{13} \text{ atoms/cm}^3$ ) compared to its density ( $10^{22} \text{ atoms/cm}^3$ ) are added to modifying this lattice, that's doping the material.

If the dopant has 5 valence electrons (pentavalent atom like phosphorus or arsenic) there will be a free electron which will be at an energy level created in the forbidden band, very close to the conduction band. It is called "n-type" semiconductor and the electrons are the majority charge carriers.

Otherwise, if the dopant has 3 valence atoms (trivalent atom like gallium or boron) it will have a hole<sup>6</sup> that will be at an energy level created in the forbidden band, very close to the valence band. In this case, the holes are the major charge carriers and this element is called "p-type" semiconductor.

Both configurations (p-type or n-type semiconductor) are shown in Figure 3.11.

SiPM is based on a silicon diode formed by a junction of n-type and p-type semiconductors that is made with special techniques to achieve a good contact between both surfaces.

This union creates the so-called depletion zone, which is the interface between both materials. In this zone, there is a diffusion of electrons to the p-type semiconductor and holes to the n-type semiconductor due to the difference in the concentration of the majority charge. This re-arrangement of the charge creates an electric field in the depletion zone contrary to the movement of these charges, whose potential difference, called contact potential, is  $V_0 = 0.7 \text{ V}$  for silicon [77]. All this information is shown schematically in Figure 3.12

---

<sup>6</sup>Electron absence in the crystal lattice

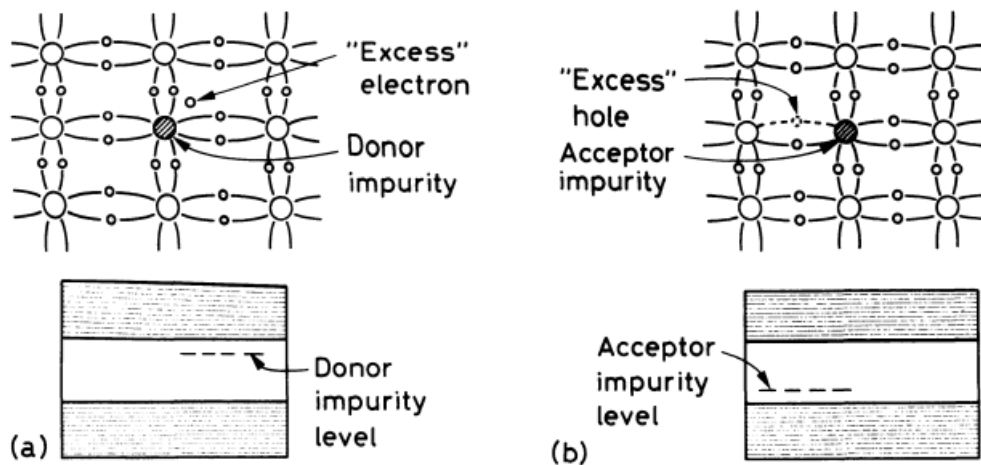


**Figura 3.11** – Crystal lattice and energy band scheme formed by a silicon with (left) a pentavalent dopant that creates an n-type semiconductor (right) a trivalent dopant that creates a p-type semiconductor. [77]

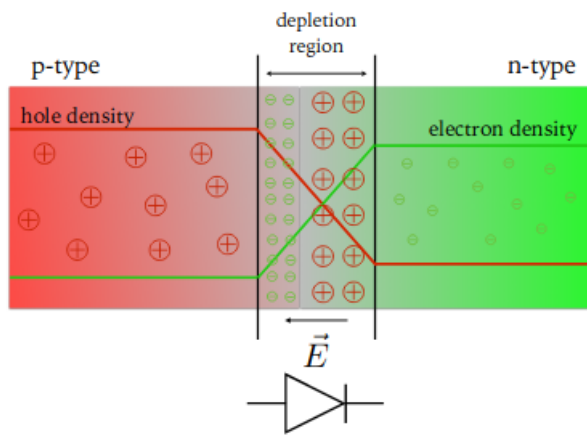


**Figura 3.12** – (Above) Schematic of the charge distribution and electric field created in a pn-junction. (Bottom) Commonly used symbol for a diode. [84]

There are no charge carriers in the depletion zone and, if any one are created, they will be swept out by the electronic field (special interesting property for radiation detectors since charge carriers are created in this zone when ionizing radiation crosses through it).

If we want to use this p-n junction as a particle detector, this setup has some problems that we have to overcome. On the one hand we need to prevent the charge recombination in order to optimize its collection in the depletion zone. On the other hand we need to increase the width of the depletion zone (it is  $0.5 \mu\text{m}$ , too small to stop interesting particles) and, as we will see in section 4.3, this small width increases the capacitance value that will increase the electric noise in the output signal.

We can overcome these problems if we apply an external bias voltage across the junction. If this bias voltage is with positive terminal in p-type semiconductor and negative terminal in n-type semiconductor, which is called forward bias voltage, it will create an additional electric field opposite the internal electric field, which will attract electrons in n-type towards p-type and holes in p-type towards n-type. In short, it will reduce the depletion zone, and if the applied voltage is greater than the contact potential, an electric current will be created even if no charge has deposited their energy in the depletion zone.

However, if this bias voltage is applied with positive terminal in n-type semiconductor, negative terminal in p-type semiconductor, which is called reverse bias voltage, the contrary effect will happen and the intensity of the electric field in the depletion zone will be increased. This effect will be limited by the resistance of the semiconductor and if we use a too large bias voltage the pn-junction will breakdown and it will begin conducting.

If reverse bias voltage is applied, we can solve all the problems mentioned above. In this case, the charge collection will be improved and the width of the depletion zone will be increased. If ionizing radiation crosses

the depletion zone, which is wide enough to detect interesting particles, it will deposit their energy and, due to that, charge carriers will be created<sup>7</sup> which will be swept due to the electric field and an optimized current signal will be created.

Depending on the intensity of the polarization voltage we can work in different modes and we will have different output signals. If the bias voltage is less than the threshold, the charge carriers will recombine and no output signal will be produced. If the bias voltage is larger than threshold an avalanche is created due to each original electron and it is independent of other possible avalanches. Due to this avalanche, it has a gain whose value is around 200. This mode is called proportional mode since the collected charge is proportional to the energy deposited. Finally, If the bias voltage is even larger, each avalanche can trigger a second avalanche and, due to that, their internal gain is higher than the proportional mode<sup>8</sup>, that's, its output signal will be larger. This mode is called Geiger mode since the output signal only shows when a detection has happened but it is not proportional to the energy deposited.

The voltage at which the SiPM changes from proportional to geiger mode is called the breakdown voltage,  $V_{BR}$ . If it works at a lower voltage it is in proportional mode but if it works at a higher voltage, it works in geiger mode. The measurement of the breakdown voltage is one of the most important things to characterize the SiPM and I show how we have done it in section 4.3.

### Silicon photomultiplier

The SiPM is based on a matrix of APDs which are photodiodes operating in geiger mode. A scheme of an APD used in a SiPM is shown in

<sup>7</sup>The energy required to create an electron-hole pair in silicon is 3.62 eV in STP[77]

<sup>8</sup>The gain of commercial SiPMs, for example Hamamatsu, is of the order of  $10^6$ , similar to the PMTs

Figure 3.13. It has p+ and a n+ layers<sup>9</sup> that are used because they improve the properties of SiPMs but the way these APDs work is the same as that described before.

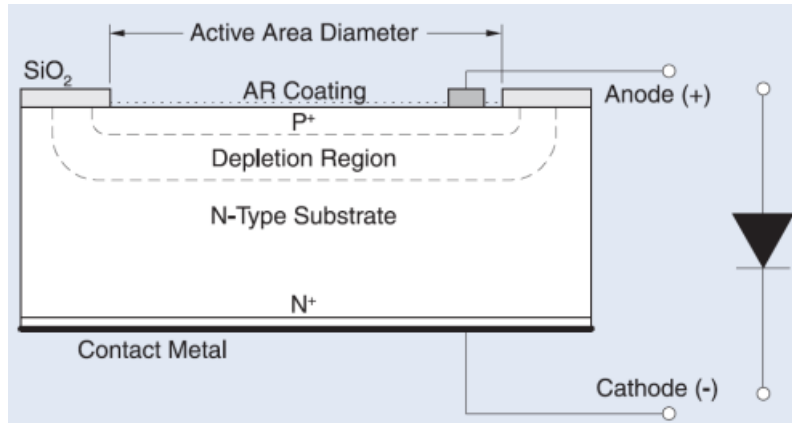


**Figura 3.13** – Scheme of a APD and electrical symbol used. [85]

These APDs, called pixels when they are part of a SiPM, are connected in parallel and we read the sum of all of them at each moment. The output signal of each pixel is approximately the same regardless of the energy deposited, with some difference due to the uncertainty in the SiPM manufacturing process and the statistical nature of the detection process. Due to that, we cannot know the energy deposited in each APD but, as we read all SiPM pixels at the same time, the charge of the output signal when we detect  $n$  photons simultaneously will be  $n$  times the charge we have when we detect only one photon, as can be seen in Figure 3.14. Due to this property, after a correct calibration of our SiPMs which will be shown in section 4.3, we can know how many photons we have detected, which have a linear relationship with the output signal.

Furthermore, as we saw in section 3.2.2, since we work with scintillators, in our case, the number of photons is proportional to the deposited

---

<sup>9</sup>p+ and n+ layers are the same as p and n layers, explained before, but with higher concentrations of acceptor impurities or donor impurities respectively CHECK THAT!!

energy, so we can recover the characteristic linearity of its output signal and to know the energy deposited in our scintillator, and, therefore, the energy of the initial radioactive event.

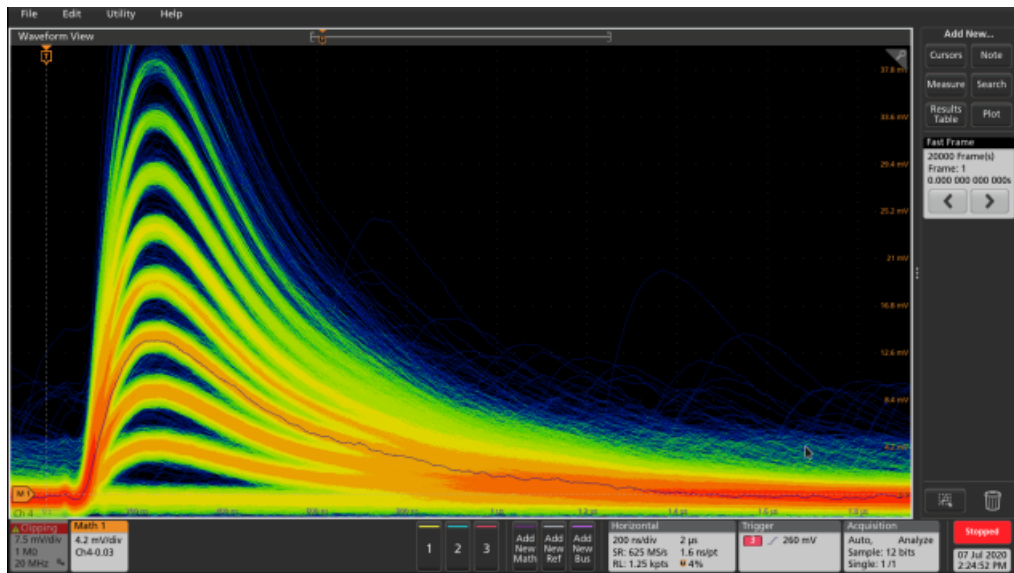


**Figura 3.14** – Using persistence on the oscilloscope to show several pulses with different heights. Each height associated with a different number of SiPM pixels lit at the same time.

On top of that, these pixels need to be so small<sup>10</sup> that, if the photon density to be detected is low enough, we only detect one photon in each pixel. If it doesn't happen, we will detect two or more photons with the same pixel but the output signal will be the same as one detected photon, so we will have a loss of linearity of our output signal. This effect is known as saturation and it is important to know the photon density at which it happens for our SiPMs. The experimental measurements of this effect, which have been done for our SiPMs, is shown in section 4.3. SI LA MIDO YO PERFECTO, SI NO DECIR QUE PARA NEUSTRO CASO NO ES IMPORTANTE PORQUEU ESTAMOS MIDIENDO MUY POCOS FOTONES POR EVENTO.

---

<sup>10</sup>Pixel sizes for commercial SiPMs are 50 or 75 $\mu\text{m}$  [86], [87]

Each of these pixels has a quenching resistance<sup>11</sup> in series that is used to stop the current produced when this pixel has detected a particle. It is used for limit the current drawn by the diode during breakdown and reduce the reverse voltage seen by the diode to one below the breakdown voltage. After that, the voltage seen by the diode is reset to the bias voltage and this pixel is ready to detect a new particle again. In Figure 3.15 (left) a diagram of these chenching resistances and APDs in a SiPM and (right) how it works is shown respectively.

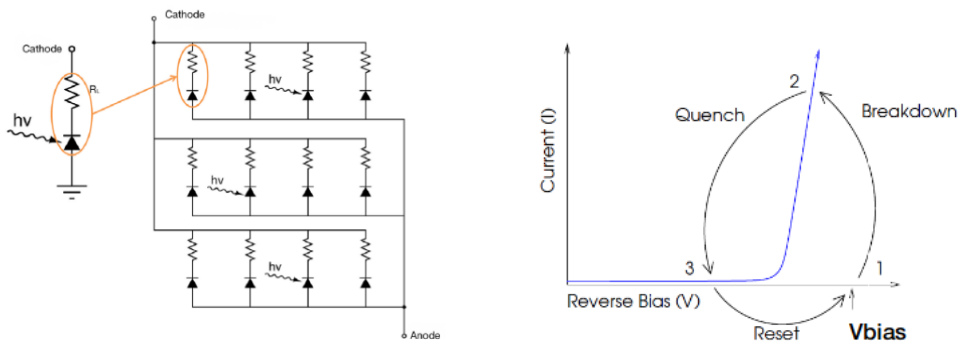


**Figura 3.15** – (Left) Electronic scheme of a SiPM and (right) output current of a SiPM as a function of the reverse voltage. It show that the quenching mechanism is essential for working with SiPMs [90]

In this simple electrical scheme we can see that all pixels have a common cathode and anode which means that, as we said before, they are at the same bias voltage and the output is the sum of all of them.

We have a lot of names to refer to these photosensors such as SiPMs, MPPCs, G-APDs, SSPMs, MRS-ADPs or AMPDs. The candidate for TRITIUM project is S13360-6075 from Hamamatsu photonics [87] because its characteristics are the ones that best fit our objectives since this model has super low afterpulses, crosstalk and dark counts than other SiPM models from Hamamatsu. Its characteristics and properties are shown in Table 3.3.

<sup>11</sup>The tipical valuer of this quenching resistance for commercial SiPMs is around  $500\text{ k}\Omega$

Parameter	Numerical value
Serie	S13360
Model	6075
Pixel Pitch ( $\mu\text{m}$ )	75
Effective photosensitive area ( $\text{mm}^2$ )	$6.0 \times 6.0$
Number of pixels	6400
Fill factor	82%
Refractive index of windows material	1.55
Operating temperature range ( $^\circ\text{C}$ )	$[-20, 60]$
Spectral response range, $\lambda$ (nm)	[320, 900]
Peak sensitivity wavelength, $\lambda_p$ (nm)	450
PhotoDetection Efficiency, PDE, $\lambda = \lambda_p$ (%)	50
Dark counts, Typical/Maximum (kcps)	2000/6000
Terminal capacitance, $C_t$ (pF)	1280
Gain, M,	$4 \cdot 10^6$
Breakdown Voltage, $V_{BR}$ (V)	53
Cross talk probability(%)	7
Temperature coefficient $\Delta TV_{op}$ (mV/ $^\circ\text{C}$ )	54

Table 3.3: Characteristics of SiPM S13360-6075 from Hamamatsu Photonics [87].

These characteristics and properties will be explained and their experimental measurements will be shown in section 4.3. These numerical values, which appear in Table 3.3, are provided by Hamamatsu photonics but it is only an approximation for this model. These parameters must be determined experimentally for each SiPM used because it can be very different even if it is the same model.

It must be taken into account that we will do this characterization at the level of a single SiPM because, at the beginning, it is easier to understand the results but we will work with a matrix of them and we will have to do this characterization for each matrix used.

The matrices under consideration are the model "S13361-6050" from Hamamatsu, which consists of a  $4 \times 4$  SiPM matrix where the active area of each SiPM is  $6 \times 6$  mm [88] or the model "S13361-3050" from Hamamatsu, which consists of a  $8 \times 8$  SiPM where the active area of each is  $3 \times 3$  mm [89]. They are a commercial matrices from Hamamatsu and, as you can see, the total active area that we will cover with these arrangements is the same in both cases,  $24 \times 24$  mm and it is approximately the same that the active area covered with the PMTs used, which has been shown in the previous section.

These matrices have a common bias voltage and common ground for all SiPMs that are contained and we will have an output signal for each SiPM.

We hope to obtain better results with the  $4 \times 4$  matrix for theoretical reasons which we will see in section 4.3 like larger PDE, mainly due to a larger active area but it is something that we will have to verify with experimental measurements.

Nuestro SiPM esta dopado? con que?

### Comparison of photosensors considered

As we have said before, we are going to use two of the most widely used photosensors in the world, PMT and SiPM. Each has some properties that are better than the other for our experiment and its own problems. We will have to test both and choose the one with which we achieve better results.

The output signal of both photosensors used is proportional to the number of incident photons and they have a similar internal gain (of the order of  $10^6$ ). Both properties are essential for our experiment in order to detect tritium events and obtain a signal large enough to be measured and processed.

They have fast output signals, whose rise time is shorter than nanoseconds, and a wide spectral sensitivity that is similar for both ([200 – 800] ns for PMT and [300 – 900] ns for SiPM).

The supply voltage necessary to work with SiPM, on the order of tens of volts, is much lower than that of PMTs, which require high voltage, that is, on the order of thousands of volts and the PDE at 420 nm, achieved with SiPM is higher, around 50%, than PMT, whose PDE is around 30%. A large PDE is essential because, as we have seen before, the number of photons that we will read in each tritium event will be very low, so we must detect as many photons in each event as we can.

Furthermore PMTs, due to the reason that they consist of a vacuum tube, are more bulky and fragile than SiPMs, which are compactness and robust. It is an advantage of the SiPMs because we want that our detector work during a lot of years so we need this to be durable. Furthermore, because PMTs are manually produced, they are much more expensive, thousands of euros, than SiPMs, tens of euros, which can be mass produced.

On top of that the behavior of the PMTs is affected by magnetic fields, something which doesn't happen with SiPMs with which it has been

tested that it can work correctly with magnetic field intensities between 0 and 7 Tesla.

In addition to that, due to their enormous uniformity, SiPMs are capable of distinguishing the exact number of photoelectrons detected and even resolving a spectrum of a single photoelectron, which is not possible with PMTs due to variations in their gain.

On the other hand, the dark current rate for PMTs is much lower (a few counts per second) than for SiPMs, whose dark current rate is between 0.1 and 1 Mcps<sup>12</sup> (depends on its size) and it happens almost entirely at the level of a single photoelectron. It is a problem of the SiPMs because we need to distinguish the tritium signal from this background. In addition to that, SiPMs have other properties, such as the crosstalk of the afterpulses, that must be measured and extracted since they can affect the correct measurement. We will see how to do it in section 4.3

Also, the SiPMs output signal is affected by a slight change in temperature, something which doesn't happen with PMTs. It is a serious problem of the SiPMs for our experiment because we will work in the field, where we cannot avoid such a low temperature change. As we will see in section 4.3 we will solve this problem with a suitable change in the supply voltage that compensates for this variation.

---

<sup>12</sup>Mega counts per second,  $10^6$ c/s

### 3.2.4 Electronic Readout

The last part we need to have a complete scintillator detector is the electronic system that is the part in charge of reading, processing and analyzing the output signal of the photosensor used and providing us with information that we can interpret.

This electronic system will depends on the type of the output signal of our detector. Therefore, it will be different for the different detector configurations that has been tested in our experiment. It includes PMT and SiPMs and these will be the parts in which this section is divided.

#### Electronical system for PMTs

In the different tests in which we have used PMT, we were interested in two different main objectives. On the one hand, we were interested in knowing the amount of incident photons that reached the PMT photocathode, which can be interesting, for example, to characterize fibers, and, on the other hand, we were interested in the energy of each event that occurred, which can be interesting, for instance, to obtain an energy spectrum or to discriminate events based on their energy (for knowing the origin of these events and counting only interesting events).

In the first case, if we want to know how many photons have reached the photocathode, we have to work without the internal gain of the PMT. The reason for this is that it introduces a large uncertainty in the measurement. The use of this internal gain could be interesting in other situations such as when we need to know the energy of the event because, as we saw in section 3.2.3, its use greatly enlarges our signal, a factor of the order of  $10^6$ , and, due to that, it is easier to process and analyze it.

For working without the internal gain of the PMT we need to avoid

the use of the electron multiplication stage that we saw in section 3.2.3. To achieve this, we design, build and test special PCBs, whose electronic scheme is shown in Figure 3.16, in which we short-circuit all the dindes and read the signal directly from the photocathode.

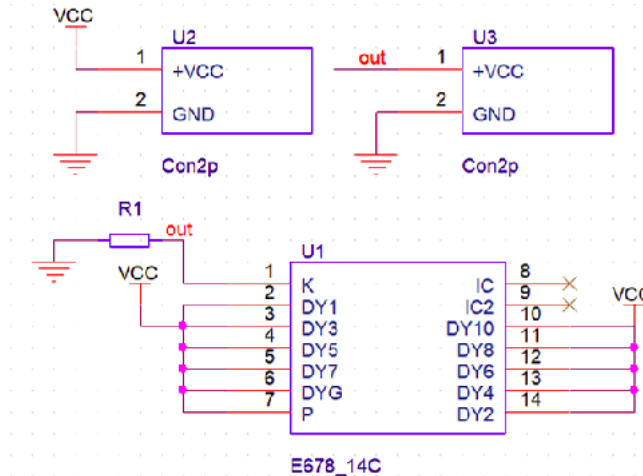


**Figura 3.16** – Electronic scheme of the electronic voltage divider circuit used for working with PMTs without its internal gain.).

This PCB is designed to be powered with positive supply voltage which is less than the normal situation [0 – 400 V]. The reason of this lower supply voltage is that we don't need to create a voltage difference between each pair of dynodes in the chain (we only need to create a voltage difference between the photocathode and the first dinode).

In this case, the output signal of our photosensor is very fast and small (currents of the order of tens of nanoamperes<sup>13</sup>) and we need a special system to analyze these types of currents. The system which we have chosen is Keithley 6487 Picoammeter/Voltage Source [91], which is a commercial system from the Keithley company, because it has some interesting options for this study such as automatic baseline correction, the ability to read

---

<sup>13</sup>1 A =  $10^9$  nA

signals as small as picoamps and the ability to perform some interesting mathematical operation, such as the average of N measurements with the associated statistical error, where N is programmable by the user ( $N = 100$  in all our studies).

With this configuration we can measure the output current of our photosensors and, from it, quantify how many photons have been detected by the PMT photocathode using the equation 3.9:

$$N^o \gamma / \text{sec} = \frac{(I_{PMT} - I_{DC})}{q_e \cdot QE \cdot CE} \quad (3.9)$$

Where  $I_{PMT}$  is the output current of the PMT when it detects photons and  $I_{DC}$  is the dark current of the PMT. This equation takes into account the quantum efficiency, which is close to 30% for the PMTs used, and the capture efficiency in the dyndes, which is equal to 1 because we read the signal directly from the photocathode. In addition, it is taken into account that, due to the photoelectric effect in which this detection consists, each detected photon only generates one electron, whose charge is  $q_e$ .

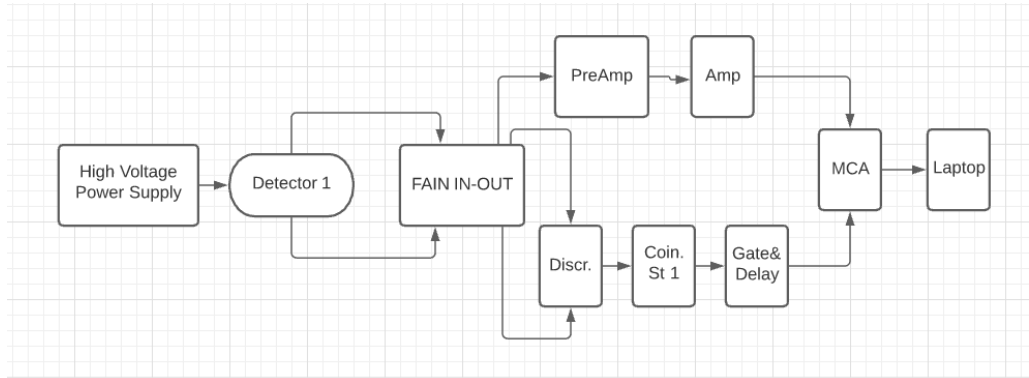
In the second case, if we want to know the energy of the event that occurred, we need to work with the internal gain of the PMT. For that we will use the electron multiplication stage that we saw in section 3.2.3.

In all our studies we have used several PMTs in our experiments (two or four depend on the case). The electronic schematics used, which are shown in Figures 3.17a and 3.17b respectively, are based on various NIM technology modules<sup>14</sup>.

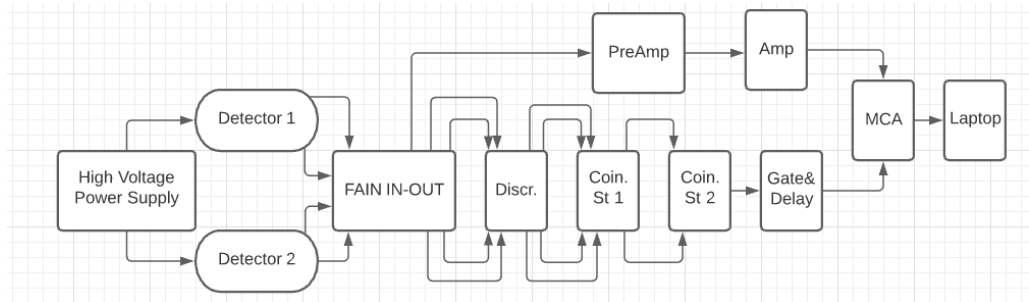
The PMTs used in each situation are feeded with the voltage supply "TC 952 High Voltage Supply" from Tennelec [92]. It has four channels

---

<sup>14</sup>The Nuclear Instrumentation Module (NIM) is a standard specification convention for electrical and mechanical parameters defined in electronic modules used in experimental nuclear and particle physics.



(a) Electronical configuraiton scheme used to measure with two PMTs.



(b) Electronical configuraiton scheme used to measure with four PMTs.

**Figura 3.17** – Schemes of different electronic configuration used to measure with PMT.

for feeding up to four different PMTs so it is enough for both configurations. In some situations we need to work with both configurations at the same time, that's, with six PMTs at the same time. In this cases other voltage supply had been used, called "HV Power Supply N 1130-4" from "Wenzel Elektronik" [93] company with which we get 4 additional channels for feeding PMTs. The high voltage used in each case will be named in each specific situation.

As you can see in Figures 3.17a and 3.17a, in both electronic configurations there are two different paths that must be followed by the output signals of each PMT, the amplification part and the time coincidence part.

Therefore, the first module we need is the analogic FAN IN-OUT module which is used to duplicate the input signal.

The module used is the "Quad linear FAN IN-OUT MODEL 740" module from the company "Philips Scintific" [94]. With this module we can obtain up to 4 output signals (we only need two) that are totally identical to each input signal. For each PMT we have two identical output signals. One will be used as the input for the amplification part and the other will be used as the input for the time coincidence part.

- The amplification part, which is the same for both electronic configurations, Figures 3.17a and 3.17b, is used to process and amplify the output signal. We have to take into account that we have only used the signal from one PMT for the amplification part. We could have added a stage where we add the four PMT output signals and it would probably improve our results, but since our ultimate goal is to work with SiPM, we have not delved into that.

The electronic path we have followed to achieve this amplification is:

1. One of the output signals of the previous module (FAN IN-OUT) is introduced in a preamplifier that is used to prepare the signal to be amplified, appendix B. The preamplifier used is "MODEL 9326 FAST PREAMP" from ORTEC [95].
  2. The output signal from the preamplifier is introduced into the amplifier where it will be converted to a positive signal with a shape close to the Gaussian function and an amplification factor will be applied. The amplifier modules used on this studies are "model 575A" and "model 671", both from ORTEC company [96], [97]. The output signal for 575A module is shown in Figure 3.19, green color.
- The time coincidence part is used to obtain the coincidence gate that will be used to indicate when we have to save the amplified signal

(which is when all the PMT output signals are in time coincidence). Only the saved output signal will be used for the analysis.

This part is practically the same in both cases with just one additional step when we use four PMTs. The electronic path followed in the time coincidence part is:

1. The second output signals of the FAN IN-OUT module for each PMT are introduced into a discriminator module where we obtain an output logic signal with height of  $-1.2$  V and width of 240 ns when a threshold, the one programmed by the user, is exceeded. The discriminators used in our experiments are "Octuple Constant-Fraction Discriminator CF8000" module from ORTEC company [98] and "4 channels discriminator model 84" from CAEN company. Some cases of these four output signals are shown in Figure 3.18 for four PMTs in coincidence.
2. Now is the time to make time coincidences. As we will see in section 3.4.2 and chapter 5, we have two photosensors in each detector, so we will do time coincidences in pairs of photosensors, PMTs in this case.

Therefore, each pair of output logic signals of the discriminator module (attached to two PMTs that are in the same detector) will reach a different channel of the coincidence module and generate an output signal, with a height of  $-1.4$  V and width of 20 ns, when a time coincidence has occurred on them.

This first time coincidence stage is used to remove the detection of external light or dark current of PMTs from the saved measurements. This is because this module only generate logic output signals when both PMTs have detected photons at the same time, indicating that these photons are coming from the coupled scintillator.

The time coincidence modules used are "Coincidence Unit Model 465" from LeCroy [100] and "Coincidence Type N6234" from

CERN-NP [?].

3. The next step, which is included only when working with four different PMTs, is used to do time coincidence between two different detectors. It could be interesting, for example, to detect hard cosmic radiation as we will be in 3.4.2 section.

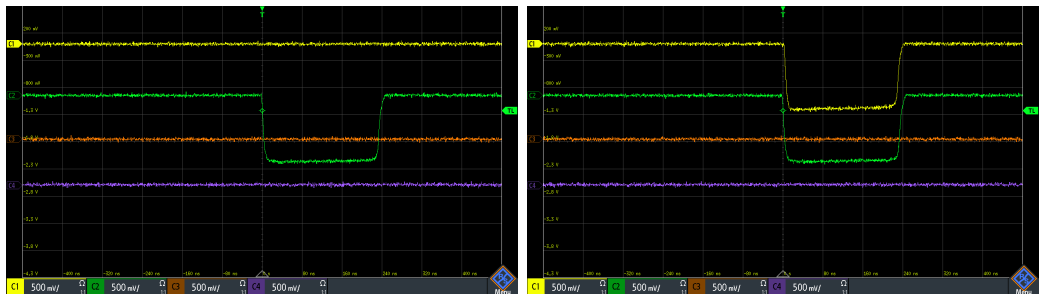
If we want to do time coincidences between both detectors, we have to use the logical output signals of the previous step (output of the coincidence module) as input of another coincidence stage similar to the previous one. In this case, which is only used when we have four PMTs, we will have a logical output signal with the same parameters, height of  $-1.4$  V and width of 20 ns when both detectors have detected events at the same time. The modules used is the same as before.

In Figure 3.18 we have shown some of the different situations that we can have with the previous two steps. There we have four logical signals from four PMTs. The two first signals (channel one and two, yellow and green respectively) come from two PMTs connected to one detector and the other two signals (channels three and four, color orange and violet respectively) come from PMTs connected to another detector.

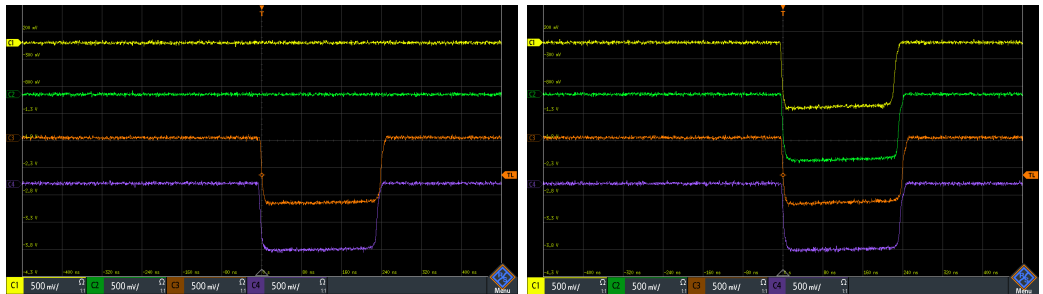
- (a) In Figure 3.18a we can see that only one PMT (channel two) has detected an event. As the second PMT connected to the same detector (channel one) did not detect this event. It indicates that the detected photons did not come from the scintillator. In this case, the time windows (output from coincidence module, stage 1) will not be opened and this event will not be saved.
- (b) In Figures 3.18b and 3.18c we can see that two PMT signals connected to the same detector have detected an event but the others have not. It means that it is an event that has only been detected by one detector. If we are using the second stage of time coincidence, the time window will not open to

save this event.

- (c) In Figure 3.18d we can see that, in this case, all signals have detected the event. It means that it is an event that has been detected for both detectors. In this case, a time window will be created to save this event.



(a) Event detected in only one PMT. (b) Event detected in two PMTs, one detector.



(c) Event detected in two PMTs, other de-(d) Event detected in all PMTs, both detector.

**Figura 3.18** – Different situation that can happen when we do time coincidences with PMTs.

4. Finally, the logical output signal of the coincidence module, which indicates that all the PMTs used in our study are in temporal coincidence, is introduced in the "Gate and Delay Generator", model 416A of the company ORTEC [101]. With this NIM module we obtain a positive logical signal, shown in Figure 3.19, orange color, with a height of 8 V and width of 2  $\mu$ s.

At the end, we have two different signals, shown in Figure 3.19, which will be introduced in the MCA 8000D, Pocket MCA from AMPTEK company [102] to be saved. On the one hand we have an analog signal (output from the amplifier module) that has information about the event that has been detected (its energy, detection time, etc.) and this is the signal whose information we will save for analyzing. On the other hand we have a logic signal (output from the Gate and Delay Generator module) that indicates when we have to save the amplified signal, that is, when all our PMTs used in our experiment have detected an event at the same time.



**Figura 3.19** – Signal amplificated and logical gate (input signals of MCA).

The information that will be saved and histogrammed in the MCA is the weight of the signal, which is proportional to the energy of the detected event, explained in the appendix B.

## Electronical system for SiPMs

Before talking about the electronic system that is used for reading SiPM, we have to keep in mind that we are using SiPM arrays in TRITIUM detector. The electronic system used to process and analyze these output signals is PETSYS [103], which is a commercial system prepared to work with SiPM matrices from Hamamatsu, which is the SiPM company chosen for us.

Petsys system, Figure 3.20, is a complete acquisition and digitization system that is capable of working with up to 1024 SiPM arranged in matrices of up to 64 SiPM per matrix. This capacity is necessary because, as we will see in chapter 5, TRITIUM monitor will use dozens of SiPM matrices with 16 channels (SiPMs) per matrix.

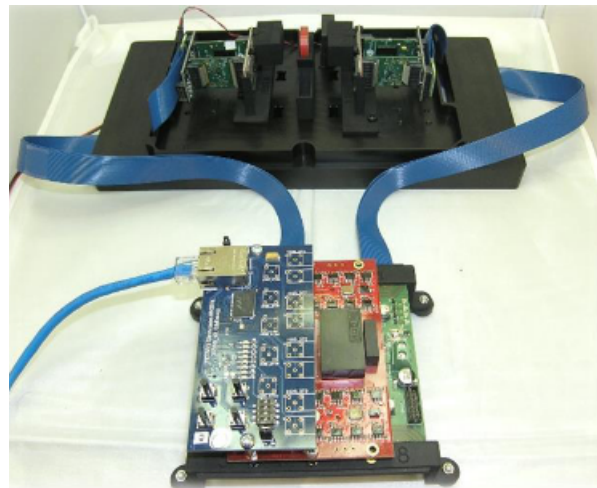


**Figura 3.20** – Different parts of PETSYS system. [103]

Taking into account the current detection limits imposed, this capacity should be enough for TRITIUM detector but, as we will see in chapter 5, TRITIUM is a modular detector. If we need to overcome its limits reached (improve its sensitivity or reduce their background even more) we will need to increase this capacity. We need an electronic system that is

able to increase its capacity in a modular way and PETSYS meets this requirement. It has the Clock and Trigger module with which we have the possibility of connecting up to sixteen different PETSYS basic boards in parallel with which we could read up to 16384 SiPM<sup>15</sup>.

PETSYS is based on C++ and Python scripts that are prepared for the main tasks required for our experiment, such as time coincidence options between SiPM (or even SiPM matrices) or energy discrimination. In addition, PETSYS is open source, so if it is necessary, we have the option to modify the scripts for developing interesting functions. The way the signals will be processed and analyzed for PETSYS will be exactly the same as those shown in Figure 3.17

This system has a time resolution of 250 ps which is one of the best time resolutions of commercial systems available today and its price is around 10€/ channel, which is very cheap in comparison with current similar electronic systems.

As we will see in section 4.3, the temperature of each SiPM matrix is an important parameter to take into account. The PETSYS system has the ability to monitor the temperature of both, the SiPM matrices and ASICS that are used to control them during the measurements.

Although PETSYS is the system used to work with SiPM matrices in the TRITIUM detector, it does not allow characterizing the SiPMs, which is an important task to understand the results of our detector.

In order to do so, we have designed, developed and built an electronic system with which we can read up to eight different SiPMs. With this system we can also monitor the temperature of the SiPMs used.

This system is based on three different PCBs<sup>16</sup>, which are shown

---

<sup>15</sup> $1024 \cdot 16 = 16384$

<sup>16</sup>PCB, Printed Circuit Board

in Figure 3.21 and whose electronical schemes are shown in the appendix C:

1. The first PCB, shown in Figure 3.21a, is used to organize the SiPMs and sensor temperature in this system. This PCB has the ability to place up to 8 different SiPMs and a temperature sensor and arrange these signals on two HDMI connections.

This PCB will be inside a special black box, from "" company, that has a high degree of light tightness. This black box has a small hole, whose diameter is 1 mm, prepared to introduce an optical fiber<sup>17</sup> with which we will illuminate the SiPM with a incoherent light source. The light source used is a LED, model 430L from Thorlabs company [105], whose emission spectrum is shown in Figure 3.21d, which has been experimentaly measured using a spectrometer and fitted to a Gaussian function. We can see that the emission peak of this LED is produced at 436.3 with a FWHM<sup>18</sup> of 19.1 nm. With this LED we intend to simulate the light emission of the fibers used in the TRITIUM experiment to calibrate the SiPMs at the working wavelength.

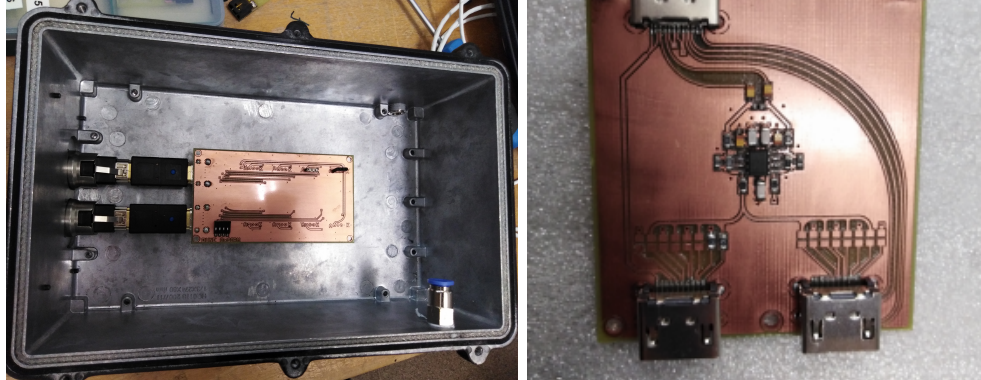
2. The second PCB, shown in Figure 3.21b, is used to sum the different signals from the SiPMs used in the first PCB and amplify the output signal by a factor G. This PCB uses a differential amplification with which we achieve to reduce the electronic noise of the system.
3. The third PCB, shown in Figure 3.21c, is used to arrange all the different input and output signals of this system in an HDMI connection with which we connect to the second PCB. The objective of this PCB is to avoid the introduction of electrical noise by crosstalk between different signals.

---

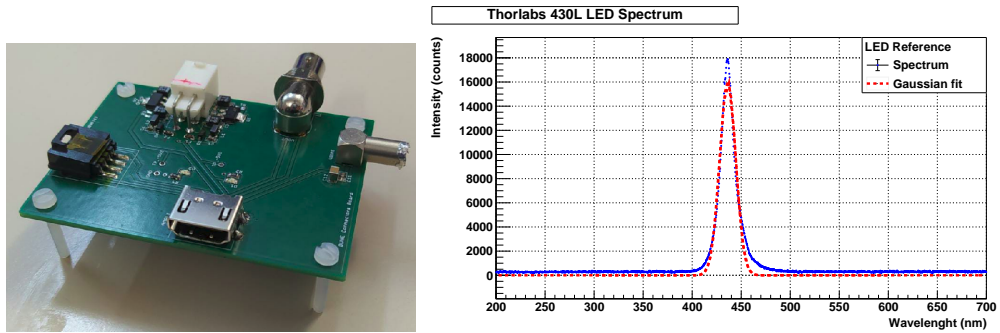
<sup>17</sup>The optical fiber used is BCF-98 from Saint-Gobain company [104]

<sup>18</sup>The FWHM parameter, Full Width at Half Maximum, of a Gaussian fit can be calculated from its sigma using the equation:  $\text{FWHM} = 2.35 \cdot \sigma$

The input signals of this system are the supply voltage of the SiPMs and the supply voltage of the PCBs ( $\pm 6$  V) and the output signals of this system are the temperature sensor signal and the summed signal of all SiPMs.



(a) PCB 1 used to arrange 8 SiPMs and black box.  
(b) PCB 2 used to sum and amplify the output signals of SiPMs



(c) PCB 3 used to arrange the different signals of the system.

(d) Emission spectrum of the LED.

**Figura 3.21** – Three PCBs used for the SiPM characterization and LED emission spectrum.

## 3.3 Ultrapure Water System

### 3.3.1 Introduction to the Ultrapure Water System

The aim of using an ultrapure water system is to condition the sample before the measurement. It is important for two reasons:

- On the one hand, it is important because, as we saw in section 1.2, the mean free path of tritium electrons in water (our case) is around  $5 \mu\text{m}$  and even less for solid materials like organic material.

For detecting this tritium decay, we need that the electron of its decay reaches the fiber, so we must keep our detector clean. If the analyzed water sample contains particles that can be deposited on the fibers of our detector, it can form a layer of matter, which prevents the tritium electrons from reaching the fibers, reducing the tritium detection efficiency until it becomes impossible to measure tritium.

- On the other hand, we have to keep in mind that, as we will see in chapter 5, the tritium monitor does not have any spectrometric capabilities that can be used to distinguish other radioactive elements from tritium. That means that, all the radioactive element included in the analyzed water sample will be computed as a tritium event.

With this system we can remove all particles up to a diameter of  $1 \mu\text{m}$  and organic matter, which means that we remove all particles and molecules other than water. Since tritium is the only radioactive element that can be practically equal to water (when it is in the HTO form, the majority form in which tritium are present in the water sample), with this process we remove all particles radioactive elements other than tritium and the amount of tritium present in the sample is not affected

In summary, with the ultrapure water system we get to keep our detector clean, ensuring the stability of its detection efficiency and we eliminate all radioactive particles other than tritium, maintaining the activity of the tritium in the sample, so we do not need any spectroscopic capabilities in our detector to distinguish radioactive elements. Both reasons has been tested with experimental measurements that will be shown in the chapter 4.4.

### 3.3.2 Set Up of Ultrapure Water System

The main objectives of this water treatment device are:

- Obtaining a high degree of purification in the processed water sample, reducing its conductivity by approximately two orders of magnitude (from  $1000 \mu\text{S}/\text{cm}$  up to  $10 \mu\text{S}/\text{cm}$ )
- Designing of a device with low maintenance (low cost and low man-power)
- Installation of a remote control devices such as probes and valves and development of a software to management it.

For this, the LARUEX laboratory in Extremadura, one of the six collaborators of the TRITIUM experiment, has designed, developed and built an ultrapure water system, whose scheme is shown in Figure 3.22.

This system has been installed in the Arrocampo dam and consists of four different consecutive stages:

- First, the raw water from the Tagus River is introduced into two different filters, the first formed by Silex-Anthracite and the second

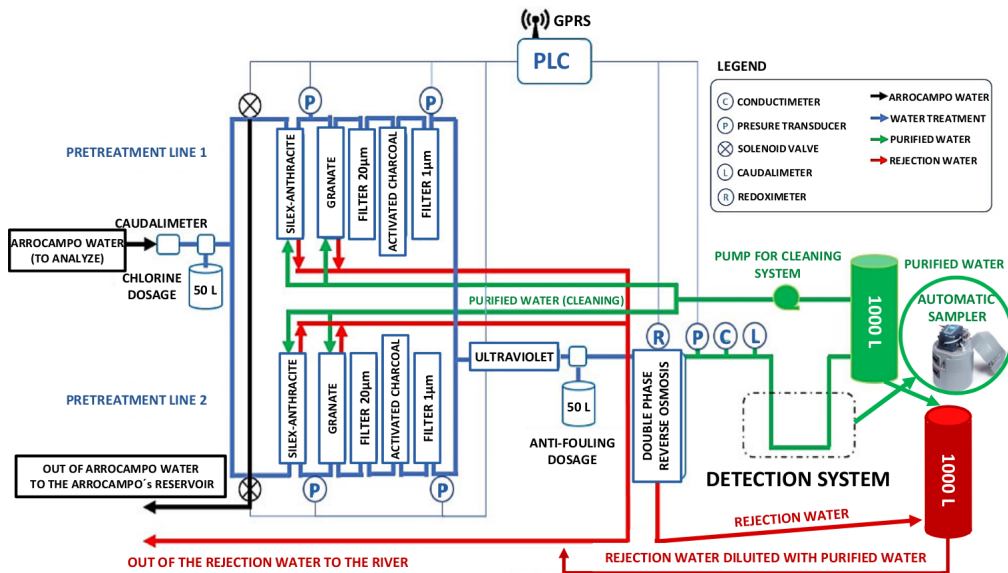


**Figura 3.22** – Scheme of water purification system.

by granate, with which we make a gross filtering (the largest particles are eliminated). There are two parallel lines that are capable of self-cleaning by injecting ultrapure water in the opposite direction.

- Next, this water sample is introduced into a  $20 \mu\text{m}$  filter (Formed by a synthetic mesh) and activated charcoal filters (one per line in both) that form the fine filtration stage. With the  $20 \mu\text{m}$  filter we can filter particles with diameters of up to  $20\mu\text{m}$  and, with the activated charcoal filter, we remove the chlorine and iron particles from the sample.
- Then, this water sample is introduced into the super-fine filtering consisting of a  $1 \mu\text{m}$  filter, formed of a dense polypropylene mesh, (one per line), and UV lamps. With the first we remove all the particles up to diameters of  $1 \mu\text{m}$  and, with the second, we remove the organic matter present in the purified water sample.
- Finally, this water sample is introduced in the last stage, double-

phase reverse osmosis, thereby reducing the conductivity of the water to values of  $5 \mu\text{S}/\text{cm}$ . We verified that we achieve a conductivity of  $10 \mu\text{S}/\text{cm}$  with only one module reverse osmosis and this is enough for the needed conditions of tritium detector. Therefore, we use just one module of reverse osmosis for 24 h and the other for another 24 h, thereby reducing the power consumption of the system.

At the end of this system, each water sample is divided into two different outlet samples. The pure water sample, which is the ultrapure water that will be injected into tritium detector, and the rejection water, whose turbidity is even greater than the water sample before treatment because it contains all the particles that have been extracted from the ultrapure water sample.

With this ultrapure water system we can process up to  $0.850 \text{ m}^3/\text{h}$  with a single line operating or  $1.480 \text{ m}^3/\text{h}$  with both, greatly overestimating the requirements of the tritium detector.

The software used for remote controlling the ultrapure water system is Siemens PLC, with which we receive information such as the state of the valves, the pressure probes or water production in real time.

Several photos of this system are shown in the appendix D.

## 3.4 Background Rejection System of TRITIUM Monitor

The objective of this section is to reduce the radioactive background that affects the TRITIUM detector. It is important because we are following the ALARA principle for the tritium activity measurement, that is, to measure tritium activity "as low as reasonably achievable".

We have to take into account that the low limit reached in the tritium activity measured with our detector will be limited due to the uncertainty in the activity of the radioactive background measured since we cannot measure tritium activities lower than this uncertainty. Therefore, if we want to measure tritium activities as low as possible, we must reduce this background uncertainty as much as possible.

The total uncertainty of the measurement is a quadratic sum of all the different uncertainties present in this measurement, which is the statistical uncertainty,  $\sigma_{st}$ , (due to the statistical nature of the radioactivity process), the systematic uncertainty,  $\sigma_{si}$ , (due to the manufacture of the detectors), etc (equation 3.10).

With the background rejection system of TRITIUM monitor we try to minimize the statistical component. Because of the Poissonian nature of the process, the statistical component of the uncertainty corresponds to the square root of the measured activity,  $A_m$ , equation 3.10, so, if we want to reduce this component, we must minimize the radiological background that affects our detector as much as possible.

$$\sigma_T^2 = \sigma_{st}^2 + \sigma_{si}^2 + \dots; \quad \sigma_{st;bac} = \sqrt{A_{m;bac}} \quad (3.10)$$

The background that affects the tritium detector is due to natu-

ral radioactivity, which is present in all parts of the earth and it has two main origins. On the one hand, it can come from radioactive elements of the natural radioactive series, shown in Table 3.4, which are the primordial radioactive elements, those that are present since the formation of the earth. On the other hand, it can come from natural radiation received from extraterrestrial sources, called cosmic radiation, composed of high-energy particles, mainly protons and  $\alpha$ , which, when they interact with the particles in the Earth's atmosphere, generate a shower of muons, photons and neutrons mainly.

Mass Num.	Series	Prim. el.	Half life (y)	Final isotope
4n	Thorium	$^{232}\text{Th}$	$1.41 \cdot 10^{10}$	$^{208}\text{Pb}$
4n+1	Neptunium	$^{237}\text{Np}$	$2.14 \cdot 10^6$	$^{209}\text{Pb}$
4n+2	Uranium-Radium	$^{238}\text{U}$	$4.51 \cdot 10^9$	$^{206}\text{Pb}$
4n+3	Uranium-Actinium	$^{235}\text{U}$	$7.18 \cdot 10^8$	$^{204}\text{Pb}$

Table 3.4: Classification of natural radioactive series [106][107].

Natural radioactivity depends on the altitude and latitude at which we are on Earth because the volume of the Earth's atmosphere, with which cosmic rays interact, is different. For the same reason, it also depends on the height at which we are working, at sea level in our case, and, due to the relative position of the earth in the universe, it also depend on the solar activity cycle in which we are when we measure. The spatial distribution of cosmic rays, mainly muons, follows a  $\cos^2(\theta)$  distribution with the zenith angle.

We will divide this natural radioactivity into two parts and we will use a different technique to prevent these events from affecting the tritium measurement:

- On the one hand, we have weak radiation, which is any radiation whose energy emission is below 200 MeV/nucleon. To avoid that these events

affect the tritium measurement, we will use a lead shield, explained in section 3.4.1, with which we stop this radiation before it reaches the tritium detector.

- On the other hand, we have the hard radiation, that is, any radiation whose energy emission is greater than 200 MeV/nucleon (mainly cosmic radiation). We have to keep in mind that it is much more difficult to stop hard radiation than weak radiation, so instead of stopping this radiation, what we will do is to build an cosmic veto, which are explained in section 3.4.2, with which we only detect a hard cosmic event and it will be used in anti-coincidence with the TRITIUM detector, that is, we will save the measured tritium event just when we don't measure any hard cosmic event in time coincidence.

### 3.4.1 Passive Shield (Lead)

To stop the weak radiation we use the so-called passive veto, which consists of a lead shielding inside which we will place the TRITIUM detector. This lead shielding is used to stop external particles before they reach the tritium detector, affecting the tritium measurement. It will work for particle energies below 200 MeV/nucleon, which is mainly the earth's natural radioactivity and the weak component of cosmic radiation.

This lead shielding consists of 158 lead bricks with ultra-low intrinsic radioactivity, whose thickness are 25 mm. They are shaped like a chevron, shown in Figure 3.23a, specially designed for a perfect fit and easy assembly. As can be seen in Figures 3.23b and 3.23c, these lead bricks are arranged in two layers leaving a total thickness of the lead shielding walls of 50 mm and the space between the lead bricks in the inner layer is overlaid with a lead brick of the outer layer to avoid possible entry of radiation.

Mechanical engineering department of CENBG has designed a spe-

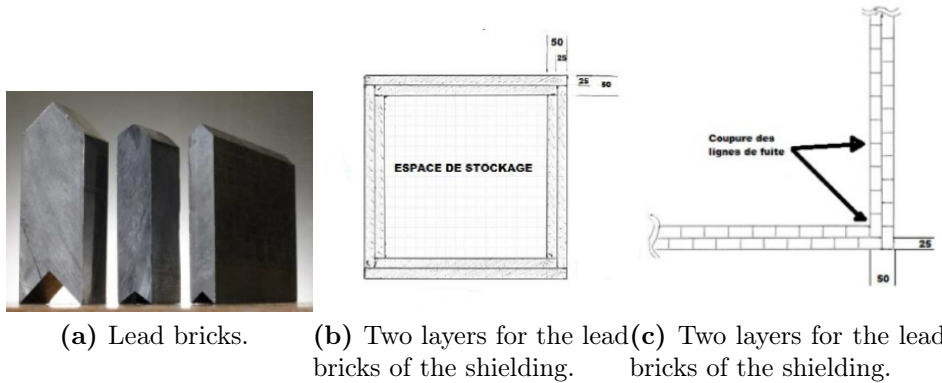


**Figura 3.23** – Lead Bricks and their arrangement in the lead shielding.

cial aluminum structure, shown in Figure 3.24, to support the total weight of the lead bricks, 2.4 tons.

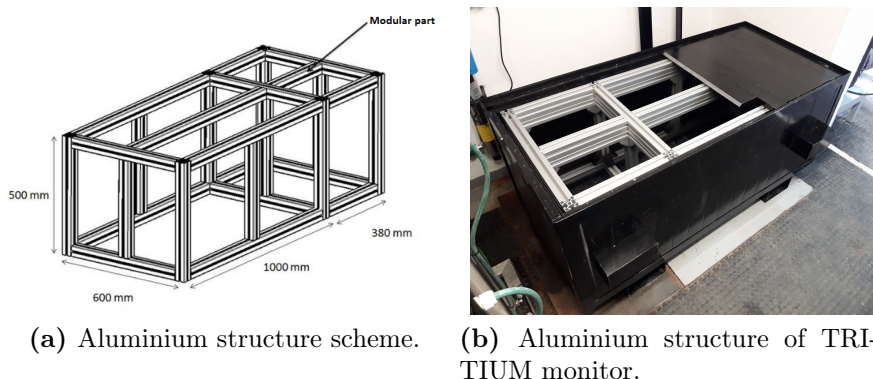


**Figura 3.24** – Lead Bricks and their arrangement in the lead shielding.

The internal space of this lead shielding is arranged in two parts, shown in Figure 3.23. The one, larger, has an internal dimensions of 90.5 cm long, 41 cm deep, and 51 cm high and it will be used to place the TRITIUM detector. The other, smaller, has an internal dimensions of 33 cm long, 41 cm deep, and 51 cm high and it will serve to place the electronic system necessary to collect and store data. The external dimensions of this lead

shielding are 148 cm long, 60 cm deep and 70 cm high and a weight of 2.5 tons.

### 3.4.2 Active Shield (Cosmic Veto)

For this section we have to take into account that the mean free path of particles is proportional to their energy. Therefore, we would need too thick walls to build a lead shield that would be able to stop hard radiation, mainly cosmic radiation. Instead of trying to stop it, we have used the so-called cosmic vetos.

The cosmic veto consists of several complementary detectors, two complementary detectors for each cosmic veto in our case, with which the hard cosmic events that affect the tritium measurement will be detected and subtracted from the tritium measurement.

As you can see in Figure 3.25, the way we have done it is to place two complementary detectors, one above the TRITIUM detector and the other below it. The distance between both vetos is set by the TRITIUM prototype, which has to be placed between both and it is 34.2 cm for our latest prototype.

We must keep in mind that we only want to eliminate the hard cosmic events that affect the tritium measurement. For that we must take into account that this cosmic veto must be placed within the lead shielding. This is because, in this case, the weak radiation, which can contribute as a false hard comic events, has been removed.

Each cosmic detector will have two photosensors, four photosensors in each cosmic veto. The most likely hard cosmic events that can affect the tritium measurement will pass through both cosmic detectors at the same time. To eliminate only them, the first thing we will do is detect only these

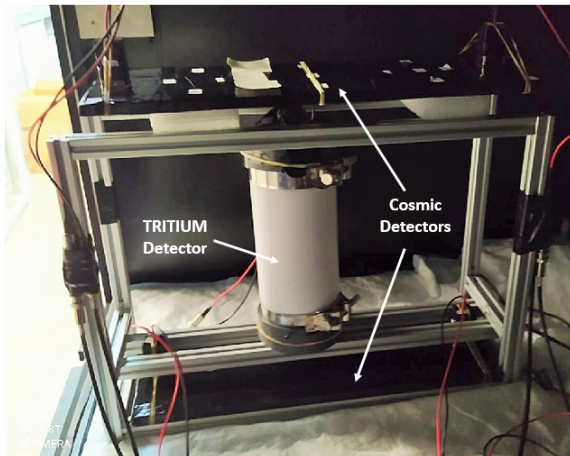


**Figura 3.25** – Cosmic veto and Tritium-IFIC 2 prototype in an aluminum mechanical structure developed by IFIC's mechanical engineering department.

hard cosmic events, which is achieved by reading both cosmic detectors in coincidence with the electron configuration shown in Figure 3.17b and then we will read the TRITIUM detector in anti-coincidence with the cosmic veto, that is, store the tritium measurement only when we don't detect any hard cosmic event in the cosmic veto in time coincidence.

In this case, if we have detect a hard cosmic event (time coincidence event in both cosmic detectors), we can be quite sure that it will cross through the tritium detector and, therefore, it will affect to their measurement, as you can see in Figure 3.26a.

There is a possibility that this hard cosmic event detected in the cosmic veto comes from two different hard cosmic events (one detected in each cosmic detector as shown in Figure 3.26b but it is practically negligible).

The expected hard cosmic rate at sea level for muons, which is the main contributor of cosmic radiation at this height, is  $70 \text{ m}^{-2}\text{s}^{-1}\text{sr}^{-1}$  [108][109], that is, approximately,  $10^{-2} \text{ cm}^{-2}\text{s}^{-1}\text{sr}^{-1}$ , as you can see in their cosmic rate plot, shown in Figure 3.26c. If we take into account that we are

doing time coincidences with signals whose width is of the order of 10 ns we can see that the probability of obtaining two different hard cosmic events in temporal coincidence is less than  $10^{-9}$  which is practically insignificant so they are not worth considering.

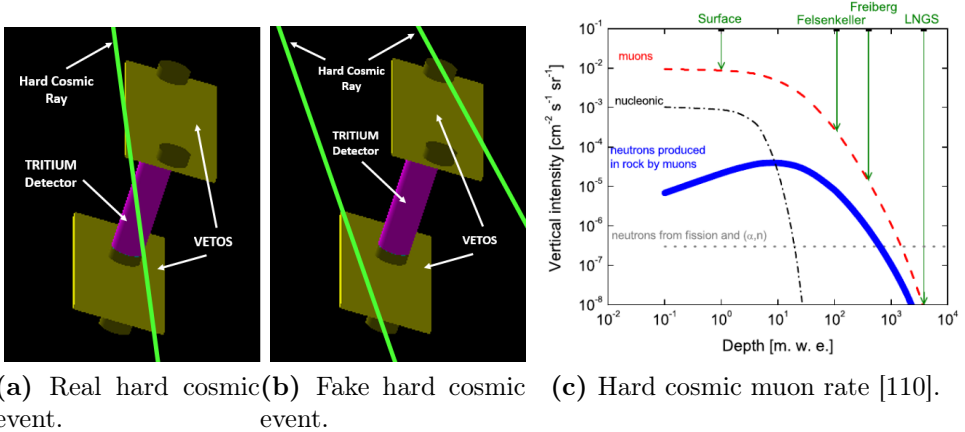


**Figura 3.26** – Hard cosmic events detected with the cosmic veto of TRITIUM:  
a) Affecting to the tritium measurement, b) Does not affecting to the tritium measurement. c) Hard cosmic muon rate.

Finally, these individual cosmic detectors, on which the cosmic veto is based, consist of a plastic scintillator block from Epic-Crystal [111], whose properties and energy emission spectrum are shown in Table 3.5 and Figure 3.27 respectively.

The dimensions used are 45 cm long, 17 cm deep and 1 cm of thickness and they are covered by three layers, teflon, aluminum and black tape, shown in Figure 3.28, which is used, on the one hand, to prevent external photons from reaching the scintillator plastic, giving false hard cosmic events and, on the other hand, to prevent the photons generated by the scintillator plastic from escaping before reaching the photosensor, losing real hard cosmic events.

This coating has two  $2.5 \cdot 2.5$  cm<sup>2</sup> windows where we can place

Base material	Polystyrene
Growth method	Polymeric
Density (g/cm <sup>3</sup> )	1.05
Refractive index	1.58
Soften temperature (°)	75-80
Light output (Anthracene)	50-60%
H/C ratio	1.1
Emission peak (nm)	415 (Blue)
Decay Time, (ns)	2.4
Hygroscopic	No

Table 3.5: Properties of plastic scintillator blocks from Epic-Crystals. [111]

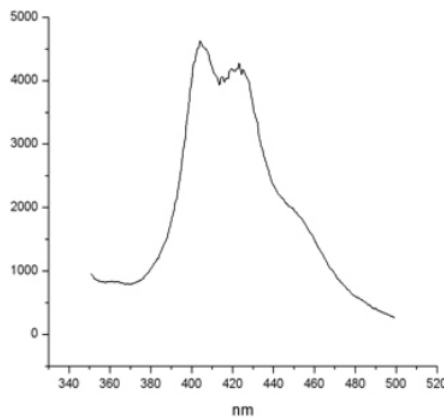


**Figura 3.27** – Emission energy spectrum of the plastic scintillation used for the cosmic vetos. [111]



(a) Scintillator with- (b) Teflon coating. (c) Aluminium coat-(d) Black tape coating.  
out coating. ing.

**Figura 3.28** – Different layers used to cover of the cosmic veto.

both photosensors to read the photons produced by the plastic scintillator.

Now, we can calculate the expected hard cosmic rate for our specifically cosmic vetos. As we have seen before, the expected hard cosmic rate at sea level is  $10^{-2} \text{ cm}^{-2}\text{s}^{-1}\text{sr}^{-1}$ . If we take into account that, on the one hand, the solid angle of our detectors is  $\omega = 0.5434$ , which has been calculated by integrating above the area of the TRITIUM cosmic veto, and the area of its cosmic veto is  $45 \text{ cm} \cdot 17 \text{ cm} = 765 \text{ cm}^2$ , the expected hard cosmic rate on our cosmic vetos should be 2,909 event/s.

# Chapter 4

## Research & Development on Detector Design and Components

### 4.1 Introduction

This chapter shows the characterization of each individual part of the TRITIUM monitor, which includes scintillating fibers, SiPMs (at the individual SiPM level and at the matrix level), the ultrapure water system and the background rejection system, consisting of the lead shielding and the active veto.

This characterization is one of the most important things to do because it will help us to understand their behaviour and the results obtained with the complete monitor. Furthermore, we have made some developments to improve interesting parameters of the TRITIUM monitor components to enhance the monitor's capabilities of tritium detection.

All these studies have been carried out inside a special light-tight box, called black box, to ensure that the photons we are detecting come

from the photon sources used, whether they are emitted by LEDs or by scintillators. In addition, because of the reason that we cannot do an accurate energy calibration when using plastic scintillators, we will show some of their energy spectrums in units of channels (units of ADC), which are linearly proportional to the units of energy.

## 4.2 Characterization and R&D on Scintillating Fibers

### Introduction

In this section we will make experimental measurements of the scintillating fiber parameters that most affect the tritium detection, such as its collection efficiency or their uncertainty in its conditioning process.

We have to take into account that we are working with thousands of scintillating fibers that need to be prepared and conditioned prior to use in fiber studies or inside of TRITIUM monitor. Therefore, as we will see in this section, we had to develop machines that are able to automatically prepare so many fibers at the same time.

### Scintillating Fiber Conditioning Process.

First thing we had to do in TRITIUM experiment was to choose the optimal fiber length at which the signal from the tritium events is optimized. To make this decision we have to take into account that, on the one hand, long fibers are interesting because the efficiency of our detector is proportional to the active area, which is proportional to the fiber length but, on the other hand, in long fibers, scintillation photons will need to be reflected in the fiber walls more times to be driven to its ends, where it will be detected by photosensors and this is a problem because we lose photons in each reflection, deteriorating the detector signal.

Several simulations were performed using Geant4 [112], a particle and nuclear physics simulation package based on C++, to quantify, between other things, the importance of this effect and to allow us to choose the optimal fiber length. The results of this simulations will be shown in section

7.4, where they will be discussed. In these simulations it has been seen that it is preferable to work with short fiber (Figure ??). The fiber length, which has been chosen for the tritium prototypes developed in Valencia, is 20 cm and the fiber length used in each study will be named in the appropriate section, but it will be close to this value.

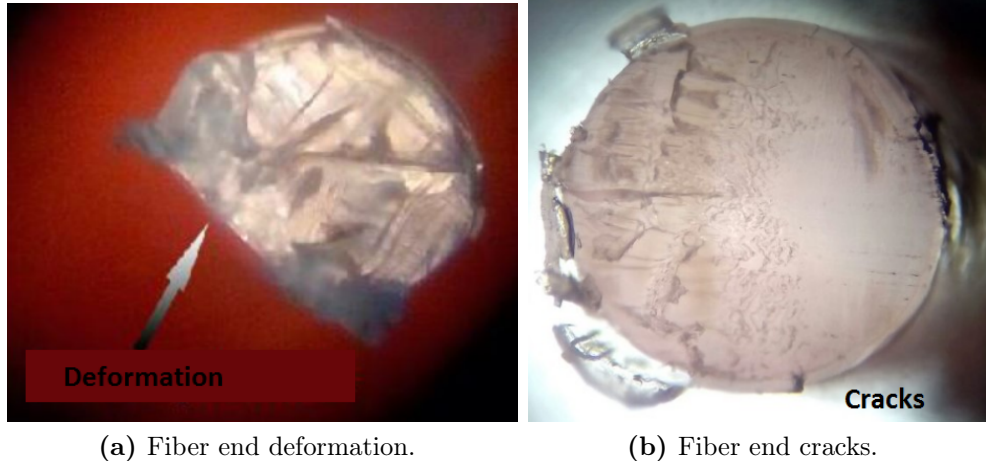
Saint-Gobain's commercial fibers are 1 meter long, so first thing we had to do was cut the scintillation fibers before using it. It is very important to introduce strict requirements on the cutting quality of the fiber ends since it will greatly affect the transmission of photons and, thus, the efficiency of TRITIUM monitor. This cut must be perpendicular to the fiber and very low uncertainty in the length of the fiber, both requirements are mandatory to achieve a good coupling with the surface of the photosensor. It is also important that its final state must be as clean as possible, that is, without cracks or deformations because it will contribute to internal reflections, losing photons and, thus, reducing the tritium signal.

Cutting the end faces of polymer fibers is one of current challenges. There are many different techniques such as milling, laser cutting, focused-ion-beam, blade cutting, etc. Due to its simplicity, we have focused on blade cleaving.

Many commercial devices based on blade cleaving, such as the one provided by thorlabs with a diamond tipped blade [113] or others similar to the guillotine designed for industrial fiber optics [114], were tested in a extensive study done but with unsuccessful results [79]. As can be seen in Figures 4.1, it presents deformations, cracks or imperfections so the technics considered in this study don't overcome the requirements imposed.

The microscope model PB 4161 from EUROMEX company or the Digital Microscope from Jiusion company, shown in Figures 4.2, were used to check the results in the fiber ends.

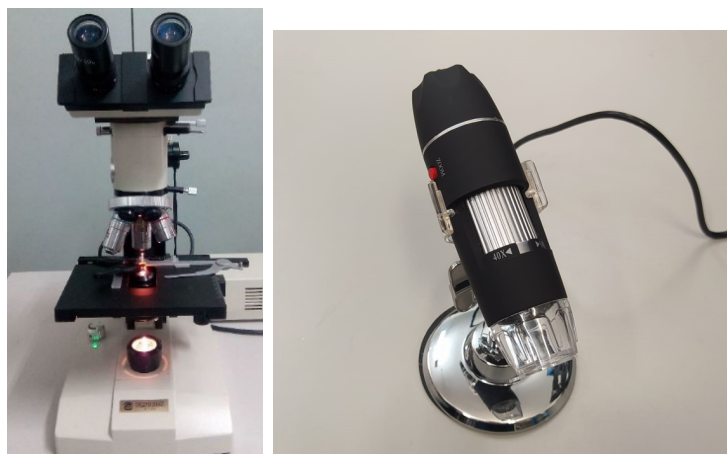
Because commercial devices don't work for our scintillating fibers,



(a) Fiber end deformation.

(b) Fiber end cracks.

**Figura 4.1** – Unsuccessful results of using commercial techniques to cut fibers.

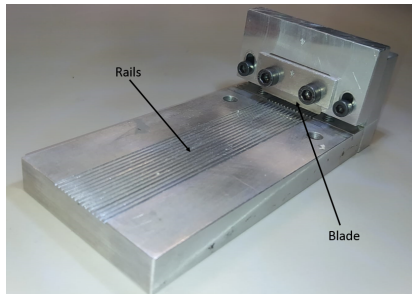


(a) EUROMEX microscope

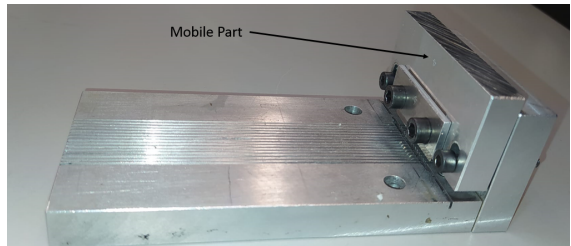
(b) Jiusion microscope

**Figura 4.2** – Microscopes used to check the results.

we had to design, build and test our own cutting device, which is shown in Figure 4.3.



(a) TRITIUM Cutting device



(b) TRITIUM Cutting device



(c) Additional piece of TRITIUM cutting device

**Figura 4.3** – Cutting device developed in the TRITIUM experiment and additional part to make precise measurements of fiber length.

It consists of fourteen rails where the fibers will be fixed and a thin blade, fixed on a mobile piece, perpendicular to the fibers, with which we can be sure of achieving a perpendicular cut, which is one of the requirements imposed.

The blade used is the typical commercial razor blade, whose thickness is 0.1 mm, which is the thickness with which we obtain the best results and it was positioned with a slight inclination, 5°, with respect to the horizontal axis since it has been seen in several studies that this helps to obtain a less aggressive and cleaner cut [115], [116].

Therefore, as can be seen in Figure 4.4a, with this device we obtain fiber ends without breaks or deformation overcoming another imposed

requirement.

Another important parameter that can affect the cutting quality of the fiber ends is the temperature of both, either the fiber or the blade. It has been tested in a study in which both were subjected to different temperatures from room temperature (25 degrees) to 110 degrees [79]. No significant conclusions were obtained in the temperature study, so we work at room temperature to facilitate the cutting technic.

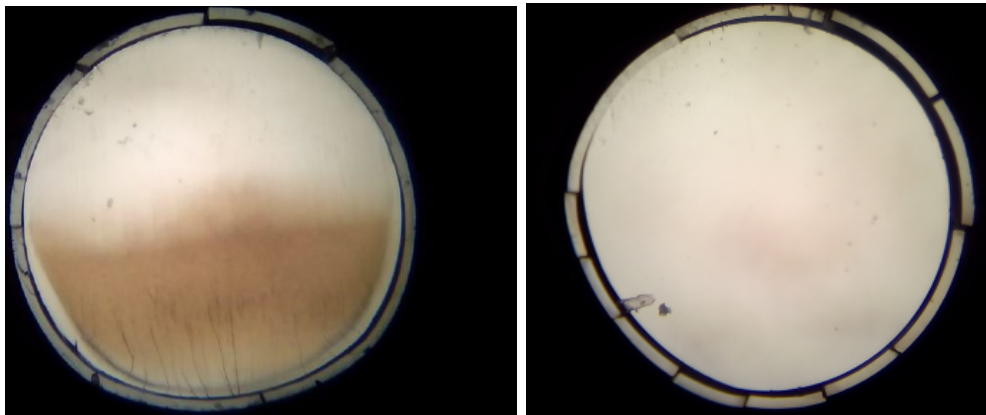
To obtain a low enough length uncertainty, which is the last requirement we must overcome, we designed and built an additional piece, shown in Figure 4.3c, which is used to measure the fiber. With this piece we achieve an uncertainty in the measurement of less than 1 millimeter.

With the designed cutting fiber device we have exceeded all requirements imposed, obtaining a cut fiber end whose quality is high enough to ensure that it will affect the transmission of light as little as possible.

In Figure 4.4a, which shows the fiber end after cutting process with TRITIUM cutting device, you can see a slightly darkened part at the bottom of the fiber, which is an inevitable effect of the cutting process. To repair this imperfection, a polishing process developed by thorlabs is included [113].

This polishing process consists of using five different polishing papers, with a decreasing grain size, whose diameters are  $30 \mu\text{m}$ ,  $20 \mu\text{m}$ ,  $12 \mu\text{m}$ ,  $5 \mu\text{m}$  and  $0.3 \mu\text{m}$  respectively, in which we describe movements in the shape of 8 for two minutes (approximately 120 movements).

The result obtained with this polishing process is shown in Figure 4.4b. In Figure 4.4, the quality of both fiber ends, before and after polishing process, can be compared. There, we can see that the darkened part has completely disappeared.



(a) Fiber end after cutting with Tritium de-(b) Fiber end after cutting and polish-vice. ing.

**Figura 4.4** – Result of the polishing process. a) Fiber end after cutting with TRITIUM devices b) Fiber end after cutting with TRITIUM devices and polishing with Thorlabs technic.

The end of the cut fiber is completely clear after cutting and polishing, without any damage or imperfection, so both tasks, cutting and polishing, will make up the conditioning process developed for each fiber before any study or its introduction into the TRITIUM detector.

### Automatic Polishing Machine for Scintillating Fibers

At this point we have to take into account that, as we will see in sections 5.3.1 and 5.3.2 respectively, we have to use three hundred fifty and eight hundred scintillating fibers for our latest prototypes, Tritium-Aveiro 0 and Tritium-IFIC 2, which means that we will have to prepare tens of thousands of fibers for the TRITIUM monitor<sup>1</sup>, section 5.4 and we will have to condition each scintillating fiber.

---

<sup>1</sup>Our final prototype will be a module of TRITIUM monitor, which will be based on dozens of modules.

While this amount of fibers is not a problem for the cutting process, as it is very fast, the polishing process would be too time consuming because it takes more than ten minutes to polish each fiber.

Therefore, we designed, developed, built and tested an automatic polishing machine for scintillating fibers, shown in Figure 4.5, with which we can polish up to one hundred scintillating fibers at the same time and automatically. Furthermore, if we want to increase its fiber capacity, it is easily scalable.

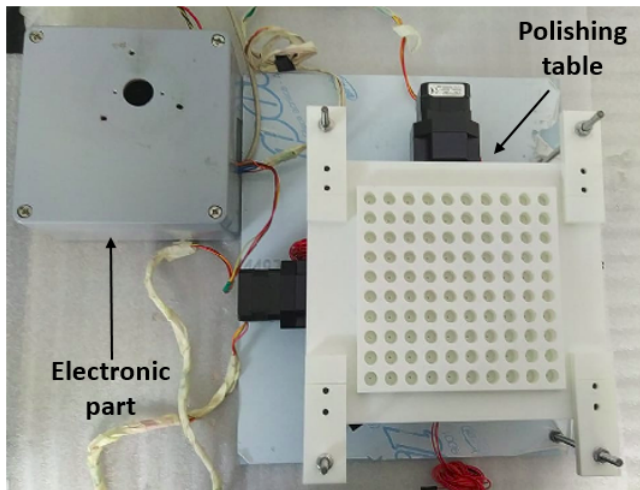


**Figura 4.5** – Polishing machine developed in TRITIUM experiment.

As we can see in Figure 4.5, this automatic polishing machine is based on two parts. On the one hand, the polishing table, where the fibers will be polished and, on the other hand, the electronics used, based on arduino technology, to automatically move the polishing table:

1. The polishing table can be divided in two parts, the immobile part, where the fibers will be fixed, and the mobile part, where the polishing papers will be fixed. We decided to move the polishing papers because they are lighter and mechanically easier than fibers.

The immobile part consists of a piece, shown in Figure 4.6a, which has been designed and built with a 3D printer, fixed to the system with four vertical screws. There are two nuts on each screw that are used to set the height and the inclination of fibers relative to the polishing papers. This piece contains one hundred holes where the fibers will be placed.

Because of the reason that the fibers will press the polishing paper with their own weight, we use a plastic belt and a piece of metal with a weight of around 100 g, shown in Figure 4.6b, to increase its weight (in the same way as in thorlabs polishing process).

The mobile part consists of a flat PMMA plate, whose dimensions are  $18 \cdot 18 \text{ cm}^2$ , on which the polishing paper will be fixed. This part is fixed to two horizontal screws, perpendicular to each other, that are used to move it around the XY plane (horizontal plane). This system is shown in Figure 4.6c.

This system contains multiple switches, each mounted on a piece designed with a 3D printer, shown in Figures 4.6a, 4.6c and 4.6d. As we will see in this section, these switches are used to stop the system if they reach the end of the path and to find the coordinates origin.

2. The electronic part, shown in Figure 4.7, is based on arduino technology and it is used to achieve automatic movement of the polishing paper.

It consists of two stepper motors, model NEMA ST4209S1404-A [117], which are used to control the horizontal screws on which the polishing paper is fixed. These motors are controlled by an arduino UNO [118] that uses a CNC shield [119] in which two different drivers are connected to control these stepper motors, one driver for each stepper motor.

Drivers are controllers that allow you to manage stepper motors in a simple way. Choosing the correct controller for your system is very

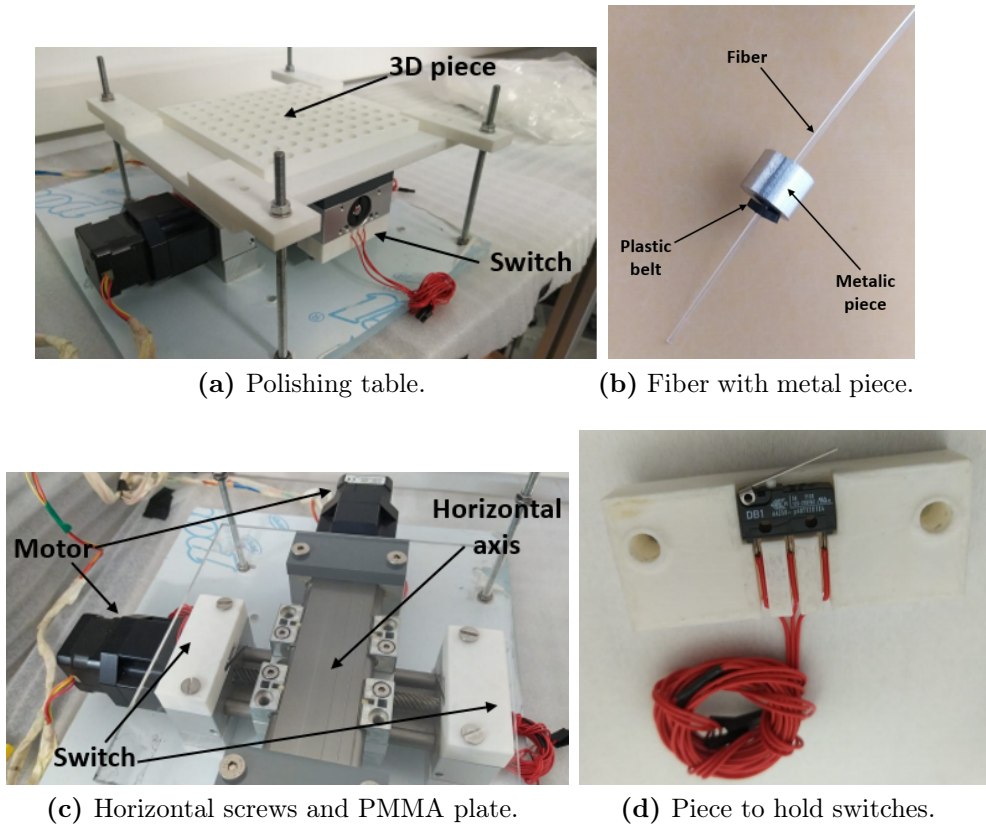


**Figura 4.6** – Polishing table of the polishing machine

important because it can limit the supply power to the motors, causing the motors not to move in the worst case. Instead of using the Pololu A4988 drivers [120], which is one of the most widely used drivers, our first choice was the DRV8825 driver [121] since DRV8825 allows to power the motor with higher voltage and intensities (45 V and 2.5 A) than A4988 (35 V and 2 A). Also, the DRV8825 controller includes a new microstepping mode (1/32) compared to the A4988 (1/16) with which we get more accurate and smooth movements.

Finally these drivers were replaced by the TMC2208 [122]. The main reason for this change was that they are much less noisy since it includes the *StealthChop* function with which the noise is practically eliminated. On top of that, this controller is much more accurate as it has a microstepping mode of 1/256.

The voltage and current used to power the motors are similar to the A4988 (35 V and 2 A) which is sufficient for our system since the used motors are limited to 1.33 A.

The excess current will be transformed into heat that we will have to dissipate from the system since overheating of these drivers can cause loss of steps, producing movements different from those programmed or even destroying the driver. Therefore, a cooling system is needed to ensure the correct operation of the polishing system.

The cooling system, shown in Figure 4.7, is based on a fan and a copper piece<sup>2</sup> in contact with both controllers. It has the possibility to use a PELTIER cell to increase the cooling power of this system. A fan is also included to prevent heat accumulation inside the electronics box.

This polishing machine is controlled by a computer using the Universal G-code Sender software (a graphical interface based on the GRBL package). It has several useful functions such as the "HOME" function with

---

<sup>2</sup>The copper is one of the best thermal conductor at STP

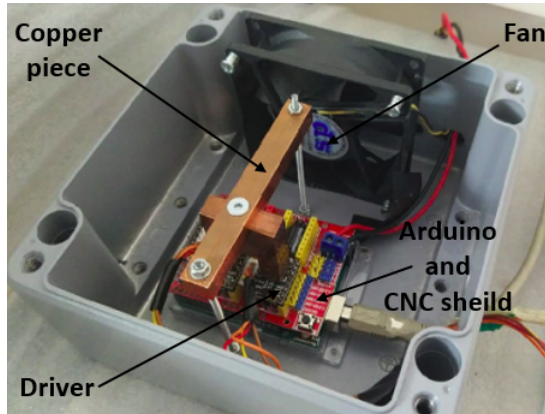


**Figura 4.7** – Electronic system of Polishing machine.

which the system, using the previously installed switches, finds its origin coordinate every time the system is turned on.

It also has the ability to load a file containing the g-code to be executed, which is used for us to program the 120 movements required for each polishing paper.

To test this machine, twenty fibers with a length of 15 cm were cut and arranged in a bundle. They were fixed in a structure shown in Figure 4.8 with two PMTs located at their ends, which were read in time coincidence using the electronic system described in section 3.2.4, Figure 3.17a.

Two different measurements were taken using two different radioactive sources,  $^{60}\text{Co}$ , whose activity was approximately 715 Bq, as a gamma source and  $^{90}\text{Sr}$ , whose activity was approximately 17.8 kBq, as a beta source. After that, the fiber bundle was polished with the polishing machine developed and the test was repeated.

The energy spectrums recorded are shown in Figure 4.9 for each radioactive source, which where placed in the middle of the fiber, that's,

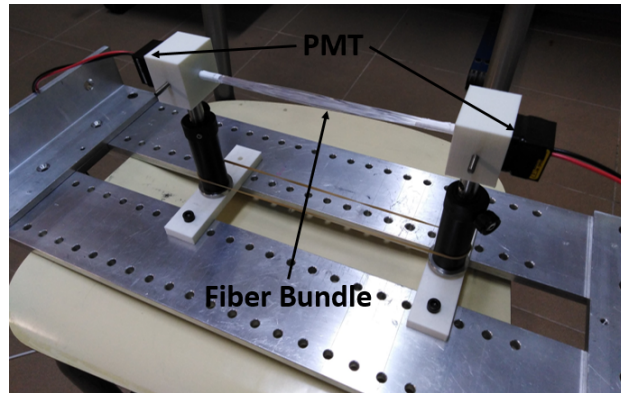


**Figura 4.8** – Set up used to test the effect of the polishing machine.

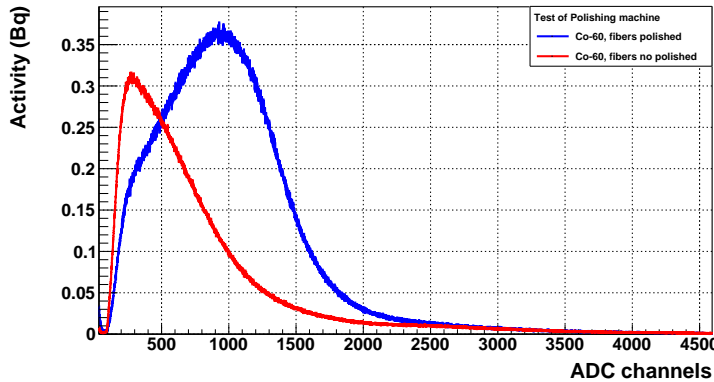
7.5 cm from each PMT.

As can be seen in these figures, both energy spectrums have shifted to the right of the spectrum, which means that the detected events have more energy (more photons per event has reached the PMTs). On top of that, an increase of more than 40% (42% for gamma source and 49% for beta source) has been achieved in the number of counts registered in both cases.

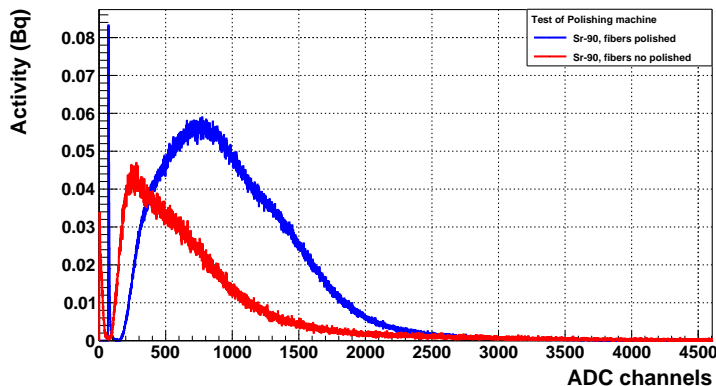
The reason for this is that, with this process, we have improved the photon collection efficiency of the system (mainly because we have improved the interface between fibers and PMTs) which, as we discussed previously, is very important for the reason that we expect to detect few photons in each tritium event.

### Characterization of Scintillating Fibers

This section shows the characterization of no-clad BCF-12 fibers from Saint-Gobain, which are the fibers used in the TRITIUM experiment. These measurements are compared to other measurements that have been made using single clad and multiclad BCF-12 fibers to quantify how the clad affect



(a) Energy spectrum recorded for the Co-60 source.



(b) Energy spectrum recorded for the Sr-90 source.

**Figura 4.9** – Energy spectrums used to test the effect of the Polishing machine

to several parameters of scintillating fibers.

It is an interesting comparison because, although commercial clads cannot be used for the TRITIUM experiment, we can develop our own clad with a low enough thickness. For example, clads with a thickness of the order of tens of nanometers can be achieved by electrodeposition techniques.

As we have seen in section 3.2.2, the difference between these three types of fibers is that no clad fibers only consist of a polystyrene core with

a refractive index of 1.60 whereas, in single clad fibers, the polystyrene core has an acrylic cover (PMMA) with a thickness of 30  $\mu\text{m}$  and a refractive index of 1.49 and, in multiclad fibers, this acrylic cover has another fluor-acrylic cover with a thickness of 10  $\mu\text{m}$  and a refractive index of 1.42.

This characterization has been carried out at the level of a single scintillating fiber and the parameters that have been measured in every type of fiber are the fiber collection efficiency and the uncertainty in the fiber response due to the conditioning process developed in TRITIUM. The reference measure that will be used for that is the number of photons per second that reach the active area of the photosensor.

To measure this parameter we will use a calibrated PMT, model R8520-06SEL, whose quantum efficiency at the working wavelength, 29.76%, has been measured by Hamamatsu. As we have seen in section 3.2.4, to measure this parameter, on the one hand, we need to work without internal gain of the PMT and, for this task, we will use the PCB described in section 3.2.4, Figure 3.16 and, on the other hand, the Keithley 6487 Picoammeter/Voltage Source will be used to measure the output current of the PMTs. The number of photons per second can be known from the Keithley measurement using the equation 3.9 with  $QE = 0.2976$  and  $CE = 1$ . The Figure 4.10 shows a schematic of the set up used for this characterization.

It consists of an optical structure in which a LED and a PMT are fixed to the specific distance between them, established by the user. The LED used is the model LED435-03 from the Roithner LaserTechnik GmbH company [123], whose emission spectrum is shown in Figure 4.11, which has been experimentaly measured using a spectrometer and fitted to a Gaussian function. We can see that the emission peak of this LED is produced at 433.9 nm with a FWHM of 18.4 nm. With this LED we intend to simulate the light emission by the fibers used in the TRITIUM experiment, similar to how we explained in section 3.2.4.

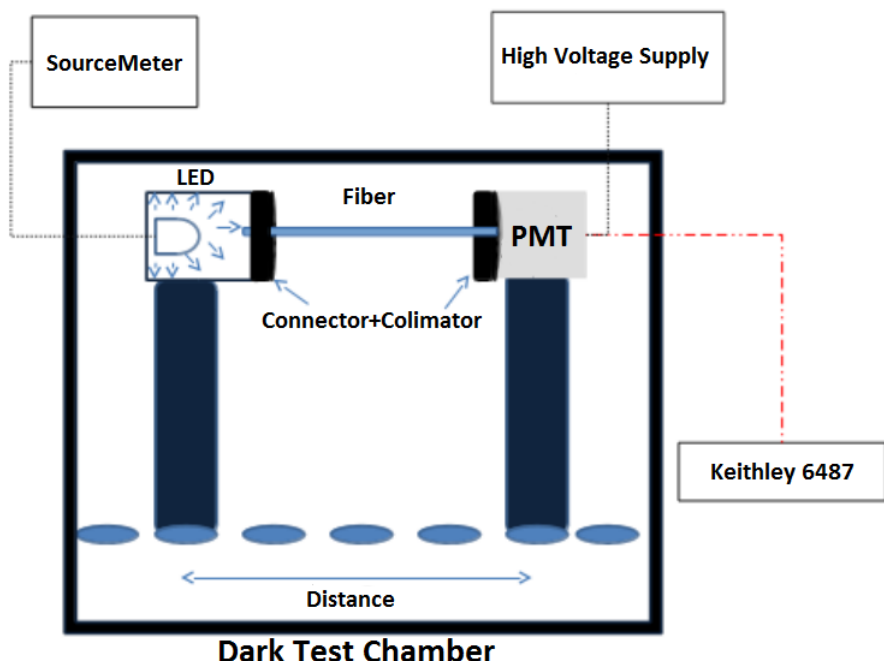


**Figura 4.10** – Set up used for fiber characterization.

The fiber will be fixed between the LED and the PMT, whose distance will be configured based on the length of the fiber, 20 cm for all this study, and optic grease [125] will be used for optimal optical coupling between the fiber and the PMT. Two collimators are used to ensure that the photons detected in the PMT are only those that come from the LED and travel through the fiber and two connectors, type FH-ST<sup>3</sup> from RoHS company [], were placed to the ends of the fiber and used to fix it to the system.

Before we start with the characterization of the fiber we have to perform several tasks to check that our system is fully prepared to measure. On the one hand we have to verify the quality of the tightness to the light of the black box used and, on the other hand, we have to verify the correct

---

<sup>3</sup>FH-ST is a quick assembly connector for 1 mm POF

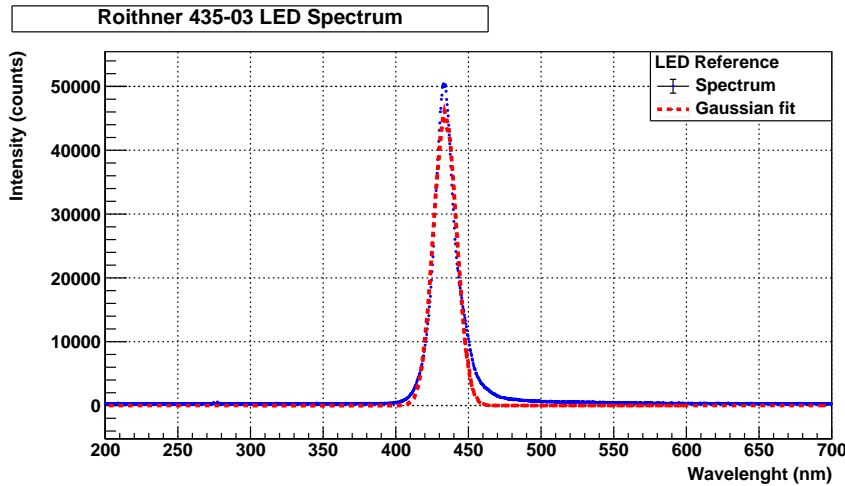


**Figura 4.11** – Emission spectrum measured for the LED model 435-03 from Roithner LaserTechnik GmbH Company.

operation of the PMT for this study, which involves checking the correct operation of the PCB designed to work without internal gain and checking the linearity of the PMT output signal in the study range.

First, the quality of the light tightness of the black box used will be verified. It is important because we are detecting a few hundred photons per nanosecond, so we must check that our background is as small as possible.

This test will be carried out by measuring a no-clad fiber, whose length is 20 cm, in the previous assembly. This measurement was carried out by feeding the LED with four different intensities (0.05 mA, 0.1 mA, 0.15 mA and 0.2 mA) and this measurement will be repeated covering the set up with a special black blanket from Thorlabs [126] with which we can make sure that the amount of photons that reach our system is negligible.

This test was repeated for three different no clad fiber samples and the mean and standard deviation were calculated using the equations 4.1.

$$\bar{x} = \frac{\sum_{i=0}^N x_i}{N}; \quad Std. Des. = \frac{\sqrt{\sum_{i=0}^N (x_i - \bar{x})^2}}{N - 1}; \quad (4.1)$$

The difference between the results obtained in both tests is presented in Figure 4.12.

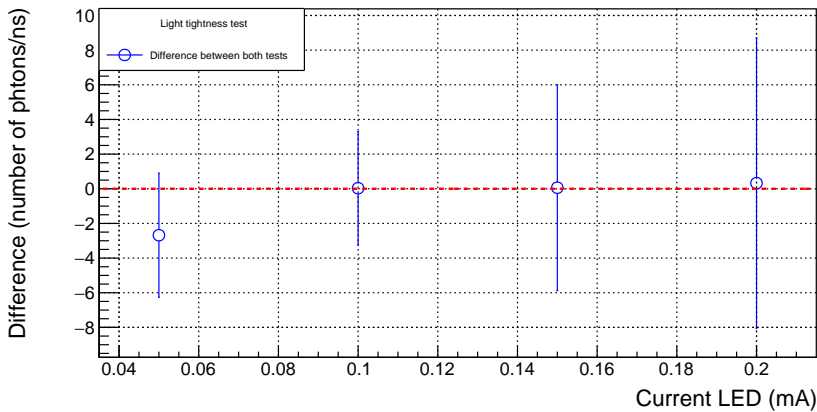


**Figura 4.12** – Difference between the results obtained in both tests carried out to check the light-tight quality of the system.

As can be seen in this figure, there are no statistically relevant differences between both situations, which can be verified with the help of the red auxiliary line that marks 0 (no difference). Therefore, we can be sure that the quality of the light tightness of the black box used is high enough for our tests.

Then the operation of the PCB without the internal gain will be tested. It consists of finding the plateau in which the electron collection efficiency in the first dynode is practically 100%.

This test will consist of, using the setup previously explained with-

out any fiber, feeding the LED at 1 mA intensity. There, the PMT output current was measured for different voltages between 0 and 500 V. The Figure 4.13 show the number of photons detected by the PMT (using a semi logarithmic scale).

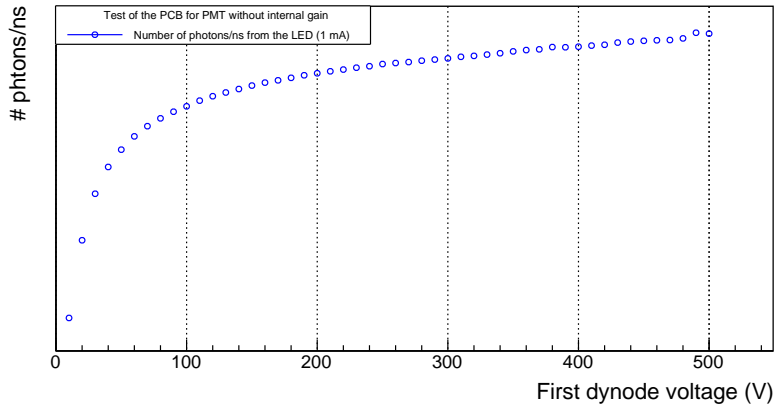


**Figura 4.13** – Response of the PMT based on its high voltage using the PCB with which we get no internal gain from the PMT.

As we can see, this plateau is found at voltages higher than 150 V, where we can appreciate that the PMT output response are stable. This is the interesting range within which we should work. The chosen voltage at which we developed all this study was 250 V.

Finally, the linearity of the PMT will be verified. In this study the LED will be powered with several intensities of up to 10 mA (LED linearity range) to ensure that its emission is not saturated.

This linearity will be tested in two different ranges, one in the range of the number of photons expected in a tritium event that is only a few tens of photons per tritium event (tens of photons per nanosecond), as we have seen in section 3.2.2, and, second, in the range of this study, whose events will have up to two thousand five hundred photons per nanosecond.

To test the linearity of the PMT at the level of tritium events, we will use the set up explained above without any fibers and without the connector that there is in the part of the PMT but keeping the collimators to ensure that the active area of the PMT is the same as the one we use in this study.

To test the linearity of the PMT at a level of more than a thousand photons per nanosecond, we remove the other connector (the one in the LED part) in order to increase the photons emitted by the LED that reach the photosensor and also keeping the collimators.

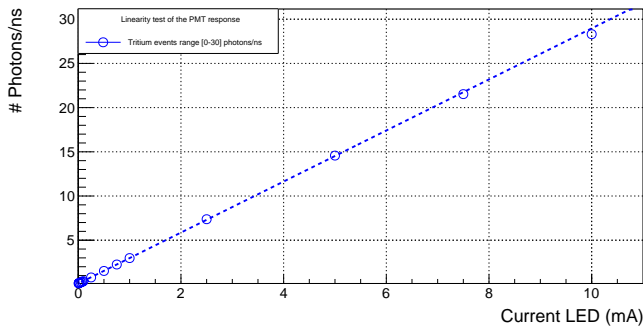
Both results is shown in Figures 4.14, where the uncertainties are included but they are too small to be visible.

As can be seen, the PMT output current is linear in both cases, so the system is ready to start with the characterization of the fibers.

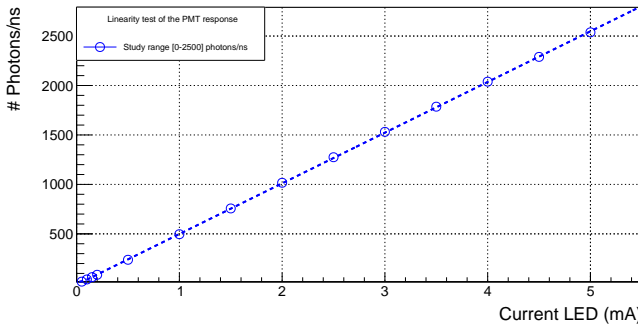
First, the uncertainty of the conditioning process,  $\sigma_{con}$ , was experimentally measured. This uncertainty appears because, as we have seen before, we have to condition each fiber, cutting and polishing it, before using and this is an individual task that can present a small dispersion, affecting the response of each individual fiber. It is an important measurement because this uncertainty will be present in the TRITIUM detector.

To measure it, we have to take into account that there is a bit of freedom in this system due to the position of the connectors which are fixed to the fiber (1 mm or less) which means that there is an additional uncertainty,  $\sigma_{pos}$ , in the measurement. Since both uncertainties are not related, the total measurement uncertainty can be calculated as a square sum, equation 4.2.

$$\sigma_t = \sqrt{\sigma_{pos}^2 + \sigma_{con}^2} \quad (4.2)$$



(a) Verification of linearity in the response of the PMT in the range of tritium events.



(b) Verification of linearity in the response of the PMT in the range of this study ( $0 - 2500$ )  $\gamma/\text{ns}$ .

**Figura 4.14** – Linearity tests of the PMT response

The uncertainty due to the fiber position are always presented in the measurement so, the only way we can measure the uncertainty due to the conditioning process is to quantify the uncertainty in the fiber position and extract it to the total uncertainty, sum of both, using the equation 4.3. To do so we have designed two different experiments, one where only the uncertainty in the fiber position are presented ( $\sigma_t = \sigma_{pos}$ ), and other in which only both uncertainties are involved.

$$\sigma_{con} = \sqrt{\sigma_{tot}^2 - \sigma_{pos}^2} \quad (4.3)$$

The test designed to measure  $\sigma_{pos}$  consisted of prepare one fiber of each type (no clad, single clad and multiclaid) using the conditioning process explained before. Then, fix each fiber in the set up, take a measurement by feeding the LED at an intensity of 0.1 mA and remove this fiber to the set up (and also the connectors). Finally, we repeat these measurements ten times with the same fiber, fixing and removing it every time.

With this test, we will obtain ten different measurements for each fiber type in which, the standard deviation of these measurements is only due to the uncertainty in the position. The results is shown in Table 4.1, whose results has been calculated using the equations 4.1 and 4.4.

$$Rel. Std. Des. = \frac{Std. Des.}{\bar{x}} \quad (4.4)$$

Fiber type	Average ( $\gamma/\text{ns}$ )	Std. Des. ( $\gamma/\text{ns}$ )	Rel. Std. Des. (%)
No Clad	$524.088 \pm 0.010$	17.65	3.37
Single Clad	$1071.696 \pm 0.01$	9.07	0.85
Multiclad	$949.930 \pm 0.026$	9.91	1.04

Table 4.1: Average and standard deviation (due to fiber position in setup) of photons per nanosecond that reach the PMT for 0.1 mA LED intensity.

As we can see, the clad of the fiber reduces the uncertainty due to the position of the fiber, which means that it improves the uniformity of the fiber response. Also, as can be seen from this table, the use of the clad greatly improves the collection efficiency of the fibers since both types of fibers with clad have collected more photons than the fiber without clad. A possible reason of that is because the photons are mainly collected in the core of the fiber and one of the most important things that will affect to

the collection efficiency is the interface created by this core.

This interface can be much more controlled in the case of a single clad or multiclads fibers where it is created between the core and the first clad, than in no clad fibers, where it is created between the core and the environment (air or water in our case), where external conditions, such as the dirt in the room, can affect a lot.

We can also see that the use of a second clad slightly reduce the collection efficiency. A possible reason of that is ...

We can also see that the error of the measurement, provided by the keithley and propagated to the average, is three times smaller than the standard deviation, so we will not take it into account any more.

Now, we do the other experiment in which both uncertainties are involved. It consists of preparing ten different samples of each type of fiber (using the conditioning process) and measuring it under the same conditions as the previous test. This measurement will be done for four different LED emission intensities (0.05, 0.1, 0.15 and 0.2 mA) to reduce possibles mistakes.

The case of no clad fibers is shown in Figure 4.15, where we can see that, indeed, although each fiber shows a very linear trend with the amount of photons that it collects, a dispersion in the fiber response is clearly seen in each figure. Similar results were obtained for single clad and multiclads fibers.

The average of these 10 samples for each type of fibers and its standard deviation are summarized in Tables 4.2, 4.3 and 4.4 and represented in Figure 4.16, where they can be compared.

As it is shown in Figure, they have a very linear trend which confirms the correct behavior of the fibers. We can also see that, similar to

Led Int. (mA)	Average ( $\gamma/\text{ns}$ )	Std. Des. ( $\gamma/\text{ns}$ )	Rel. Std. Des. (%)
0.05	243.46	9.82	4.03
0.1	540.62	33.51	6.20
0.15	902.74	36.83	4.08
0.2	1252.62	50.48	4.03

Table 4.2: Average, standard deviation and relative standard deviation of 10 different samples of no clad fibers.

Led Int. (mA)	Average ( $\gamma/\text{ns}$ )	Std. Des. ( $\gamma/\text{ns}$ )	Rel. Std. Des. (%)
0.05	383.81	33.23	8.66
0.1	922.68	73.97	8.02
0.15	1485.10	119.90	8.07
0.2	2053.78	166.39	8.10

Table 4.3: Average, standard deviation and relative standard deviation of 10 different samples of single clad fibers.

Led Int. (mA)	Average ( $\gamma/\text{ns}$ )	Std. Des. ( $\gamma/\text{ns}$ )	Rel. Std. Des. (%)
0.05	376.68	14.96	3.97
0.1	870.87	34.58	3.97
0.15	1396.60	55.24	3.95
0.2	1932.57	76.02	3.93

Table 4.4: Average, standard deviation and relative standard deviation of 10 different samples of multi clad fibers.

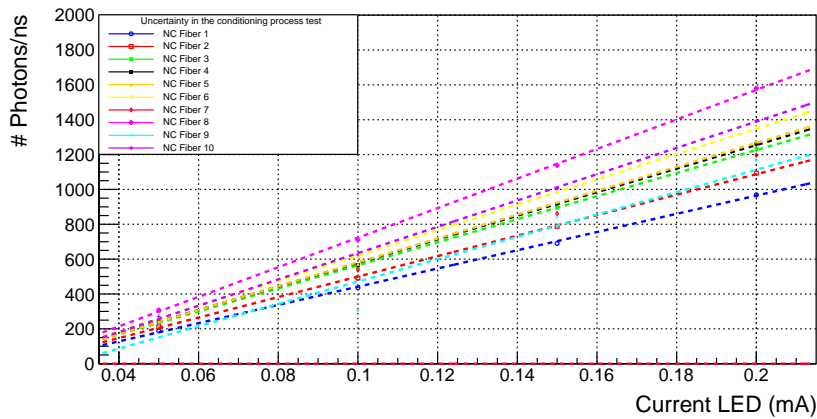


**Figura 4.15** – Number of photons/ns reaching the PMT for No Clad fibers.

what happened with the previous test, single clad and multiclads fibers, both, have higher signals than no clad fibers, which means that the clad has an appreciable effect on the fiber collection efficiency and it could be a possible point to future studies since, as we have said before, it is possible to develop our own fiber clad using the electrodeposition technique, with which we can create layers as thin as tens of nanometers.

Again, similar to what happened in the previous study, single-clad fibers have higher collection efficiency than multiclads fibers, something that has been verified in all our tests.

The relative standard deviation are also presented in these tables, where we can see that the dispersion of each fiber type for different LED intensities is practically negligible in each type of fiber, which again verifies the correct behavior of the system.

There is only one point (no clad fiber with 0.1 mA) that is higher than we expect. We can see in Table 4.2 that the reason for this is that its standard deviation is too high (as high as the measurement for no clad fibers with 0.15 mA). The reason was found in the sample 9, whose measurement

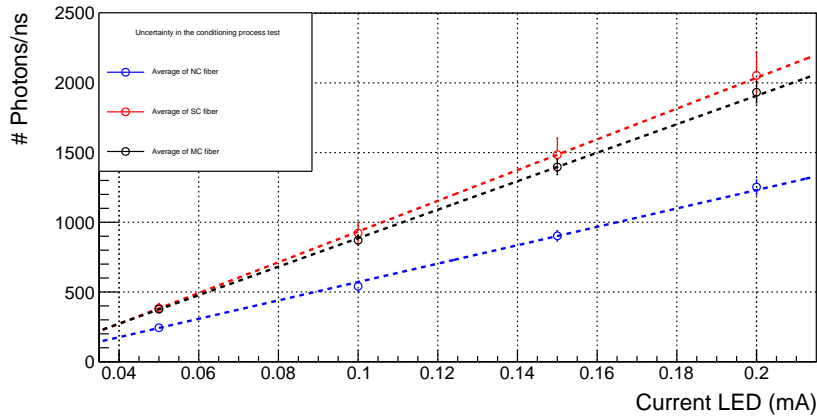


**Figura 4.16** – Average of 10 samples for each fiber type (no clad, single clad and multiclad fibers).

was very different from the average, increasing the standard deviation, probably because we did not wait enough time for system stabilization. We discard this sample because this result is not representative.

To uniform the results, an average of these four values is calculated for each fiber type and shown in Table 4.5, where the uncertainty in the fiber position, previously calculated, and the uncertainty due to the conditioning process, calculated using the equation 4.3, are also shown.

Fiber type	$\sigma_t$ (%)	$\sigma_{pos}$ (%)	$\sigma_{con}$ (%)
No Clad	4.01	3.37	2.17
Single Clad	8.21	2.17	7.92
Multiclad	3.96	1.04	3.82

Table 4.5: Relative standard deviations ( $\sigma_t$ ,  $\sigma_{pos}$  and  $\sigma_{con}$ ) measured in this test.

As we can see, the least uncertainty in the conditioning process is found in the no clad fibers, which means that the main damage from this process occurs in the fiber clad. It's something that was seen in Figure 4.4.

It has been seen under the microscope that this damage only occurs at the end of the fiber, where we cut and polish it.

Also, the largest relative standard deviation in this process is recorded for single clad fibers, which means that the second clad increases the resistance of the fiber to this process.

In summary, as a result of these tests we have seen that, on the one hand, the use of fiber clad improves the photon collection efficiency, which could be an interesting point for future studies. As we have said before, it is possible to develop our own fiber clad using the electrodeposition technique, with which we can create layers as thin as tens of nanometers.

On the other hand, we have quantified the relative statistical deviation due to the fiber conditioning process developed in the TRITIUM experiment, where it has been seen that the fiber clad is the main damage of this conditioning process so, if we want to develop a method to create our own clad, it should be applied after the fiber conditioning process.

Finally, the measurement of the photon collection efficiency of each type of fiber is shown. The collection efficiency is the percentage of photons collected along the fibers. It is usually given by the manufacturer per meter of fiber,  $EC_{100}$ .

To measure it, we prepare ten different samples of 10 cm in length for each type of fiber and measure each one using the set up previously explained. Then, the average and standard deviation was calculated for each type of fiber using the equations 4.1, whose results are shown in Table 4.6.

The collection efficiency can be calculated by comparing these tests with those performed for a fiber length of 20 cm, whose values has been previously shown in Tables 4.2, 4.3 and 4.4 since both have been made under the same conditions. The results is shown in Table 4.7:

Led Int. (mA)	No clad ( $\gamma/\text{ns}$ )	Single clad ( $\gamma/\text{ns}$ )	MultiClad ( $\gamma/\text{ns}$ )
0.05	$318.35 \pm 61.34$	$549.62 \pm 70.79$	$480.35 \pm 83.72$
0.1	$735.65 \pm 143.02$	$1269.91 \pm 164.32$	$1110.66 \pm 193.44$
0.15	$1183.91 \pm 232.07$	$1983.93 \pm 230.97$	$1777.40 \pm 307.19$
0.2	$1645.18 \pm 323.76$	$2506.97 \pm 208.01$	$2338.43 \pm 350.24$

Table 4.6: Average and standard deviation of 10 different fibers of 10 cm.

Fiber type	$CE_{10}$ (%)	$CE_{100}$ (%)
No Clad	$75.97 \pm 7.61$	$7.597 \pm 0.761$
Single Clad	$77.96 \pm 5.66$	$7.796 \pm 0.566$
Multiclad	$82.60 \pm 7.24$	$8.260 \pm 0.724$

Table 4.7: Collection efficiency of each fiber type for 10 centimeters,  $CE_{10}$ , and 1 meter,  $CE_{100}$ .

We have to keep in mind that the difference between the fiber length in both studies is only 10 cm, so the collection efficiency calculated from these measurements,  $CE_{10}$ , is only at that distance. The collection efficiency is normally given at a distance of one meter so, assuming that this parameter has a linear dependence with the distance, we can extrapolate it, whose value is shown in the last column,  $CE_{100}$ .

The collection efficiency per meter given by the manufacturer Saint-Gobain is between 7% and 3.44% [78]. We are using collimated photons for that so we can guess that we are in the best situation, 7%.

As can be seen in Table 4.7, our measured values are very close to the one provided by the manufacturer. The difference between this value for the three types of fiber studied is not as great as we expect. We have to take into account that we are using a difference in fiber length of only 10 cm and it may not be enough to see this effect. It might be interesting to repeat these tests with a greater difference in fiber length.

## Cleaning Process for Scintillating Fibers

Finally, an addition step was included to the fiber conditioning process, which is applied to improve the photon collection efficiency of the fibers.

As we have seen before, the tritium events detected in the fibers produce few photons, so it is very important to conserve as many photons as we can until they are detected by the photosensors. As we have also seen in our fiber characterization study, the quality of the interface that is created between the core of no clad fibers (used in the TRITIUM detector) and the environment (tritiated water in our case) greatly affects collection efficiency.

Therefore, a mechanism, called the fiber cleaning process, was applied to improve the state of this interface. This mechanism aims to remove all external particles deposited on the fibers, such as fat molecules deposited when the fibers are touched, which can affect the quality of the interface, worsening their photon collection efficiency.

As a consequence of this cleaning process, the wetting property of the fibers, shown in Figure 4.17, is improved, preventing air molecules from attaching to the fiber and achieving a uniform water clad around each fiber and, therefore, improving their collection efficiency.

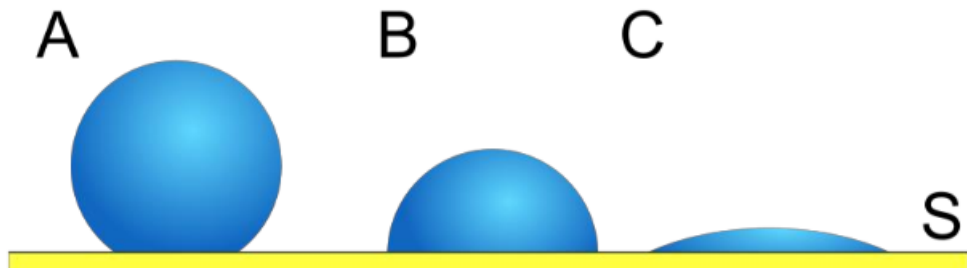


**Figura 4.17** – Wetting property produced by the cleaning process. []

The cleaning process used was carried out within a clean room at ICMOL laboratories<sup>4</sup> and it was developed by their researchers.

It consists of filling three different beakers, one with alkaline soap, another with millipore water<sup>5</sup> and the last one with isopropanol. First, the fibers must be rubbed for 5 minutes with alkaline soap and then placed in the first beaker for sonication for 3 minutes. Then, the fibers must be cleaned with a constant flow of water for 5 minutes. Second, the fibers will be placed in the second beaker for sonication for another 3 minutes, and third, they will be placed in the third beaker for sonication for another 3 minutes. Finally they will be dried with an  $N_2$  air gun and introduced inside of the prototype.

The improvement in fiber response was verified using a bundle of twenty fibers with a length of 15 cm that was prepared with the conditioning process previously described. This bundle of fibers was arranged in the setup described in Figure 4.8 and a measurement was taken. Then ,these fibers were cleaned with the fiber cleaning process and a measurement was taken again in the same conditions.

Two radioactive sources were used in this study, a beta source,  $^{90}\text{Sr}$ , which is the same as that used in the polishing machine test, and a gamma source,  $^{137}\text{Cs}$ , whose activity was ...

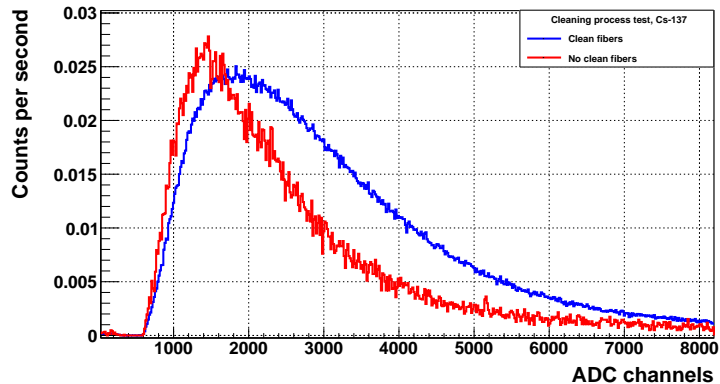
The results are shown in Figures 4.18, where we can see a shift of the spectrum to the right.

To quantify this improvement we can make a rude approximation and we can calculate the relative displacement of the peak of the spectrum using the equation 4.5, where  $A_C$  is the counts per second measured after the cleaning process and  $A_{NC}$  is the counts per second measured before the

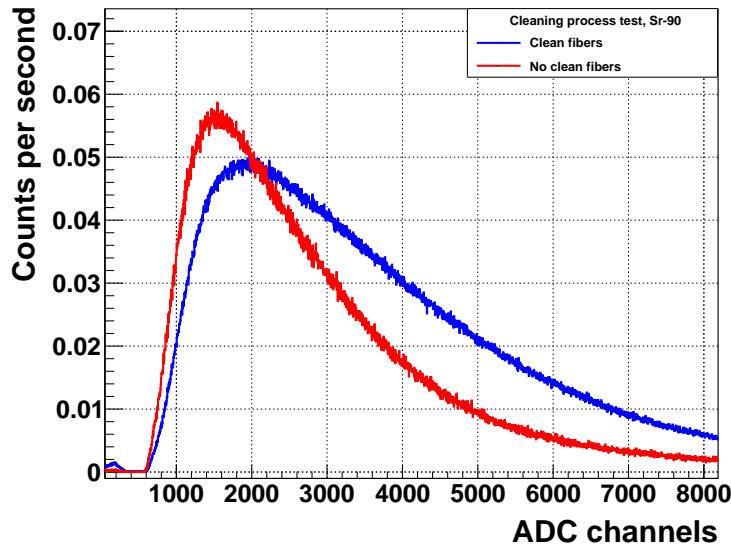
---

<sup>4</sup>ICMOL, Institute of Molecular Science, is a research institute located in the Science Park of the University of Valencia.

<sup>5</sup>The millipore water is...



(a) Energy spectrum recorded for the Cs-137 source.



(b) Energy spectrum recorded for the Sr-90 source.

**Figura 4.18** – Energy spectrums used to test the effect of the Cleaning process

cleaning process.

$$F(a, b) = \frac{A_C - A_{NC}}{A_C} \quad (4.5)$$

The improvement obtained is 20.74% for the gamma source and 20.99% for the beta source so, we have verified that we can improve the photon collection efficiency of the fibers using the cleaning process carried out in the clean room of ICMOL laboratories. Nevertheless, we have to keep in mind that this test was carried out in air and it could be interesting to repeat it in water to obtain more realistic conclusions since the fibers of the TRITIUM detector will be immersed in water.

## 4.3 Characterization and R&D on SiPM

This section describe the work that has been carried out to characterize the SiPMs used in the TRITIUM experiment, model S13360-6075 from Hamamatsu Photonics company. It will consist of measuring some of the most important parameters of this SiPM that will affect the tritium measurement such us their break down voltage or their gain.

Furthermore, a temperature compensation method has been developed and experimentally tested to compensate for temperature variations of the SiPM since it has been seen to greatly affect to its correct operation and, therefore, the measurement of tritium.

The setup used in this characterization is shown in section 3.2.4, Figure 3.21. Furthermore, these measurements were performed inside of a climatic chamber whose temperature and humidity were controled with a precision of  $0.1^\circ$  and 0.1% respectively. We have to take into account, when the system was stabilized, variations with the same size of this precision were observed.

First of all we measured to breakdown voltage of the SiPM and their quenching resistance which was calculed from the measurement of their current-voltage curves. To measure it we need to work without amplification of the electronic system so, insatead to use the second and third PCB, we connected the output of the black box directly to the picoammeter previously mentioned [91]. A LabView program was used to automate the taking of measurements.

On the one hand, we feed the SiPM using a forward bias voltage from 0 V to 1.58 V in steps of 0.005 V, whose result is shown in Figure ??.

FIGURAAA

EXPLICACIOON

On the other hand, we feed the SiPM using the reverse bias voltage...

the black box output was connected directly to the keithley to measure the current and using

This calibration will consist of two different parts. On the one hand, we measure the IV curves of the SiPM, from which we will calculate the breakdown voltage and the quenching resistance of the SiPM and, on the other hand, we will measure energy spectrums from which we will calculate the gain of the SiPM, the equivalent capacity of the SiPM, etc.

To measure the energy spectrums we will use the setup shown in section ?? and to measure the IV curves a small modification of this setup will be made which consists of...

Pequeñas zonas de deplexión crean grandes capacidades que producen alto ruido de los SiPMs

Trabajo de Fernando Hueso.

Explicar electrónica que se utiliza como la tarjeta y demás. Poner el esquema electrónico de la tarjeta y referencia a Marc de NEXT por haberla construido. Explicar la forma del pulso como en la tesis de Katerina Asnar

Paper de Nadia para la PDE.

Las medidas se han hecho en la camara del IFIMED (ver lo que tengo apuntado en el TFM y dar gracias al IFIMED)

la banda prohibida es pequeña por lo que algunos electrones pueden excitarse termicamente y pasar a la banda de conducción -> RUIDO Cuando hable del ruido, afterpulses, crosstalk... intro en MPPC hammatsu data sheet

cuando hable de la capacidad del SiPM utilizar el punto 10.3.2 del Leo -> pag. 226

resumen de como varía cada magnitud con la temperatura y el voltaje. Tesis SiPMs.

Inocherent light source!

fired cells.

paper NADIA

### B. Photon Detection Efficiency -> entero.

Aunque el aumentar el voltaje inverso mejora la eficiencia de detección de fotones, también aumenta la corriente oscura. Reducir la temperatura sin embargo disminuye la corriente oscura.

Para contar el número de veces que dos o más fotones son detectados simultáneamente, el umbral les establecido en  $N - 0.5$  p.e. (donde  $N$  es un número arbitrario de fotones). Al contar el número de pulsos que exceden este umbral se puede saber el número de veces que se han detectado simultáneamente  $N$  o más fotones (Manual Hamamatsu, 2008, 2007)

En este trabajo se estudió tanto la variación en la resolución en energía de un SiPM como la variación del centroide de un pico (explicado a detalle en los próximos capítulos) con la temperatura y el voltaje. Para ello se estableció una electrónica de adquisición adecuada para la mayor eliminación de ruido posible y óptima resolución (explicada en el Capítulo 3).

Superponer 2 plots con el LED a distintos voltajes (2 o mas... probar varios voltajes a Vov recomendado y quedarnos con los mejores).

Figura 11 de la tesis de cristales monolíticos

La ganancia M, depende exponencialmente de la tensión de polarización inversa del dispositivo (Fig. 11, derecha). Sin embargo, en la región de operación de los APDs con  $M = 100$ , un cambio relativo de tensión de polarización corresponde a un cambio lineal en la ganancia, con pendientes típicas de 10 %/V. Además, la temperatura debe estar debidamente estabilizada en un sistema con APDs ya que estos detectores sufren variaciones importantes con la temperatura, típicamente 2-3 %/ oC

Todo el apartado de SiPMs de esta tesis.

Cuando hablamos del PDE: El número de celdas de un SiPM dependerá de la aplicación específica. Será lo suficientemente elevado para detectar la cantidad de fotones esperada pero sin exceder innecesariamente este valor, ya que cada celda necesita de espacio para las resistencias de quenching de cada APD y para la separación y aislamiento entre las diferentes celdas. Cuanto mayor sea el número de celdas, mayor será el espacio muerto y menor su eficiencia. Por el contrario, un número de celdas inferior con celdas de mayor tamaño, implica una alta eficiencia de detección de fotones (Photon Detection efficiency, PDE) pero un rango dinámico bajo. La PDE en un SiPM se define como su eficiencia cuántica por el ratio entre el área sensitiva y el área total del dispositivo, lo que se conoce como factor de llenado (fill factor) y se representa con “epsilon”, por la probabilidad de que un fotoelectrón comience un proceso de avalancha (Ec. 19). Aparte de la longitud de onda,

Este parrafo justirca porque me quedo con el SiPM array de area de SiPM mayor... debido a la sensibilidad... punto 4.2 de la tesis de SiPM (LARGA)

the noise level scales with the area of the device.

If each ionization process could be considered independent of the others, the fluctuations would then be described by a Poisson distribution where the variance ( $\sigma^2$ ) would be equal to the mean number of ion-

ization electrons,  $N_I$ . However, the fluctuations in the mean number of ionization electrons present a lower value, as predicted by Fano's theory [66], being proportional to a factor  $F$ , known as the Fano Factor, which multiplies the mean primary ionization yield.

Tiene un factor de amplificación interno que depende exclusivamente de las características de la unión p-n y de la resistencia quenching

## 4.4 Characterization of the Ultrapure Water System

This section shows the characterization of the ultrapure water system, whose objective is to ensure that the quality of the output water sample of the ultrapure water system, purified water from now on, is good enough to overcome the requirements of the TRITIUM detector. There are three different requirements that this ultrapure water system must meet:

- First of all, we need to achieve a low enough conductivity<sup>6</sup> of the water, around  $10 \mu\text{Sv}/\text{cm}$ , so that external particles dissolved in the water don't be deposited on the fibers, drastically reducing the detector efficiency due to such a low mean free path of the tritium electron.
- Second, we must note that this system does not have any spectral capabilities that can be used to distinguish between several radioactive isotopes, so to measure only tritium, this system must remove all external radioactive particles (other than tritium isotope) from the sample.
- Lastly, the tritium activity should not be affected by this process.

To verify that these requirements have been exceeded, a characterization of the water sample was carried out before and after the ultrapure water system, called raw water and purified water respectively, which consists of measuring the water sample conductivity and the activity of each radioactive element that are present in the sample. The turbidity and the chemical components of the water sample will also be measured.

It must be taken into account that, so that the sample was representative of the raw water sample, it was taken from a tap located very close

---

<sup>6</sup>Conductivity is the ability of the material to conduct electrical current. In liquids, conductivity is related to the presence of salts (presence of positive and negative ions)

to the input of the ultrapure water system, which is located at 40 meters from the TRITIUM monitor and two meters deep. It has been seen that it is very important to take the sample where we introduce the sample to the ultrapure water system since variations of up to 25% in the tritium activity has been measured between both points (due to its diffusion).

First, the chemical components of the water were measured before the ultra-purification process by a physico-chemical analysis, which was carried out a few years ago. It is shown in Table 4.8.

Chemical components	Concentration (mg/L)
$\text{CO}_3\text{H}^-$	154
Mg	46
Ca	105
$\text{NO}_3^-$	16
$\text{Cl}^-$	196
$\text{NO}_2^-$	0.03
K	11
Na	173
$\text{SO}_4^-$	217
Dry Residue	1029

Table 4.8: Chemical components and turbidity measured in the raw water sample.

EXPLICACIÓN DE ESTA. SE SUPONE QUE LA AGUA PURIFICADA NO POSEE NADA DE ESTO???

Its turbidity<sup>7</sup> was also measured using the Hanna Hi 9829 portable multiparameter system from Hanna Instruments [127], obtaining a value of 29 NTU.

Second, the conductivity was measured for both, raw and purified

---

<sup>7</sup>The turbidity of water is the loss of its transparency due to dissolved particles, normally measured in NTU, Nephelometric Units of Turbidity, which measure the intensity of the scattered light at 90 degrees.

water. To do so, the same multiparameter system was used, the Hanna Hi 9829. These measurements, together with the measurement of the conductivity of reject water(explained in section 3.3.2), are presented in Table 4.9.

Date	Raw ( $\mu\text{Sv}/\text{cm}$ )	Pure ( $\mu\text{Sv}/\text{cm}$ )	Reject ( $\mu\text{Sv}/\text{cm}$ )
1/8/18	970	11.85	1442
7/8/18	958	11.8	1632
14/8/18	966	12.04	1725
22/8/18	980	12.54	1702
28/8/18	987	9.9	1692
5/9/18	1009	12.02	1645

Table 4.9: Measurements of the conductivity for several samples of each water type (raw water, pure water and reject water).

As can be seen in the first column, we have too high values of conductivity of raw water to be introduced directly into the tritium detector. The reason of that is because this type of water contains many different ions(saw in Table 4.8) that we have to eliminate to prevent them from depositing on the fibers.

We can see in the second column that the conductivity values of pure water have been reduced by almost two orders of magnitude, reaching values close to  $10 \mu\text{Sv}/\text{cm}$ , our initial objective, exceeding this requirement.

Finally, as can be checked in the third column, the reject water has high values of conductivity. The reason of that is because it contains the ions that has been removed to the pure water.

Third, each different radioactive element present in the water samples of both types, raw water and purified water, was identified and their activities was measured. For this task, a high purity germanium detector, HPGe, was used to measure this samples and a gamma analysis was carried

out to find the natural gamma emitters (those that come from the natural radioactive series, Table 3.4) and artificial gamma emitters with long enough lifetime to be measured (those that come from the activation of nuclear fission of neutrons).

The energy spectrum of these measurements is presented in Figures ... where the different elements can be identified and their activities are shown in Table...

#### FIGURAAAAS y tablaaa

As can be seen in Figures ... we have several radioactive elements in the raw water sample whose activities are not negligible compared to the activity of the tritium we intend to measure 100 Bq/L. Therefore, as we have said, it is very important to remove these elements to the water sample as it will affect the tritium measurement.

As we can see in Figure ??, these radioactive elements have been completely eliminated after the ultrapurification process leaving only tritium in the water sample, achieving to exceed other requirements for the ultrapure water system.

Lastly, the tritium activity was measured to see how it is affected by the ultra-purification process. This measurement was carried out using the Quantulus system, which consists of a liquid scintillator, which has been mixed with tritiated water, readout by PMTs.

Before this measurement, each water sample was filtered at 0.45 microns to remove any particles that would affect the extinction of the scintillation signal.

The Table 4.10 show several measurements of the activity for different tritium samples of each water types (raw water, reject water and purified water).

Date	Raw (Bq/L)	Pure (Bq/L)
7/8/18	$24 \pm 3$	$26 \pm 4$
11/12/19	$13.2 \pm 2.1$	$13.85 \pm 2.2$
15/01/20	$30.6 \pm 4.2$	$30 \pm 4$

Table 4.10: Measurements of the activity for several samples of both water types (raw water and pure water).

As can be see, tritium activity is not affected by this system, exceeding the last requirement of the ultrapure system. We have checked that the tritium activity of reject water is also the same.

## 4.5 Characterization of the TRITIUM Cosmic Veto

Finally, this section shows the characterization of the active shield (cosmic veto), whose physical configuration has been explained in section 3.4.2. This characterization has been carried out using PMTs as photosensors as shown in Figure 3.25, which are readout using the electronic configuration shown in Figure 3.17b. Their replacement by SiPMs will be a future study to quantify its improvement to the tritium measurement.

First of all, we have to find the conditions in which the detection of cosmic events will be optimized by our active veto. It consists of, on the one hand, finding the minimum high voltage of PMTs in which their efficiency is stable, and, on the other hand, finding the maximum threshold of the discriminator, which has to be overcomed by the output signals of the PMTs to contribute to the cosmic detection, at which we start to loss cosmic events in their detection. For higher high voltage and smaller thresholds of the found values, a plateau should be found.

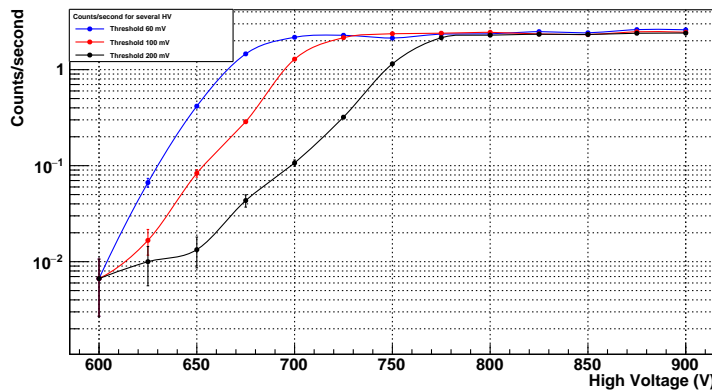
To find both parameters, several measures of the number of coincident events (cosmic events) were done. On the one hand it was measured at several high voltages and fixed thresholds and on the other hand it was measured at several thresholds and fixed high voltages. Both measurements are shown in Figure 4.19 in which a semi-logarithmic scale has been used.

A modification of the electron configuration has been made only for finding these optimal conditions, which consists of using the electronic configuration shown in Figure 3.17b where the amplification part has been eliminated and the output signal of the coincidence module, second stage, is connected to a CAEN Quad Scaler And Preset Counter-Timer module, N. 1145, [128], which is used to count the number of events in a time window (300 seconds in our case).

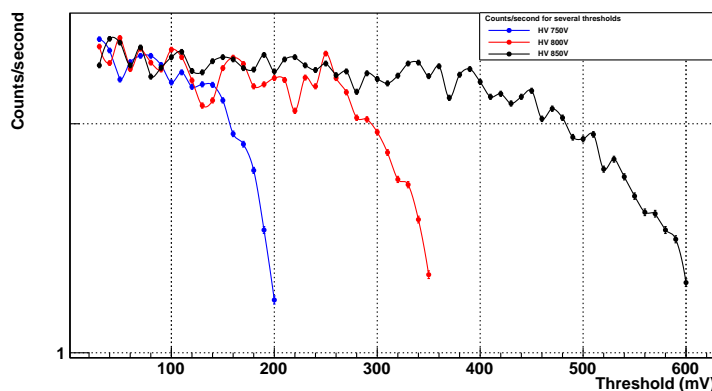
In Figure 4.19a, the measurements at several high voltage and a fixed thresholds is shown, which have been done for three different thresholds, 60 mV, 100 mV and 200 mV. As can be seen, there is a minimum high voltage for each threshold used, 700 V, 730 V and 780 V respectively, at which the plateau start. As we can see this minimum voltage is higher when we increase the value of the threshold, as we should hope. The voltage chosen to work is 800 V since we can be sure of being on the plateau for the three thresholds.

In the same way, in Figure 4.19b, the measurements at several thresholds and a fixed high voltage is shown, which have been done for three different high voltages, 750 V, 800 V and 850 V. As can be seen, there is a maximum threshold for each high voltage used, 140 mV, 270 mV and 450 mV respectively, at which the plateau ends. Now, we can see that this maximum threshold is increased for higher voltage, as we should hope. The threshold choosen to work is 200 mV since, for our last election 800 V, we can be sure of being on the plateau.

Next, the energy spectrum of cosmic events was measured, which



(a) Counts per second for several high voltage at three different thresholds.



(b) Counts per second for several thresholds at three different high voltage.

**Figura 4.19** – Counts per second at several high voltage and fixed thresholds and several thresholds and fixed high voltage.

is shown in Figure 4.20. For this task the electronic configuration shown in Figure 3.17b was used with the values previously mentioned, 800 V and 200 mV.

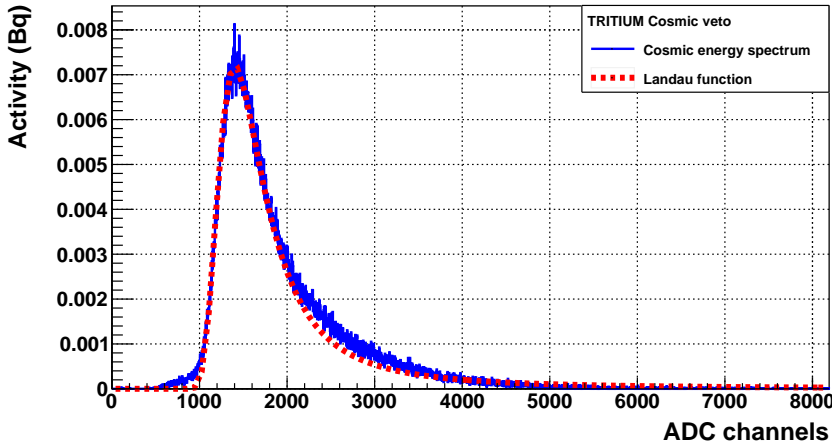


**Figura 4.20** – Energy spectrum measured with the cosmic veto.

As we can see, this energy spectrum fits well with a landau function as expected. Now, the number of detected cosmic events can be known by calculating the area integral of this spectrum, whose result is 2,5 event/s. The theoretically expected cosmic rate was calculated in section 3.4.2 for our cosmic vetos, 2,909 event/s, so the efficiency of it for cosmic events can be calculated, whose value is 85%, which is a common value of the efficiency of this type of detectors.

Finally the relationship between the detected cosmic events and the distance between both detectors that form the cosmic veto was obtained. It is interesting because this distance can be changed if other tritium prototypes are used and we need to know the expected cosmic rate for each different situation.

To do so, an energy spectrum was measured for five different distances, 10.4 cm, 20 cm, 36 cm, 39.8 cm and 50 cm, which is shown in

Figure 4.21. The energy spectrum previously shown in Figure 4.20 was also included.

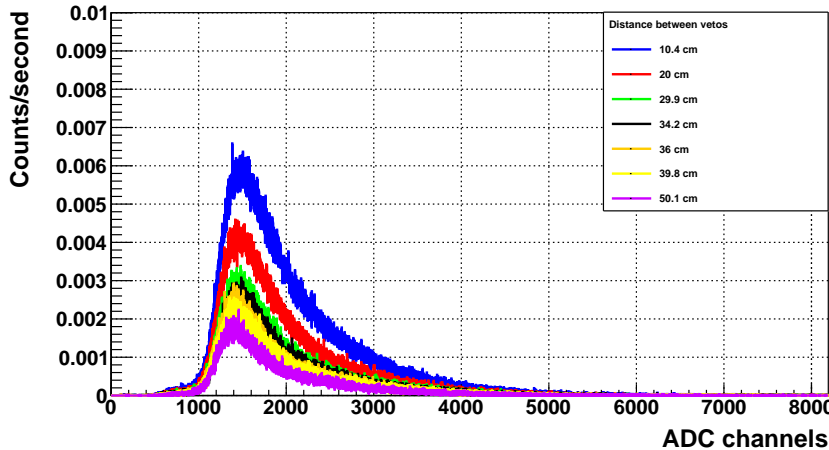


**Figura 4.21** – Energy spectrum of cosmic vetos for several distance between cosmic detectors.

As we can see, the shape of the spectrum is the same because the energy of the detected events is the same (cosmic events) but the quantity of their events is less for greater distance. The reason for that is that when we increase the distance, the solid angle formed by the active veto is smaller.

The detected cosmic events was calculated by the area integral and they are represented in Figure 4.22 where a linear fit has been added. With this linear fit, the detected cosmic rate can be easily known whatever the working distance.

Falta poner la medida antes y despues de cubrir el detector.

También se realizaron varias medias para ver como afecta una fuente gama. Discutir con Pepe como plantear esta medida o si merece la pena ponerla o no.

Como es de esperar esta deja muy poca señal en el centelleador ya

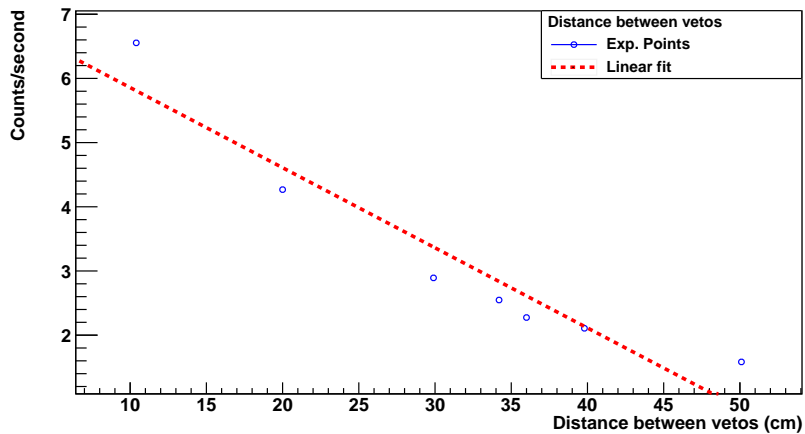


**Figura 4.22** – Linear fit of the counts per second measured with the cosmic veto with several distance between its cosmic detectors.

que este tiene muy poca eficiencia para gammas.

0



# Chapter 5

## TRITIUM Monitor Prototypes

### 5.1 Introduction

This chapter describes the different prototypes that have been developed in the framework of the TRITIUM experiment, which are Tritium-IFIC 0, Tritium-IFIC 1, Tritium Aveiro 0 and Tritium-IFIC 2, listed in chronological order of their construction.

On the one hand, the first two prototypes built were preliminary prototypes used to learn about tritium detection and to detect and solve problems in their designs.

On the other hand, the other two prototypes built were prototypes with a well-defined design in which no problems were found. They were built to check more subtle effects.

Each prototype was designed and built in our own workshops (at IFIC, Valencia or Aveiro, Portugal) and it was filled with tritiated water following a protocol specially developed for this task.

In each prototype used, several tightness and filling tests were carried out to guarantee their radiosecurity.

Finally, in the last section, the final monitor of TRITIUM detector will be explained. It is based on modular detection units for easy scalability, where each module will be the chosen prototype (the one with the best results) previously shown throughout this chapter.

## 5.2 Preliminary IFIC prototypes, TRITIUM-IFIC 0 and TRITIUM-IFIC 1

Two preliminary prototypes, Tritium-IFIC 0 and Tritium-IFIC 1, are shown in this section, which were designed, developed and built at the IFIC workshop.

These prototypes were thought to be a small scale of the final tritium detector module and, as we have said before, they were used to learn about tritium detection, to detect possible problems in their designs and to verify the improvements applied to them.

### 5.2.1 TRITIUM-IFIC 0

The Tritium-IFIC 0 prototype was the first prototype developed in TRITIUM experiment and it was used to check the feasibility of the technology proposed by TRITIUM, that's, to verify that we are capable of detecting tritium in water with scintillating fibers.

Due to the complications that arise when liquid radioactive sources are used, the design of this first prototype paid special attention to radiation safety, rather than in detecting tritium efficiency.

The Tritium-IFIC 0 consists of bundle of 35 fibers, shown in Figure 5.1, whose length is 20 cm, which were cut and polished with the techniques explained in section 4.2. This bundle has a metallic pieze located in both ends, Figure 5.1a, which are used to fix it to the prototype.

This bundle is placed inside of a vessel, whose material is PVC<sup>1</sup> since it is a safe material widely used. This vessel, shown in Figure 5.2, was

---

<sup>1</sup>Polyvinyl Chloride

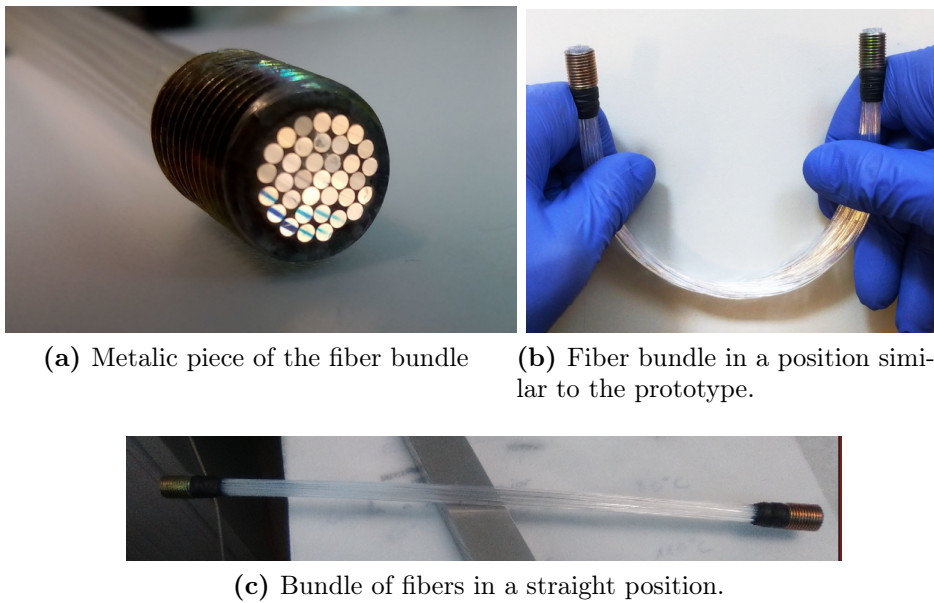


**Figura 5.1** – Bundle of 35 fibers, whose length is 20 cm, used in Tritium-IFIC 0 prototype

designed in a U-shape because, in this way, radiological safety was improved, although this shape worsen the efficiency of tritium detection.

As can be seen in Figure 5.2, a piece of methacrylate and steel was designed and built to hold the detector and two calibrated PMTs were optically coupled directly to the fiber bundle ends using optical grease [125].

The used PMTs were the model R8520-460 from Hamamatsu company [83], whose reference number are ZB2771 and ZB2773, and their signals were precessed and analyzed using the electronic configuration shown in Figure 3.17a.

A commercial voltage divider electronic circuit, whose electronic scheme is shown in Figure 3.9, was used in each PMT and they was powered to  $-800$  V, at which their gain are  $1.26 \cdot 10^6$  and  $1.01 \cdot 10^6$  and their quantum efficiency are 29.76% and 28.66% respectively.

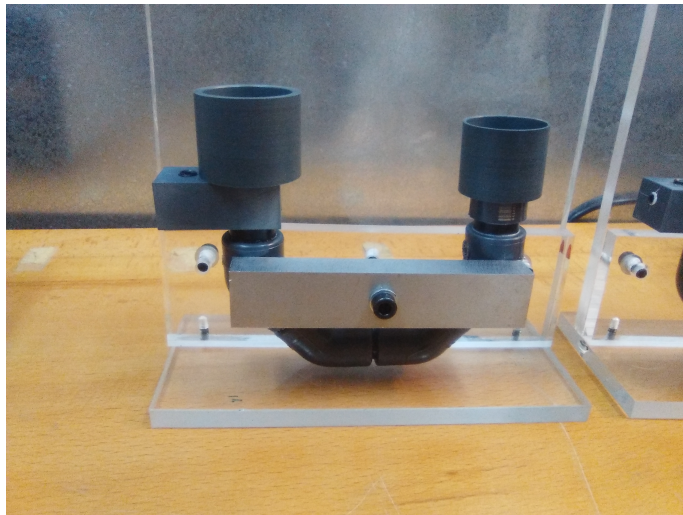


**Figura 5.2** – Tritium-IFIC 0 Prototype.

Two identical prototypes were built and filled following the same protocol but using different liquid solutions.

The first prototype, called Tritium-IFIC 0 Background, was filled only with ultrapure water ( $39 \text{ cm}^3$ , uncertainty of 0.05%) and it was used to measure the background of our detector whereas the other prototype, called Tritium-IFIC 0 Signal, was filled with a radioactive liquid source of tritium, the preparation of which is explained in the appendix E.

The activity of this liquid source of tritium is  $99.696 \text{ kBq/L}$  (uncertainty of 2.24%) and the volume used to fill this prototype was the same as the other,  $39 \text{ cm}^3$  (uncertainty of 0.05%). Therefore, the total activity of this tritiated water sample is approximately  $3.888 \pm 0.087 \text{ kBq}$ .

This second prototype was used to measure the signal of our detector (tritium + background) and the measured tritium activity can be known by extracting the background (measurement of Tritium-IFIC 0 Background) to the signal (measurement of Tritium-IFIC 0 Signal).

A statistically significant amount of time coincident events was not found in both PMTs, which means that the photons produced by a single tritium event cannot reach both PMTs. Therefore the measurement of time coincidence was not possible.

This loss of photons could be caused for several reasons, such as the excessive curvature in the fiber bundle due to the U-shape of Tritium-IFIC 0 prototype, which cause that too many photons escape from the fibers. This loss of photons could also be caused by poor quality of the tritiated water-fiber interface. In fact, the cleaning process explained in section 4.2 was motivated by this result.

To avoid this problem and obtain some results with this prototype, a measurement was performed with a single PMT. For this task, a small modification of the electronic configuration was done, in which we didn't use any coincidence stage. Therefore, the coincidence gate will be created using the PMT signals that exceed a threshold predefined by the user (the output signal of the discriminator module is connected as input of the Gate & Delay Generator module). The result of this measurement is shown in section 7.2.1, where it will be discussed.

Furthermore, a test was carried out to find an explanation why it was not possible to measure both PMTs in time coincidence. For this task a transparent PMMA vessel, shown in Figure 5.3a, was built in a similar shape to that of the Tritium-IFIC 0 prototype vessel to check the effect of the fiber bundle curve.

The LED shown in section 4.2 was used to verify the reduction in photocollection efficiency of the fiber bundle due to this curve.

As can be seen visually in Figure 5.3b, a large percentage of the photons are lost due to the curve. This problem will easily be solved by using a straight fiber arrangement in our next prototypes.

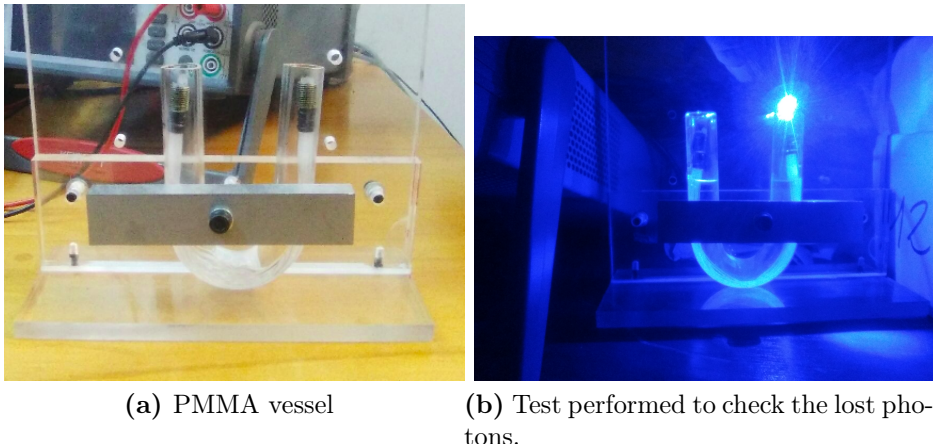


**Figura 5.3** – PMMA vessel used to check photon loss due to fiber bundle curve.

### 5.2.2 TRITIUM-IFIC 1

The next prototype, Tritium-IFIC 1, was intended to overcome the problems and limitations found in the previous prototype, section 5.2.1. To do so, some improvements were applied on it:

1. First, as we said before, the fiber bundle is arranged straight to optimize the photon collection efficiency of the fibers.
2. Second, a special fiber cleaning protocol, previously explained in section 4.2, was applied on the fibers. It was used to improve the interfaces between fiber and tritiated water, creating a better wetting property of the fiber, which will result in more tritium events detected and a greater photon collection efficiency.
3. Lastly, as we have seen in our previous fiber characterization study, shown in section 4.2, the photon collection efficiency of the fibers used is poor, so a large number of photons will be lost in each tritium event.

It is an inherent characteristic of the fiber which we cannot change but, to reduce its effect, we will use a Teflon vessel for Tritium prototypes.

Teflon is an interesting material for its optical properties, specifically its reflection factor, which is very close to 100% at the working wavelength. It means that practically all the photons that reach the walls of the vessel will be reflected back to the fiber.

Taking into account all this modification, the following prototype was designed, built and tested, whose name is Tritium-IFIC 1. It consists of 64 scintillating fibers, with a length of 20 cm, which are arranged in a straight position using a teflon structure, shown in Figure 5.4, in which these fibers are fixed in an  $8 \times 8$  square matrix.

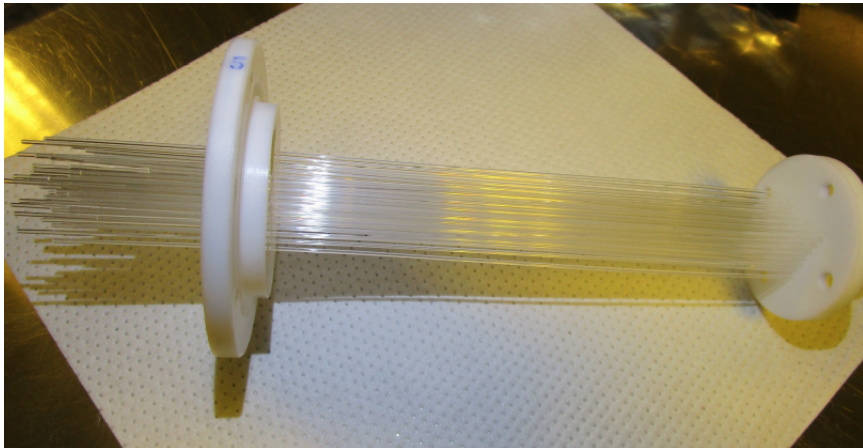


**Figura 5.4** – Teflon structure used to arrange the fibers of Tritium-IFIC 1 prototype in a matrix of  $8 \times 8$ .

A new teflon vessel was designed and built, shown in Figure 5.5. It has a cylindrical hole whose internal diameter and length are 48 mm and 200 mm respectively, where the fiber structure will be placed.

In addition to cutting and polishing the scintillating fibers used, a cleaning process, described in section 4.2, was applied to them to achieve a better tritiated water-fiber interface.

A general view of this prototype is shown in Figure 5.6, which, for

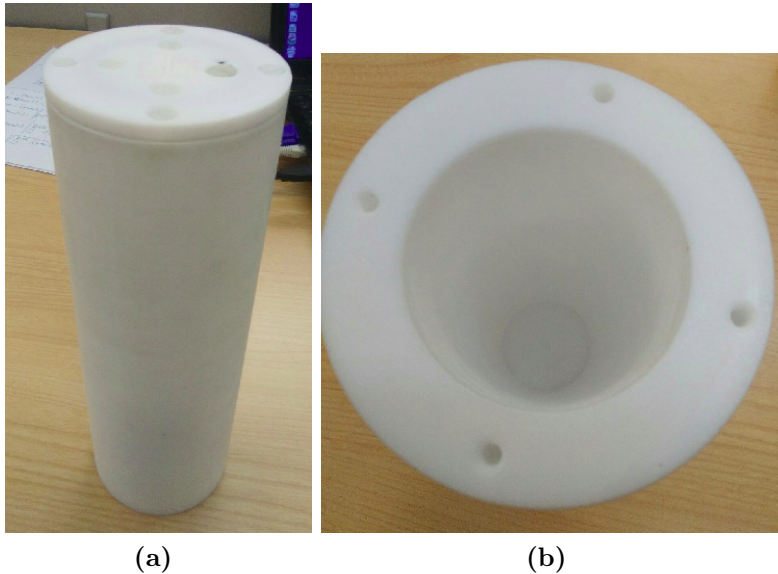


**Figura 5.5** – Teflon vessel of Tritium-IFIC 1 prototype

radioactivity safety reasons, will be read using only one PMT.

The PMT used was the model R8520-460, from Hamamatsu Photonics company [83] and it was coupled directly to the fiber bundle using optical grease [125]. It was powered at  $-800$  V, at which, its quantum efficiency is 28%.

The signal from this PMT was processed and analyzed using the same electronic configuration as that used for the Tritium-IFIC 0 prototype.

Unlike the previous prototype, only one Tritium-IFIC 1 was built. First, it was filled with ultrapure water (118 mL, uncertainty of 0.05%) and several background measurements were taken over a week. Then, it was emptied and refilled using 118 mL (uncertainty of 0.05%) of the radioactive liquid source of tritium explained in appendix E.

The result of this measurement is shown in section 7.2.2, where it will be discussed and compared with the result obtained with the previous

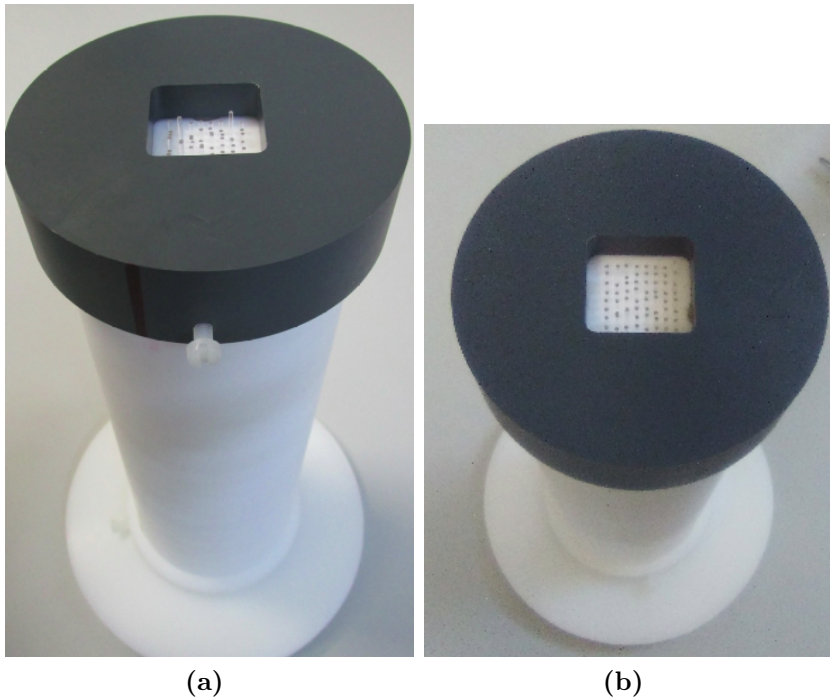


**Figura 5.6** – A general view of Tritium-IFIC 1 prototype

prototype, Tritium-IFIC 0.

## 5.3 Latest TRITIUM Prototypes

In this section the last two prototypes are shown, Tritium-Aveiro 0 and Tritium-IFIC 2, in which the problems previously found are solved and a well-defined design is developed for them.

A different design was developed for these prototypes so that they can allow the reading of a large number of fibers arranged in a straight position with two PMTs in time coincidence, in a safe way.

In these prototypes we pay particular attention to tritium detection efficiency, which is the reason why they use many more fibers than the preliminary prototypes and a time coincidence reading of these fibers is done using two photosensors.

Furthermore, the activity of the radioactive liquid source of tritium, which is used to fill these prototypes, will be lower since we are interested in measure their sensitivity.

The design of both prototypes is very similar and their objective is to test the subtle effects caused by the little difference, such us the diameter of the fibers used, and to choose the one with the best results which will be the final design of the Tritium detector module.

### 5.3.1 TRITIUM-Aveiro 0

The third prototype built and the first thought to be the final version of the TRITIUM detector module was Tritium-Aveiro 0, shown in Figure 5.7, which was designed and built in the Aveiro workshop.

It consists of a teflon vessel (D of Figure 5.7), shown in Figure 5.8, which has an internal cylindrical hole whose diameter and length are 43 mm

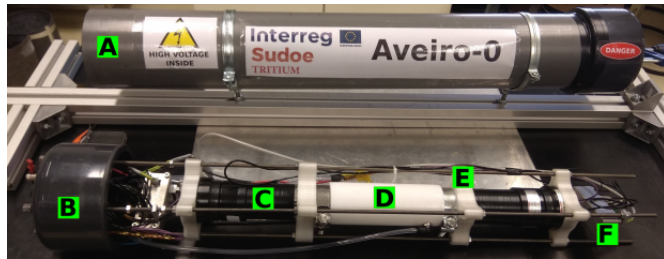


**Figura 5.7** – Tritium-Aveiro prototype.

and 180 mm respectively.



**Figura 5.8** – Teflon structure and fiber bundle used in Tritium-Aveiro 0 prototype.

This vessel contains 360 no-clad scintillating fibers with a length of 180 mm. The model of the used fibers is BCF-10 from Saint-Gobain company [130], which have practically the same characteristics than the others used up to now (BCF-12 fibers) and its most important difference is the diameter, which is the double, 2 mm.

On the one hand, a larger diameter could be interesting because it facilitates the flow of water around the fibers, reducing the problems related to surface tension and ensuring that the entire active volume of the fibers is used for tritium detection. In addition, it increase the resistance of the fibers, which is very important since the water is flow around them.

On the other hand, a larger diameter could be detrimental since it worsens the signal-to-background ratio. It happens because, with 2 mm fibers, the active volume that our detector has in the same space is smaller so its signal will be smaller and the part of the fibers where no tritium events reach (they only contribute to the background) is larger so the background will be larger.

In order to quantify the importance of the effect of the fiber diameter, which is needed to choose the best configuration, these measurements will be compared with similar measurements performed with Tritium-IFIC 2 prototype which, as we will see in next section, is based on a similar configuration with 1 mm fibers (BCF-12 model).

The amount of fibers used in Tritium-Aveiro 0 prototype is the maximum which allows the water to flow and, due to the large quantity of fibers used, these fibers are not feasible to use any structure to fix them. It should be noted that these fibers were cut with the fiber cutting device developed by TRITIUM but they were neither polished nor cleaned. The reason for this is that the automatic polishing machine was not yet developed and it was not feasible to polish 360 fibers by hand. In fact, the automatic polishing machine was motivated by the amount of fibers used in our last prototypes.

To ensure the radiosecurity of this prototype, the teflon vessel is totally closed and it has two PMMA windows, whose thick is 10 mm, located at both ends of the fiber bundle which will be used to read it. Two clamps are used to press the Teflon walls against the PMMA windows to ensure the watertightness of the prototype.

PMMA was chosen for its optical properties, especially its transmission coefficient, which was measured for visible light range in the ICMOL laboratories and it is shown in Figure 5.9.

As can be seen, its transmission coefficient is 95% for the working

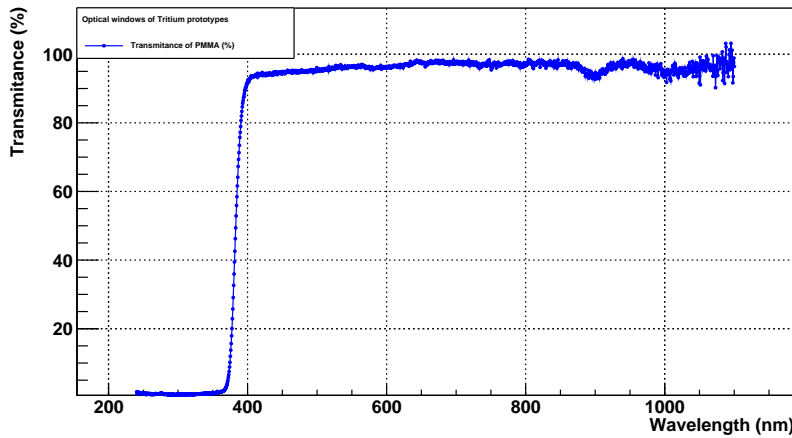


**Figura 5.9** – Transmission spectrum of light (in the visible range) in a piece of PMMA of X thickness measured in the ICMOL laboratory.

wavelength (435 nm), which means that the loss of the light in these optical windows is very small. Slightly better transmission coefficients can be achieved with other materials such as quartz or sapphire but they are much more expensive.

Two PMTs (C of Figure 5.7), powered at  $-1500$  V, are used to read this prototype in time coincidence. They are fixed to both fiber bundle ends of the prototype using two pieces (E of Figure 5.7) which has been designed and built with a 3D printer. Both PMTs are optically coupled to the PMMA windows using optical grease [125].

The PMTs used are the model R2154-02 2" from Hamamatsu company [131], whose characteristics, specially its gain and efficiency, are quite similar to the PMTs used in the other prototypes.

All these different parts, together with the electronic system (F of Figure 5.7), is arranged in a structure, seen in Figure 5.7, which is based on several nuts located on four long stainless-steel screws. These screws are fixed to an external PVC structure, A and B of Figure 5.7, which is used

to protect the prototype from physical damage and provide a light-tight operation environment. This PVC structure is equipped with several high voltage power, low voltage power and signals feed-through connectors.

Only one prototype was built, which was designed to be installed in the Arrocampo dam. To do so, on the one hand, a water inlet/outlet were installed in its Teflon vessel to allow a constant water flux through the detector and, on the other hand, several PCBs were specially designed, developed and tested to process and analyze the signals of this system.

On the one hand, a PCB, whose electronic scheme is shown in Figure 5.10, was designed to power the PMTs with a negative high voltage. It consists of several high voltage power supply, model C11152-01 from Hamamatsu company [132], one for each PMT used, which is controlled by a DAC<sup>2</sup>, model MAX5500 from Maxim Integrated company [133]. An Arduino Mega is used for the DAC communication and cross-checking the output values and it is connected to a Raspberry Pi to control the system.

A graphical interface, shown Figure 5.10b, has been developed to manage the different options of this system in a comfortable way.

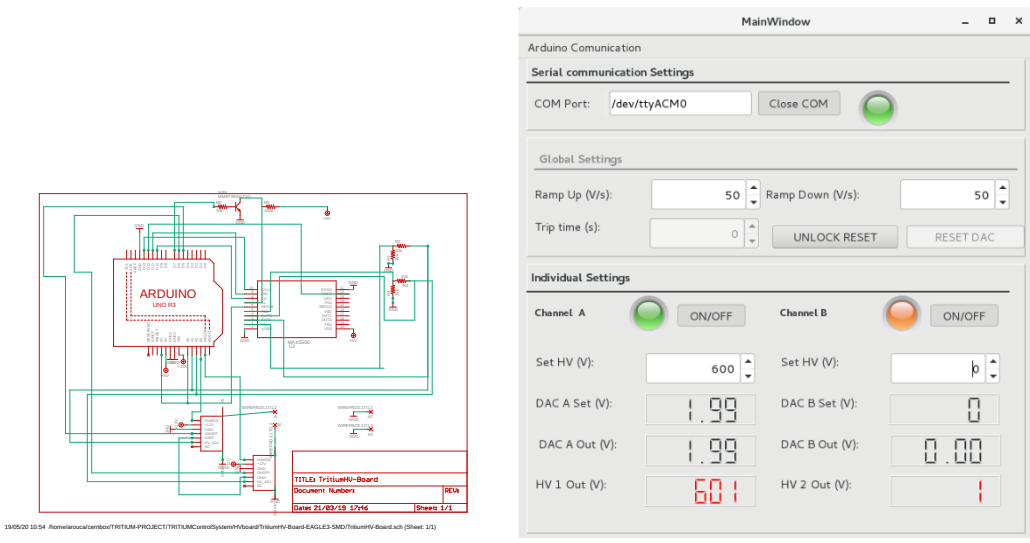
On the other hand, a electronical chain consisting of several PCBs was used to process and analyze the system signals, whose simplified electronic scheme is shown in Figure 5.11.

It consists of three different lines, two of them are used for the PMT signals of the prototype and the remaining line is used for doing anticoincidence with a active veto.

To test this electronic chain a plastic scintillation with dimensions of  $10 \cdot 10 \cdot 1 \text{ cm}^3$  was used to simulate a veto signal but four different vetos are being developed, each one is based on a rectangular plastic scintillations of Saint-Gobain company [134], whose dimensions are  $50 \text{ cm} \cdot 30 \cdot 2 \text{ cm}^3$  with

---

<sup>2</sup>DAC, Digital-to-analog converter



(a) Electronic scheme of the PCB

(b) Graphical user interface

**Figura 5.10** – Electronic scheme of the PCB designed to power the PMTs of Aveiro prototype and the graphical user interface developed to control it.

a PMT coupled, model R2154-02 2" from Hamamatsu company [131]. The output signal of these PMTs will be input in a OR stage, whose response will be introduced in the veto line shown previously in Figure 5.11. As a result, each plastic scintillator will be read in anticoincidence with tritium-Aveiro prototype.

Both lines, used to process and analyze the PMT signals of the prototype, are equal and they are used to operate in time coincidence. First, each PMT signal is introduced in a preamplifier model CR111 from CRE-MAT Inc. company [135], which is used to shape and pre-amplify the signal. To reduce electronic noise and signal loss, both preamplifiers are connected as close as possible to the PMTs and they are located inside of aluminum boxes which act like a Faraday cage.

Each preamplifier is followed by a differentiation stage, which is used to reduce the time width of the signal, and amplification stages, used

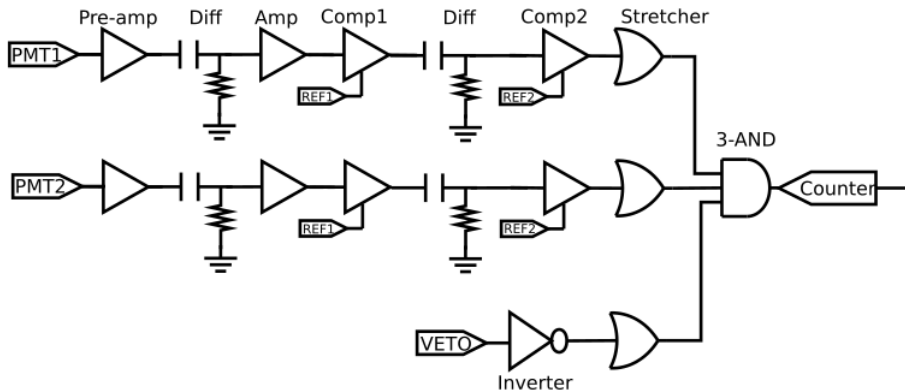


**Figura 5.11** – Simplified electronic scheme used to process and analyze the signal of Tritium-Aveiro 0 prototype.

to amplify the signal. The amplification used is the model OPA656 from Texas Instruments [136].

Then, a fast comparator, model LT111 from Linear Technology company [137], is used to set a threshold which will be used to remove the PMT signals whose amplitude are below this value (dark counts of the PMT). A MAX5500 DAC is used to configure the thresholds.

The time width of the preamplifier output signal is too large,  $200\ \mu s$ , so which too many false coincidence will be registered. To solve this problem a second differentiation stage is included and a second comparator are added to produce a 5V square signal again.

Finally a tunable pulse stretcher based on an OR gate, model SN74AHC1 from Texas Instruments company [138], is used to set the time width of each signal at 100 ns, with which the time coincidence windows of our acquisition system is 200 ns, narrow enough to have a negligible false coincidence rate.

In the remaining line, used for the veto signal, an inverter is used

in the first stage. With it, the signal will always be in the high level, 5 V, except when a cosmic particle is detected, in which case the signal will be in the low level, 0 V. Then, another stretcher is used to create a signal with the same time width than the others, 100 ns.

Lastly, these three signals are introduced into a 3-input AND gate, model SN74LVC1G11 from Texas Instruments company [139], to perform a logic level comparison. With this last stage we achieve a temporal coincidence of both PMT signals of the prototype and anti-coincidence of them with the veto signal. The output signal of this last stage is simply connected to a pulse counter.

A GPIO pins of a Raspberry Pi is used to communication with the system, control it and configure the different threshold levels and a graphical user interface, whose appearance is shown in Figure 5.12, has been developed to manage in a comfortable way the counter system.

In addition to count, which is the option normally used in our detector, this electronic system include a voltage follower circuit connected to the preamplifier output signal which can be used to obtain a energy spectrum of each PMT of the prototype.

It is important to note that, although this system has a graphical user interface that allows comfortable control of the system, the usual way in which it is controlled is remotely through the computer terminal.

In Figure 5.13 two screenshots are shown to demostrate two different situations of this system. There, we have four different signals. The yellow and cyan signal are input signals of the AND-Gate, which come from the PMT signals of the prototype. The pink signal is the third remaining input signal of the AND-Gate, which come from the PMT signal of the veto. The last signal, green, is the output signal of the AND-Gate.

As can be seen, in Figure 5.13a both PMTs of the prototype have

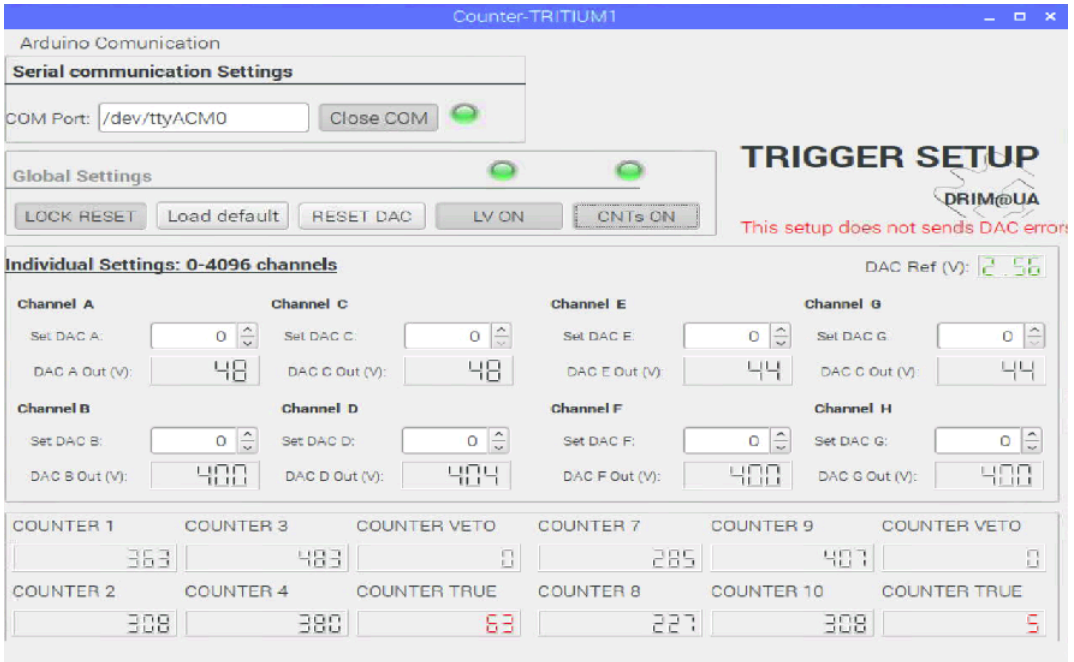


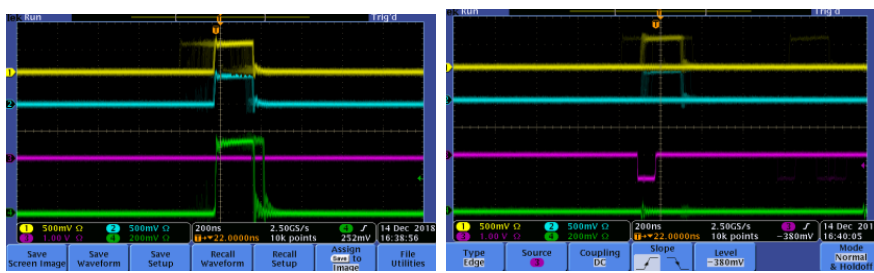
**Figura 5.12** – Graphical user interface used to manage the counter system.

detect a time coincident event, which has not been detected for the veto, so this event is counted. In Figure 5.13b, a time coincidence event has been observed in the three PMTs, which means that it is a cosmic event, so this event is not counted.

First some measurements were taken in the laboratory that were used to characterize the detector. For this task it was filled with ultra-pure water, which was used to measure the background of the detector, and then, it was filled with several radioactive liquid tritium solutions with different activities, 10 kBq/L and 30 kBq/L, which were used to measure the efficiency and the sensitivity of this module.

Later, it was installed in the arrocampo dam to test its functionality and to begin with the tritium level monitoring.

All these measurements will be shown in section 7.2.3, where it



(a) Event accepted by the electronic system  
 (b) Event rejected by the electronic system

**Figura 5.13** – Two different situations of the electronic chain response. A.- Event accepted since veto has not detected it. B.- Event rejected since veto has detected it

will be discussed and compared with the measurements of the previous prototypes.

### 5.3.2 Advanced IFIC prototype, Tritium-IFIC 2

The last prototype developed in TRITIUM experiment and the second thought to be the final versión of the Tritium detector module was Tritium-IFIC 2, which is shown in Figure 5.14, A.

This prototype was designed and built in the IFIC workshop and it consists of a cylindrical teflon vessel, shown in Figure 5.15, whose shape is similar to the one used in Tritium-Aveiro 0 prototype, whose internal length and diameter are 200 mm and 36 mm respectively.

This prototype contains 800 no-clad scintillating fibers, model BCF-12, with a length of 200 mm. We can check that, as we have said, many more fibers are used than the Tritium-Aveiro 0 prototype which are arranged in less volume.

The fibers used are cut, polished and cleaned with the conditioning

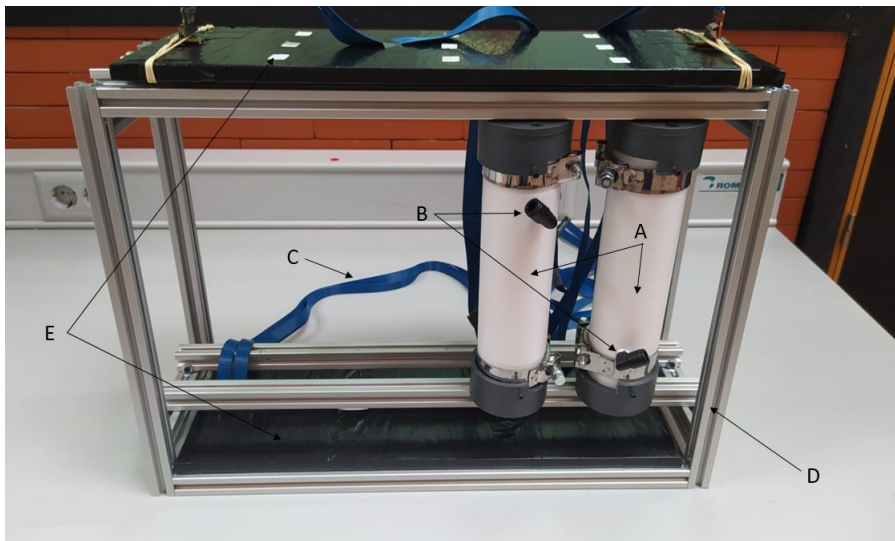


**Figura 5.14** – Tritium-IFIC 2 prototype.

processes previously shown in section 4.2 since, at that time, the development of the automatic polishing machine had been completed.

These fibers are freely arranged, with a density that allows water to flow through the fibers and two PMMA windows located at the ends of the fiber bundle were used to read this system, similar to the Tritium-Aveiro 0 prototype.

The width of the PMMA optical windows used is 5 mm, which is sufficient to guarantee radiosecurity since we are working at very low water pressure and two clamps are used to ensure the watertightness of the prototype, similar to the Tritium-Aveiro 0 prototype. We have checked that the transmission coefficient, shown in Figure 5.9, is not affected by the little difference of the PMMA width used in both prototypes.

As can be seen in Figure 5.14, B, and Figure 5.15, a water inlet/outlet was installed in the teflon vessel of this prototype to allow a constant water flux through the prototype, similar to the Tritium-Aveiro 0



**Figura 5.15** – Tritium-IFIC 2 teflon vessel.

prototype.

For the first laboratory measurements, two PMTs were used, model R8520-460 from the Hamamatsu Photonics company [83], which is useful to understand the results and compare them with the results obtained with the previous prototypes. However, measurements with SiPM arrays have already started whose output signal is connected to PETSYS system through flat wires as can be seen in Figure 5.14, C.

We have to take into account that our final objective will be to install this prototype in Arrocampo dam using SiPM arrays readout by the PETSYS system. This is the reason why we have not developed a electronics chain to process and analyze the PMT signals of this prototype.

Like the Tritium-Aveiro 0 prototype, although PETSYS has a graphical user interface, shown in Figure 5.16, which allows controlling all

the different options such as the voltage with which we feed the SiPM arrays, the thresholds used, etc., normally it will be controlled remotely via computer terminal.

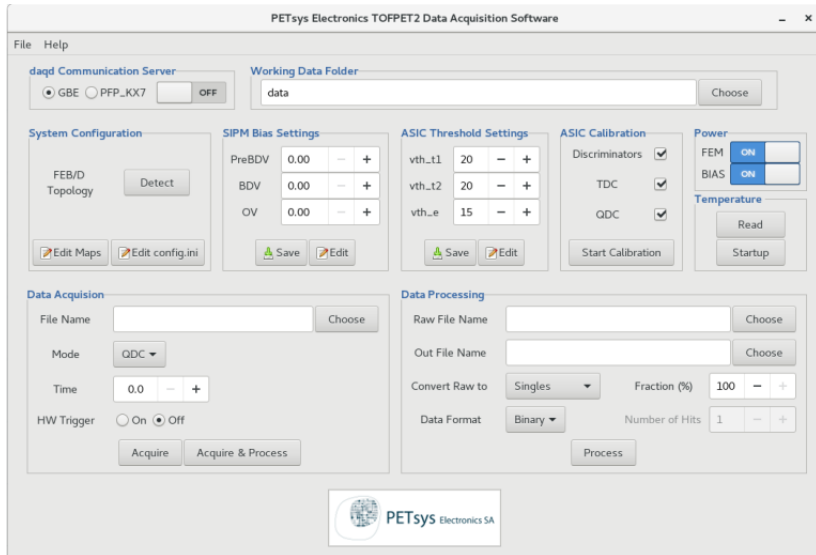


**Figura 5.16** – Graphical User Interface (GUI) of PETSYS.

Two PVC caps, located at both ends of the prototype, Figure 5.15b, were used to work with the SiPMs in a light-tight environment and an aluminum structure, shown in Figure 5.14, was designed and built to house up to 10 tritium-IFIC 2 modules and two cosmic vetos, shown in Figure 5.14, E.

At this point we should note that, in the available space of the lead shielding, explained in section 3.4.1, we can accommodate up to 5 structures like the one shown in Figure 5.14. It means that our final Tritium detector is prepared to have up to 50 Tritium-IFIC 2 modules and 10 different cosmic vetos. It means that, due to the reason that our detector scales with the number of tritium modules used, the results obtained with the tritium detector can improve the results obtained with the tritium-ific 2 prototype by a factor of 50.

Two identical Tritium-IFIC 2 prototypes were built and, similar to the Tritium-IFIC 0 prototype, one of them was filled with ultrapure water and used to measure the background and the other was filled with a radioactive liquid source of tritium and used to measure the signal. The volume used in both cases was 82 mL.

The activity of the tritium source used for this prototype is 10 kBq/L (uncertainty of 2.24%), which was prepared by diluting a sample of tritiated water explained in appendix E with ultrapure water until the desired activity was achieved.

The results of this prototype is shown in section 7.2.4, where they will be compared with the results of the previous prototypes and, specially, with Tritium-Aveiro 0 prototype to choose the design with the best results.

## 5.4 Modular TRITIUM Detector for In-Situ Tritium Monitoring

Lastly, this section presents the final Tritium detector, a schematic design of which is shown in Figure 5.17.

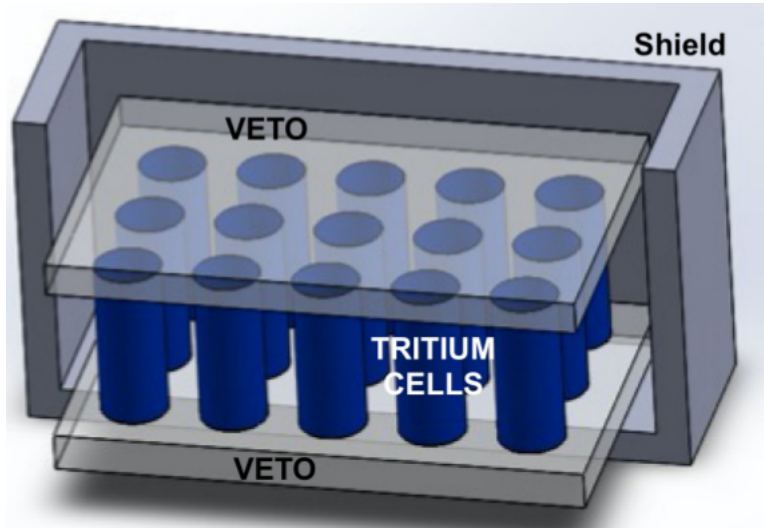


**Figura 5.17** – A schematic design of the Tritium detector.

It consists of several Tritium modules, shown in Figure 5.17, which will be read in parallel. Each module will be the prototypes that achieves better results, Tritium-Aveiro 0 (section 5.3.1) or Tritium-IFIC 2 (section 5.3.2).

These modules will be isolated from environmental radioactivity using three different techniques.

1. First, an external lead shielding, a part of which is shown in Figure 5.17, is used to stop the radioactivity coming from the place where the tritium monitor will be located before it reaches the tritium detector. It has been explained in section 3.4.1.

2. Second, several active vetos, shown in Figure 5.17, placed below and above the tritium modules, will be read in anticoincidence to eliminate the effect on the tritium measurement that has the highest energy events, mainly cosmic events, that will cross through the lead shielding and they reach the tritium modules. They have been explained in section 3.4.2 and 4.5
3. Finally, the radioactive elements present in the water samples, which will be introduced into tritium modules for their measurement, will be eliminated using an ultrapure water system, shown in section 3.3 and appendix D.

The ultrapure water system, lead shielding and a Tritium-Aveiro 0 prototype are installed and currently in operation at the Arrocampo dam. This entire system has been used to successfully monitor the tritium levels of the water used by the Arrocampo nuclear power plant during X months.

Furthermore, two Tritium-Aveiro 0 prototypes and four active vetos are currently under manufacturing to be installed at the Arrocampo dam, which will be measured in parallel with the current prototype installed.

It should be noted that RaspberryPi, which is used to manage the counter electronic system of Tritium-Aveiro prototype, will have some counting limitations if multiple modules are used. To overcome this problem, it must be replaced with an FPGA-based counter board to ensure reliable counting.

At the same time, three Tritium-IFIC 2 prototypes and an active veto have already been built, and their installation at the Arrocampo dam has been delayed due to various restrictions imposed in Spain due to the global coronavirus pandemic. They will be installed as soon as possible.

One of the most important points of the Tritium detector is its modular design, with which we can achieve scalability to reach the required

sensitivity, 100 Bq/L.

If this sensitivity goal is not reached with the current three modules, which will be installed soon, we only need to install some additional modules to improve it.

As we have said before, our only restriction is the available space, which is fixed by the lead shield already built and installed (it is also fixed by the available space in the house where the lead shield is installed). If it is necessary, the lead shielding and the house can be modified to enlarge the available space but is not currently under consideration.

Taking into account the currently available space, five different structures designed for Tritium-IFIC 2, one of which is shown in Figure 5.18, can be used, where ten different modules (grey) and an active veto (black) can be accommodated in any of them.

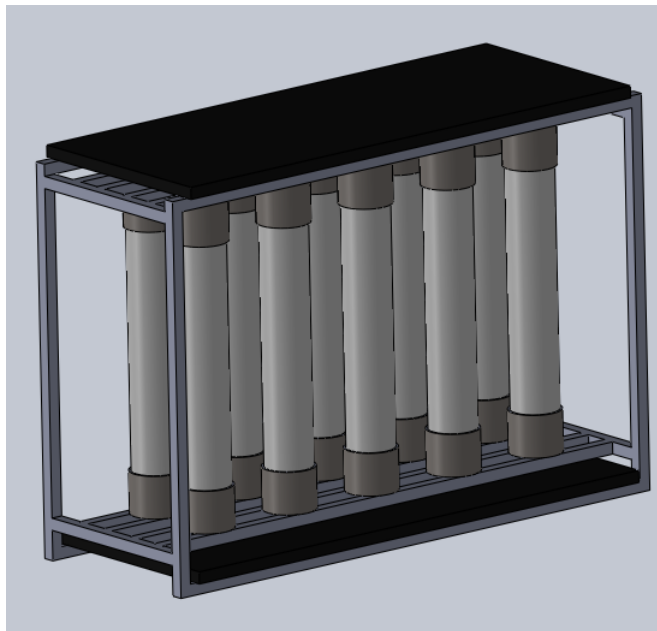


**Figura 5.18** – A tritium detector design based on the Tritium-IFIC 2 prototype.

It means that up to 50 Tritium-IFIC 2 modules can be used in parallel, reducing the Tritium detector sensitivity by a factor of fifty. In light of the results, it is not expected to use more than one structure like the one shown in Figure 5.18 (ten modules) to reach the target sensitivity.

# Chapter 6

## Simulations

### 6.1 Introduction

This chapter shows the Monte Carlo simulations that have been performed to choose the best design for our detector and understand its behavior. For this task, the used simulation environment is Geant4 [140, 141].

## 6.2 Geant4 Environment

Geant4 is a software toolkit for the simulation of the passage of particles through matter. It is a package developed at CERN that is based on object-oriented technology that has been implemented in the C ++ programming language.

It includes the definition of all the different aspects of the simulation process such as detector geometry, materials used, particles of interest, physics processes that handle particle and matter interactions, response of sensitive detectors, generation, storage and analysis of event data and visualization.

Geant4 simulates particle-by-particle physics. It means that, in our case, the tritium events will be initialized one by one, whose energy, moment, position, etc. will be determined. Then, the propagation and interaction of each tritium event with the scintillator will be simulated, in which optical photons will be created. The propagation of these optical photons will also be simulated one by one and the simulation will end when all tritium events have been simulated and the optical photons created have been absorbed by either the sensitive detector or other materials present in the simulation.

A physics list used for these simulations was Livermore, G4EmLivermorePhysics, which is specially designed to work with low energy particles. This list includes the most important electromagnetic process at low energies such as Bremsstrahlung, Coulomb scattering, atomic de-excitation (fluorescence) and other related effects.

The materials used in these simulations were water (to simulate the tritium solution), PMMA (to simulate the optical windows of the prototype), polystyrene (to simulate the core of scintillating fibers), teflon (to simulate the prototype vessel), silicone (to simulate the optical grease), sil-

icate glass (to simulate the optical windows of the PMTs) and bialkali (to simulate the photocatode material of the PMT).

The properties of water, teflon, polystyrene were taken from the Geant4 NIST database and the other materials were built by specifying their atoms. Optical properties was added to these materials:

1. First, the energy spectrums of refractive index and light attenuation was added to the water which was obtained from the reference [144]. Also a electrons emission, uniformly distributed in the water volume, was added to the water whose energy was calculated using the tritium energy spectrum. The used data was obtained from the reference [145].
2. Second, the energy spectrums of refractive index, light attenuation and photon emission was added to the polystyrene, which was obtained from their data sheet [78]. Also the scintillation yield and the decay time was included.
3. Third, the quantum efficiency spectrum was included to the photocatode material of the PMT, whose data was obtained from its data sheet [83] and a refraction index of 1.46 was used for the optical grease.
4. Finally, the optical data for the remaning materials, PMMA windows, teflon and silicate glass, were taken from the reference [146].

It is important to note that this chapter is focused on the Tritium-IFIC 2 prototype since these were the simulations I was primarily working on, but a similar simulation has been performed for the Tritium-Aveiro prototype with which important results has been obtained which will be shown in the section 7.4. In addition, other smaller simulations will be shown, such as a single scintillating fiber with various lengths or various diameters with which the effect of these parameters was quantified.

## 6.3 Description of the Simulations Performed

Several simulations have been designed and run during the life of the TRI-TIUM project to quantify how different values of interesting parameters affect to the tritium measurement and to understand the behaviour of the different Tritium prototype built which are shown in the following sections.

### 6.3.1 Tritium Source Shape Optimization

First of all the shape of the simulated tritium source was tested. The objective of this study was to find the tritium source shape that optimaze the simulation.

Due to the reason that the mean free path of tritium decay in water is only around  $5 \mu\text{m}$ , there will be many tritium events from the tritium solution that won't reach the scintillating fibers. These will be tritium events that don't provide us with useful information and only contribute to being time consuming and reducing available computing resources.

To optimize the simulation, we found the shape of the tritium source that minimizes the tritium events that do not reach the scintillating fibers avoiding losing the tritium events that reach them.

The simulation that has been designed designed for this test consists of a scintillating fiber with a length of 20 cm and a diameter of 2 mm and a surrounding tritiated water source with the same length and a thickness 100 times greater than the mean free path of tritium electrons, that's 0.5 mm, to ensure that this study take into account all possible tritium electrons that can reach to the scintillating fiber.

We have to keep in mind that the dimensions of the fiber are not important in this study since we have only simulated energy deposition of

tritium events in the fiber. That is, we have not simulated the following steps such as photon generation, propagation of these photons, etc. where the shape of the scintillating fiber becomes important.

The results of this simulation are shown in section 7.4, where it will be discussed.

### 6.3.2 Fiber Length Optimization

Another test was performed to find the fiber length which optimizes the tritium detection efficiency. Two different lengths of the scintillating fiber were taken into account in this study, 1 m and 25 cm.

For this task, the Tritium-Aveiro prototype was simulated. It consists of 360 scintillating fibers readout by two photosensors, located at both ends, which consist on a windows glass and photocatode. These scintillating fibers are located inside of a teflon tube with two PMMA windows and a optical grease layer with a thickness of 0.5 mm were simulated between the PMMA windows of the prototype and the photosensors. All optical properties mentioned in section 6.2 were included in this study.

The results of this study are shown in section 7.4 where they will be discussed.

### 6.3.3 Fiber Diameter Effect

A third test was carried out to check the effect of the fiber diameter in the tritium measurement. For this test, the same simulation explained in section 6.3.2 was used, where a fiber length of 20 cm was chosen. Two different diameters were taken into account in this study, 1 mm and 2 mm, which are the commercial options given by Saint-Gobain company.

It doesn't have sense to test it with the tritium source since its efficiency will scale with the active surface<sup>1</sup> of the scintillating fiber. However, an interesting study can be performed to check how the fiber diameter affect to the cosmic detection in the fiber. It is an important result as the background-signal ratio is mainly affected by the cosmic events that hit the Tritium detector.

To do so, the CRY library<sup>2</sup> [142], [143] was used to generate this cosmic events, which replaced the tritiated water source used in the previous simulation. The CRY library is able to generate cosmic-ray shower distributions for different particles (muons, neutrons, protons, electrons, photons and pions) at several heights (see level in our case).

The cosmic sources shape used in this simulation is a square of  $1 \cdot 1 \text{ m}^2$  located at a height of 35 cm.

The result of this simulation will be shown in section 7.4, where it will be discussed.

### 6.3.4 Simulation of the Tritium-IFIC 2 Prototype

The Tritium-IFIC 2 prototype simulation was the last simulation developed in the TRITIUM experiment and it was the one I mainly focused on. This simulation is similar to the previous simulation of the Tritium-Aveiro 0 prototype simulation since the design of both detectors are quite similar. There are two main difference between both simulated prototypes:

1. The diameter of the fibers used, which is 1 mm for Tritium-IFIC 2 prototype and 2 mm for Tritium-Aveiro 0 prototype. As we are filling

---

<sup>1</sup>The active surface of the scintillating fiber is the part of the surface of the scintillating fiber that is in contact with the tritiated water.

<sup>2</sup>CRY library, Cosmic-Ray Shower library

the internal volume of the teflon vessel, this difference imply a difference number of the used scintillating fibers, creating in a difference signal-background ratio.

2. The photosensors used since, although both are PMTs, the model of the used PMTs is different and it cause a different active area readout, affecting to the tritium detection efficiency.

The Tritium-IFIC 2 prototype simulation consists of 800 equispaced fibers distributed in sixteen different circles with increasing radius, which are shown in Figure 6.1. The fibers simulated has a diameter of 1 mm and the optical properties, mentioned in section 6.2, has been added to them, whose values has been obtained from the data sheet provided by the manufacturer.

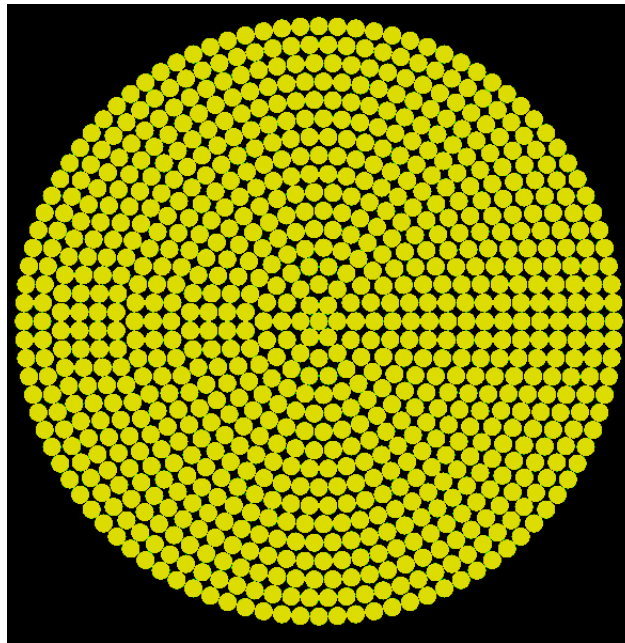


**Figura 6.1** – Distribution of the scintillating fibers in the simualtion of Tritium-IFIC 2 prototype.

The used tritiated water source consists of a tritiated water volume

with a thickness of  $5 \mu\text{m}$  around each scintillating fiber. The Tritium events will be uniformly distributed in all the tritiated water volume.

These scintillator fibers are located inside of a teflon vessel, which was simulated with the dimensions mentioned in section 5.3.2. Two PMMA windows with a thickness of 5 mm were simulated and located in both fiber ends and a optical grease layer with a thickness of 0.5 mm was included in each PMMA windows.

Finally, two PMTs, model R8520-460 from Hamamatsu company [83], were simulated in both ends. The data for the dimensions of them and their quantum efficiency spectrum were obtained from the data sheet provided by the manufacturer.

The optical properties used for the tritiated water, teflon vessel, PMMA windows and the optical grease are exactly the same as those used for the Tritium-Aveiro 0 prototype simulation.

This simulation is shown in Figure 6.2 in which can be appreciated the PMTs (black), the optical grease (blue), PMMA windows (white), tritiated water (green) and scintillating fibers (yellow). In this image, the Teflon container was not drawn to allow its interior to be seen and several volumes of tritiated water were also not included to allow several scintillation fibers to be seen.

As can be seen in this figure, the used PMTs don't cover the entire active area formed by the scintillating fiber bundle. It's not a problem for the Tritium detector since its final version will not include this photosensors. The final version of Tritium-IFIC 2 prototype will use SiPM arrays and the PMTs model used in the Tritium-Aveiro 0 prototype are circular PMTs with which the full active area is covered.

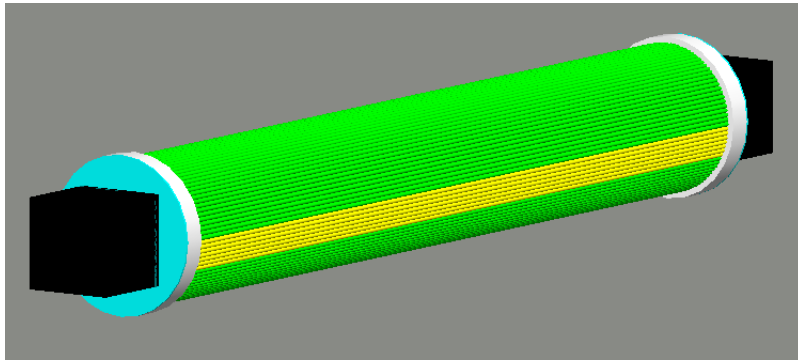


**Figura 6.2** – Simualtion of Tritium-IFIC 2 prototype. PMTs (black), the optical grease (blue), PMMA windows (white), tritiated water (green) and scintillating fibers (yellow)

### 6.3.5 Simulation of the Lead Shielding and Cosmic Veto

Finally the lead shielding and active vetos were included in the simulation of the Tritium-IFIC 2 prototype, explained in section 6.3.4. The objective of these simulations was to quantify their effect in reducing cosmic events detected by the prototype and to demonstrate their necessity.

For this task, similar to that done in section 6.3.3, the tritium source was not simulated. Instead of, a cosmic events source was used, which was simulated through the CRY library previously explained.

As can be seen in Figures 3.26a and 3.26b, two plastic scintillators were simulated with the dimensions exposed in section 3.4.2 and located above and below of the Tritium-IFIC 2 prototype simulated.

The optical properties given to this plastic scintillators were the same as the one used for the fibers, which are the refractive index and the light attenuation spectrum, whose values are the same that those used for the fibers, and energy emission spectrum, whose values was obtained from their data sheet provided by the manufacturer [111].

As shown in this figure, two PMTs, model R8520-460 from Hamamatsu company, were simulated to read each plastic scintillator, similar to that presented in section 3.4.2.

Finally, a lead shielding was simulated, whose properties were taken from the Geant4 NIST database. Due to the reason that only one Tritium detector module was simulated, it was not necessary to simulate its real dimensions since, in this case, we would need to simulate a larger cosmic veto source and most of this events will not reach neither our active veto nor our Tritium detector module, just contributing to being time consuming and reducing available computing resources.

Instead of that, the dimensions of the lead shielding were smaller to optimize the simulation since this change don't affect to the results. The dimensions used were 60 cm long, 60 cm wide, 70 cm high, which is the minimum needed to accomodate the active vetos and Tritium detector module inside. When it is compared to the dimensions mentioned in section 3.4.2, it can be noted that the length of this lead shielding is smaller than the real dimension, 148 cm.

The results of these simulation will be presented in section 7.4, where they will be discussed.

# Chapter 7

## TRITIUM Monitor Results and Discussion

### 7.1 Introduction

Comparar las cuentas que espero teóricamente con las obtenidas experimentalmente para tritium IFIC 2. Sale bastante bien.

Ajustar una curva landau a los resultados de cada espectro energético.

Tritium 0 -> Tritium y fuentes radiactivas.

Tritium 1-> Tritium y comparación con Tritium 0

Aveiro -> Calibración inicial, Medida y comparación con la simulación, Reducción de cuentas debida al plomo, figuras 8a y 8b del paper experimental de Carlos, estudio teórico del límite de curié, medida en aire y agua, medida con 10 kBq/L, extensión a mayores tiempos,

Tritium 2 -> Medida y comparación con 1 y 0 (y si se puede con Aveiro). Resultados de la tabla del punto 1.3 de la tesis donde comparo con otros experimentos similares, estabilización, extrapolación teórica.

Finally, the simulated and the experimental spectra are compared, yielding some conclusions regarding the PMT signal and the behavior of the scintillator in tritiated water.

## 7.2 Results from Laboratory measurements

Mostrar los resultados por unidad de centelleador (unidad de fibra o unidad de superficie) para poder comparar bien los prototipos.

Demostraciones teóricas de las cuentas esperadas en los detectores  
(en cada apartado)

### 7.2.1 Experimental Results of TRITIUM-IFIC 0 Prototype

### 7.2.2 Experimental Results of TRITIUM-IFIC 1 Prototype

### 7.2.3 Experimental Results of TRITIUM-Aveiro 0 prototype

- Espectro energético.

- Monitorización del fondo durante meses. Desde el mes 3 hasta el mes 8

- Monitorización del fondo y de una disolución de Tritio durante unos días. Estudio de las gaussianas de su distribución

- Efecto del apantallamiento del plomo.

- Volume used.

The first detector module was characterized, commissioned and installed in the discharge channel of Arrocampo dam to the Tagus river. Due to the high sensitivity of the detection module it requires radioactive background mitigation techniques through the use of active and passive shielding. We have obtained a Minimum Detectable Activity lower than 5 kBq/L for a single module being limited by the cosmic background. Far from the primary goal this value is already compatible with a real-time tritium environmental surveillance monitor and a power plant pre-alert system.

Medida con una fuente de  $^{55}\text{Fe}$ , ya que tiene gammas muy cercanas a las del tritio, 5.9keV. Esta se situó dentro del tubo de teflón ya que si no

se apantallaría y no llegaría ala fibra. Debido a esto no podíamos usar agua en su interior.

#### 7.2.4 Experimental Results of TRITIUM-IFIC 2 prototype

Una sección con la monitorización de la señal y el fondo.

Rellenar con uan actividad grande y volver a medir.

Vaciar el prototipo y llenar con actividades más pequeñas. 1000 y 100 Bq/L.

Espectro de tritio + fondo medido y sacar la significancia y la relación señal ruido y todo lo que se pueda.

Comparar fondos en el laboratorio, caceres, almaraz, etc.

COmparar cada propuesta (Aveiro valencia) -> Publicaciones de cada uno y una de las sintesis.

Medir en el prototipo con SIPM.

### **7.3 Results from Measurements at Arrocampo dam**

## 7.4 Results of the simulations

In this work we present simulation results for a modular tritium in-water real-time monitor. The system allows for scalability in order to achieve the required sensitivity. The modules are composed by 340 unclad scintillating fibers immersed in water and 2 photosensors in coincidence for light readout.

- Simulación del tritio. Vemos que solo se detecta tritio hasta 5 micras. Debido a esto solo simularemos aros de tritio de espesor X.

Vemos la necesidad de tener que utilizar fibras sin clad. También vemos que el espectro de deposición de energía esta centrado en 10 keVs ya que las emisiones de energía pequeña pocas veces llegan a la fibra.

Mostrar aquí la simulación del espectro de tritio. Si eso mostrarla superpuesta a la referencia 10 del paper de carlos (figura 2)

- Simulación del tamaño de las fibras. Vemos que es mejor fibras cortas

Este experimento a consistido en simular

- Simulación fibras de 1 mm y 2 mm. Cósmicos.

- Incluido el coeficiente de Birks ya que este afecta bastante. Mostrar como afecta.

Light yield and Birks' coefficient uncertainties for low energy beta particles is discussed.

A study of the detection efficiency according to the fiber length is presented.

Simulación de cosmisos. Vemos que el resultado es mejor en fibras

de 1 mm

- Expandimos esto a tritium ific 2. Empezar por todos los pasos que sigue la luz y demas y ver que todo se simula correctamente (similar a como se hace en el TFM). Luego mostrar los resultados.

Due to the low energetic beta emission from tritium a detection efficiency close to 3.3% was calculated for a single 2 mm round fiber.-> Para Tritium-Aveiro 0 prototype

- Añadimos el blindaje de plomo
- Añadimos los vetos activos
- Suma de ambos efectos.

Si pongo resultados de Tritium Aveiro genial, si no tengo que cambiar el último parrafo de la seccion Geant4 Environment.

# Chapter 8

## Conclusions and Prospects

Que cosas se han conseguido en este experimento? -> DECIR que tanto lo que se ha conseguido con el detector como con las investigaciones de componentes del detector (capítulo 3)

Responder a las grandes preguntas:

- Podemos medir tritio?
- Lo podemos hacer en tiempo quasi real?
- Lo podemos hacer a la actividad que queríamos?
- Que sensibilidad se ha llegado a conseguir?
- Estabilidad temporal?
- Precio?
- Comparación con respecto al resto de experimentos? -> Poner la tabla 1.8 pero incluyéndonos
- Efecto del shield

- Efecto de los vetos
- Efecto de ambas cosas
- Medidas a varias actividades

Hemos llegado a detectar 30 kBq/L con Tritium-Aveiro y se espera llegar a medir hasta menos de 5 kBq/L (superando los actuales límites).

Hemos llegado a detectar 10 kBq/L con Tritium-IFIC 2 (superando los actuales límites) y se espera llegar a medir incluso menos.

Ambos valores, lejos de ser el objetivo del proyecto, sirven para una monitorización en tiempo quasi real. Además, con el monitori final que consiste en varios modiules de estos en apralelo, se pretende llegar al objetivo deseado.

Tenemos datos de tritio en el agua bruta (agua del río) de esa zona desde 1998, pero tengo que solicitar permiso para poder dártelos. En cualquier caso, hay otra manera de conseguirlos, que es a partir de los informes del CSN al Congreso de los diputados (web CSN). Desde 2015 la concentración de tritio en el agua del río Tajo ha disminuido considerablemente porque la CNA instaló unos enfriadores por convección que emiten parte del H3 a la atmósfera. -> Tesis de Antonio Rodríguez y de Elena García.

# Appendices



# Appendix A

## Birks Coefficient Study

Aún faltan cosas por decir.



## Appendix B

# Signal Processing in NIM Modules

Y más cosas aún.



## Appendix C

# Electronical Schemes of PCBs Used for SiPM Characterization

Y más cosas aún.



## Appendix D

# Ultrapure Water System

In this appendix I show several photos of the ultrapure water system in the same order that the water flows through them.

First of all, the complete scheme of the ultrapure water system is shown in Figure D.1:

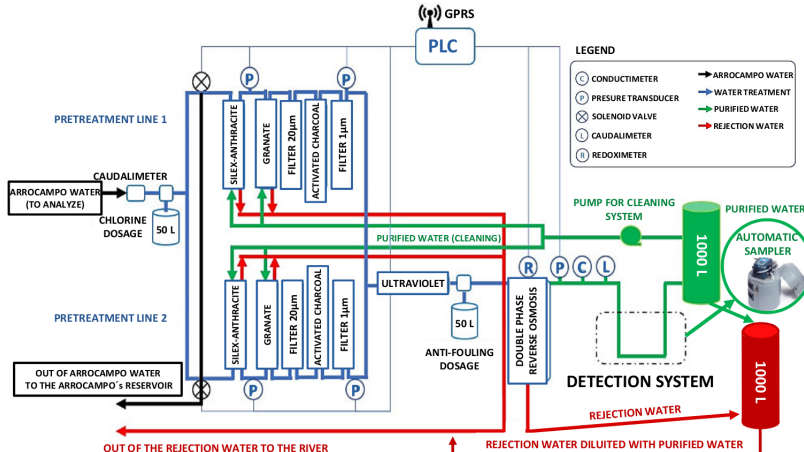


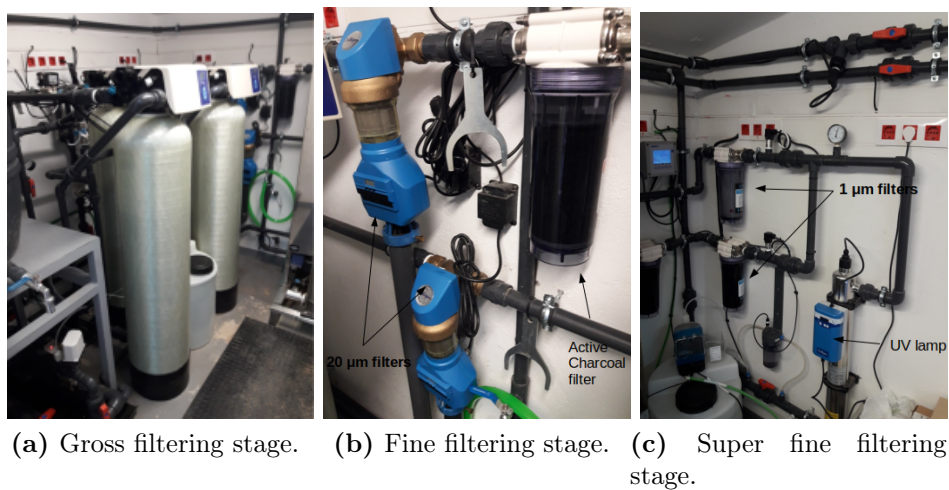
**Figura D.1** – Scheme of the ultrapure water system.

Secondly, the Gross filtering stage, made up of Silex-Antracite and

Granate filters, is shown in Figure D.2a:

In third place, the fine filtering stage, consisting of  $20\ \mu\text{m}$  filter and active carbon filter, is shown in Figure D.2b:

In fourth place, the superfine filtering, composed of the  $1\ \mu\text{m}$  filter and the UV lamps, is shown in Figure D.2c



(a) Gross filtering stage. (b) Fine filtering stage. (c) Super fine filtering stage.

**Figura D.2** – Different stages of filtration of the ultrapure water system.

In fifth place, the double phase reverse osmosis is shown in Figure D.3a

In sixth place, the containers in which we store the ultrapure water and the reject water after treatment is shown in Figure D.3b.

In seventh place, the Siemens PLC, software used to control the ultrapure water system, is shown in Figure D.4.

Finally, the complete system of the ultrapure water system is shown in Figure D.5

Just as a curiosity, the three types of water (raw water, rejection



(a) Doble phase reverse osmosis stage and (b) Storage containers of reject and ultrapure water.

**Figura D.3** – Doble phase reverse osmosis stage and containers used to store the outlet water of the ultrapure water system.

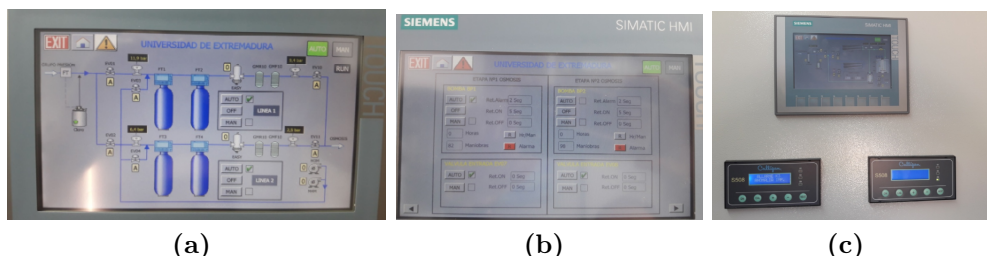


**Figura D.4** – Siemens PLC, software for remote control of ultrapure water system.



**Figura D.5** – General photo of the complete ultrapure water system.

water and ultrapure water) are shown in Figure D.6, where you can visually check the difference in the turbidity of each type of water.

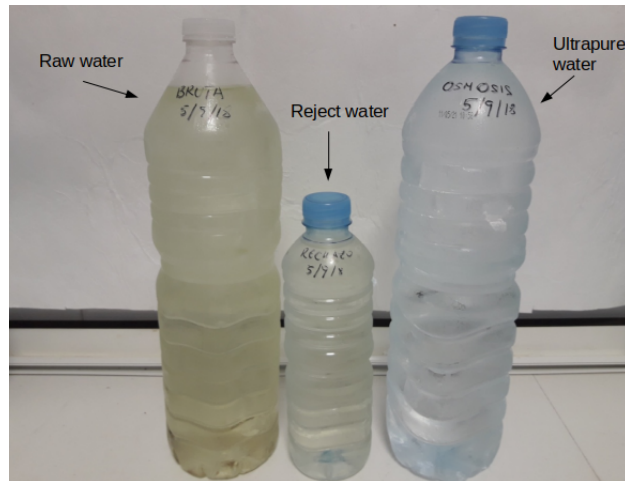


**Figura D.6** – Raw water, reject water and ultrapure water obtained with this system.

## Appendix E

# Preparation of Liquid Radioactive Source of Tritium

To prepare this radioactive liquid source, 1.86 g (uncertainty of 0.05%) of tritium was purchased from the Germany company PTB<sup>1</sup>, which has a serial number of 2005 – 1442 and reference number of PTB-6.11 – 285/03.2017 [129]

The activity of this tritium source is 26,8 MBq/g (uncertainty of 2.24%), reference data of 1 of January of 2017, and it was dissolved in 500 mL (uncertainty of 0.05%) of ultrapure water, giving 500 ml of tritium water, to which we will call standard solution, with an activity of 100.096 kBq/g (uncertainty of 2.24%), that's, 99.696 kBq/L (uncertainty of 2.24%), which was measured with the TRI-CARB 2810 system, based on liquid scintillation readout by PMT.

---

<sup>1</sup>Physikalisch-Technische Bundesanstalt, Braunschweig and Berlin, Germany

206APPENDIX E. PREPARATION OF LIQUID RADIOACTIVE SOURCE OF Tl

## Appendix F

### Electronic System of TRITIUM-Aveiro 0 prototype



# Bibliography

- [1] IAEA, *The International Atomic Energy Agency Webpage*.
- [2] UNSCEAR, *The United Nations Scientific Committee on the Effects of Atomic Radiation Webpage*.
- [3] CSN, *Consejo de Seguridad Nuclear, Spain Webpage*.
- [4] ICRU, *International Commission of Radiological Units and Measurements Webpage*.
- [5] ICRP, *International Commission on Radiological Protection Webpage*.
- [6] ISR, *International Society of Radiology Webpage*.
- [7] UN, *United Nations Webpage*.
- [8] CSN, *Red de Estaciones Automáticas, REA Webpage*.
- [9] CSN, *Red de Estaciones de Muestreo, REM Webpage*.
- [10] *Council directive 2013/15/euratom*.
- [11] J. W. BERTHOLD, L. A. JEFFERS, *Phase 1 Final Report for In-Situ Tritium Beta Detector*, U. S. Department of Energy, McDermott Technology, Inc., Research and Development Division, **DE-AC21-96MC33128**, April, 1998.

- [12] J. W. BERTHOLD, L. A. JEFFERS, *In Situ Tritium Beta Detector*, U. S. Department of Energy, McDermott Technology, Inc. (MTI), Technology development data sheet, **DE-AC21-96MC33128**, May, 1999.
- [13] X- HOU, *Tritium and  $^{14}C$  in the environmental and nuclear facilities: Sources and analytical methods*, Journal of the Nuclear Fuel Cycle and Waste Technology (JNFCWT), 16 (2018), 11-39 **DOI: 10.7733/jnfcwt.2018.16.1.11**.
- [14] REFERENCIAAAAAAAA.
- [15] *Avance del informe del sistema eléctrico español, 2019*, Red eléctrica española.
- [16] *China construirá 60 centrales nucleares en la próxima década*, Europa press.
- [17] *Inversión de EE. UU. de 35 millones para centrales nucleares*, Energy News
- [18] *Three mile island accident*, World Nuclear Association.
- [19] *International Energy Outlook 2013*. U. E. Energy Information Administration.
- [20] Tritium at Fermilab.
- [21] **Brookhaven National Laboratory (BNL)**.
- [22] ALEKSANDRA SAWODNI, ANNA PAZDUR, JACEK PAWLÝTA, *Measurements of Tritium Radioactivity in Surface Water on the Upper Silesia Region*, Journal on Methods and Applications of Absolute Chronology, Geochronometria, Vol. 18, pp 23-28 **2000**.
- [23] M. L. OLIPHANT, P. HARTECK and E. RUTHERFORD, *Transmutation Effects observed with Heavy Hydrogen*, Nature, 133, 413 (1934)**DOI: 10.1038/133413a0**.

- [24] LUIS W. ALVAREZ and R. CORNOG, *Helium and Hydrogen of Mass 3*, Physical Review Journals Archive, 56, 613 (1939) DOI: [10.1103/PhysRev.56.613](https://doi.org/10.1103/PhysRev.56.613).
- [25] *DOE Handbook: Primer on Tritium Safe Handling Practices*, U. S. Departament Of Energy Washington, D.C. 20585.
- [26] ROBERT HAIGHT, JOSEPH WERMER and MICHAEL FIKANI, *Tritium Production by Fast Neutrons on Oxygen: An Integral Experiment*, Journal of Nuclear Science and Technology, 39:sup2, 1232-1235, DOI: [10.1080/00223131.2002.10875326](https://doi.org/10.1080/00223131.2002.10875326).
- [27] INSTITUT DE RADIOPROTECTION ET DE SURETÉ NUCLÉAIRE *Tritium and the environment, Tritium and the environment*, IRSN, Enhancing nuclear safety.
- [28] , REFERENCIAAAA,
- [29] *International Atomic Energy Agency*.
- [30] *Tritium decay image*.
- [31] ZHANG LIN, *Simulation and Optimization Design of SiC-Basaed PN Betavoltaic Microbattery Using Tritium Source*, MDPI Open Access Journal 12/02/2020, DOI:[10.3390/cryst10020105](https://doi.org/10.3390/cryst10020105)
- [32] BLAUVELT, R.K., DEATON, M.R. and GILL, J.T., *Health Physics Manual of Good Practices for Tritium Facilities*, EG and G Mound Applied Technologies, Miamisburg, OH (United States), Technical Report, 01 December 1991, DOI: [10.2172/266889](https://doi.org/10.2172/266889).
- [33] TSUYOSHI MASUDA and TOSHITADA YOSHIOKA, *Estimation of radiation dose from ingested tritium in humans by administration of deuterium-labelled compounds and food*, Scientific reports, 02 February 2021, DOI: [10.1038/s41598-021-82460-5](https://doi.org/10.1038/s41598-021-82460-5).

- [34] Z. PIETRZAK-FLIS, I. RADWAN, Z. MAJOR and M. KOWALSKA, *Tritium Incorporation in Rats Chronically Exposed to Tritiated Food or Tritiated Water for Three Successive Generations*, Journal of Radiation Research, Vol 22, Issue 4, December 1981, page 434-442 DOI: [10.1269/jrr.22.434](https://doi.org/10.1269/jrr.22.434).
- [35] J.R. MARTIN and J.J. KORANDA, *Biological Half-Life Studies of Tritium in Chronically Exposed Knagaroo Rats*, Journal of Radiation Research, Vol 50, Issue 2, May 1972, page 426-440 PMID: **5025235**.
- [36] T STRAUME and A. L. CARSTEN, *Tritium radiobiology and relative biological effectiveness*, Health Physics, Vol. 65, Number 6, December 1993, DOI: [10.1097/00004032-199312000-00005](https://doi.org/10.1097/00004032-199312000-00005) .
- [37] RYTOEMAA, T., SALTEVO, J. and TOIVONEN, H., *Radiotoxicity of Tritium-Labelled Molecules*, International Atomic Energy Agency symposium, IAEA, Vienna: Biological Implications of Radionuclides Released from Nuclear Industries, INIS Vol. 11, INIS Issue. 13, Reference Number, 11535484, 1979.
- [38] INTERNATIONAL COMMISSION ON RADIOLOGICAL PROTECTION, ICRP, *Recommendations of the ICRP. Annals of the ICRP, 21(1.3), 1991a. 1990. Oxford, Pergamon Press (Publication 60)..*
- [39] WORLD HEALTH ORGANIZATION, WHO, *Guidelines for Drinking-Water Quality. Vol 1. Third Edition. Geneve, Switzerland, 2004.*
- [40] INTERNATIONAL COMMISSION ON RADIOLOGICAL PROTECTION, ICRP, *Age-dependent doses to members of the public from intake of radionuclides: Part 5. Compilation of ingestion and inhalation dose coefficients. Oxford, Pergamon Press (International Commission on Radiological Protection Publication 72), 1996.*
- [41] DÉPARTEMENT FÉDÉRAL DE L'INTÉRIEUR, DFI (FEDERAL DEPARTMENT OF THE INTERIOR), *Ordonnance du DFI sur les sub-*

*stances étrangères et les composants dans les denrées alimentaires (817.021.23)*, 2006, Switzerland (in French).

- [42] ONTARIO MINISTRY OF THE ENVIRONMENT, *Ontario Drinking Water Objectives*. Toronto, Ontario, 1994.
- [43] QUÉBEC, *Résultats du programme de surveillance de l'environnement du site de Gentilly. Rapport annuel 2006*. Québec, Canada..
- [44] RUSSIA, *NRB-99 Radiation Safety Norms*, 2007.
- [45] AUSTRALIAN GOVERNMENT, NATIONAL HEALTH AND MEDICAL RESERCH COUNCIL and NATURAL RESOURCE MANAGEMENT MINISTERIAL COUNCIL, *AustralianDrinking Water Guideilnes 6*, National Water Quality Managment Strategy, Version 3.6, Updated March 2011.
- [46] NUCLEAR ENERGY AGENCY, NEA, *Radiation and Nuclear Safety Authority*, 1993. Radioactivity of Household Water. ST 12.3. Erweko Paintuote, Helsinki, Finland, 1994.
- [47] OFFICE OF ENVIRONMENTAL HEALTH HAZARD ASSESSMENT, OEHHA, *Public Health Goals for Chemicals in Drinking Water-Tritium*. OEHHA, California ENfironmental Protection Agency, California USA, September, 2007.
- [48] UNITED STATES ENVIRONMENTAL PROTECTION AGENCY, US EPA, *Drinking Water Requirements for States and Public Water Systems*, Radionuclides Rule, 1976.
- [49] INSTITUT DE RADIOPROTECTION ET DE SÛRETÉ NUCLÉAIRE, IRSN (RADIOPROTECTION AND NUCELAR SAFETY INSTITUTE), *Bilan de l'état radiologique de l'environnement français de 2015 à 2017*. France.

- [50] BUNDESAMT FÜR STRAHLENSCHUTZ, BMU (FEDERAL OFFICE FOR RADIATION PROTECTION), *Environmental Radioactivity and Radiation Exposure*, Annual Report, 2005, (Jahresbericht 2005). BMU, Bonn, Germany (in German).
- [51] CONSEJO DE SEGURIDAD NUCLEAR, CSN, NUCLEAR SAFETY COUNCIL, *National Regulation of Radionuclides*.
- [52] EUROPEAN ATOMIC ENERGY COMMUNITY, EURATOM, *Council directive 2013/15/euratom*, October, 2013. Laying down requirements for the protection of the health of the general public with regard to radioactive substances in water intended for human consumption.
- [53] , , and , , , ,
- [54] M. N. AL-HADDAD, A. H. FAYOUMI and F. A. ABU-JARAD, *Calibration of a liquid scintillation counter to assess tritium levels in various samples*, Nuclear Instruments and Methods in Physics Research A, Volume 438, Issues 2-3, December 1999, Pages 356-361, DOI: [10.1016/S0168-9002\(99\)00272-7](https://doi.org/10.1016/S0168-9002(99)00272-7).
- [55] K. J. HOFSTETTER and H. T. WILSON, *Aqueous Effluent Tritium Monitor Development*, Fusion Technology, Volume 21, 2P2, Pages 446-451, March 1992, DOI: [10.13182/FST92-A29786](https://doi.org/10.13182/FST92-A29786).
- [56] M. PALOMO. A. PEÑALVER, C. AGUILAR and F. BORRULL, *Tritium activity levels in environmental water samples from different origins*, Applied Radiation and Isotopes, Volume 65, Issue 9, September 2007, Pages 1048-1056, DOI: [10.1016/j.apradiso.2007.03.013](https://doi.org/10.1016/j.apradiso.2007.03.013).
- [57] R. A. SIGG, J. E. McCARTY, R. R. LIVINGSTON and M. A. SANDERS, *Real-time aqueous tritium monitor using liquid scintillation counting*, FNuclear Instrument and Methods in Physics Research A, Volume 353, Issues 1-3, 30 Decembre 1994, Pages 494-498 DOI: [10.1016/0168-9002\(94\)91707-8](https://doi.org/10.1016/0168-9002(94)91707-8).

- [58] N. P. KHERANI, *An alternative approach to tritium-in-water monitoring*, Nuclear and Methods in Physics Research A, Volume 484, Issues 1-3, 21 May 2002, Pages 650-659 DOI: [10.1016/S0168-9002\(01\)02008-3](https://doi.org/10.1016/S0168-9002(01)02008-3)
- [59] Z. CHEN, S. PENG, D. MENG Y. HE and H. WANG, *Theoretical study of energy deposition in ionization chambers for tritium measurements*, Review of Scientific Instruments, 84, 103302, 2013, DOI: [10.1063/1.4825032](https://doi.org/10.1063/1.4825032).
- [60] C. G. ALECU, U. BESSERER, B. BORNSCHEIN, B. KLOPPE, Z. KÖLLÖ and J. WENDEL, *Reachable Accuracy and Precision for Tritium Measurements by Calorimetry at TLK*, Fusion Science and Technology, 60:3, 937-940, DOI: [10.13182/FST11-A12569](https://doi.org/10.13182/FST11-A12569).
- [61] A. BÜKKI-DEME, C. G. ALECU, B. KLOPPE and B. BORNSCHEIN, *First results with the upgraded TLK tritium calorimeter IGC-V0.5*, Fusion Engineering and Design, Volume 88, Issue 11, November 2013, Pages 2865-2869 DOI: [10.1016/j.fusengdes.2013.05.066](https://doi.org/10.1016/j.fusengdes.2013.05.066).
- [62] M. MATSUYAMA, Y. TORIKAI, M. HARA and K. WATANABE, *New Technique for non-destructive measurements of tritium in future fusion reactors*, IAEA Nuclear Fusion, Volume 47, Number 7, S464, June 2007, DOI: [10.1088/0029-5515/47/7/S09](https://doi.org/10.1088/0029-5515/47/7/S09).
- [63] M. MATSUYAMA, *Development of a new detection system for monitoring high-level tritiated water*, Fusion Engineering and Design, Volume 83, Issue 10-12, December 2008, Pages 1438-1441 DOI: [10.1016/j.fusengdes.2008.05.023](https://doi.org/10.1016/j.fusengdes.2008.05.023).
- [64] S. NIEMES, M. STURM, R. MICHLING and B. BORNSCHEIN, *High Level Tritiated Water Monitoring by Bremsstrahlung Counting Using a Silicon Dift Detector*, Fusion Science and Technology, 67:3, 507-510, 2015, DOI: [10.13182/FST14-T66](https://doi.org/10.13182/FST14-T66).

- [65] K. S. SHAH, P. GOTHSKAR, R. FARRELL and J. GORDON, *High Efficiency Detection of Tritium Using Silicon Avalanche Photodiodes*, IEEE Transactions on Nuclear Science, Volume 44, Issue 3, June 1997, DOI: [10.1109/23.603750](https://doi.org/10.1109/23.603750)
- [66] P. JEAN-BAPTISTE, E. FOURRÉ, A. DAPOIGNY, D. BAUMIER, N. BAGLAN and G. ALANIC, *<sup>3</sup>He mass spectrometry for very low-level measurement of organic tritium in environmental samples*, Journal of Environmental Radioactivity, Volume 101, Issue 2, February 2010, Pages 185-190, DOI: <https://doi.org/10.1016/j.jenvrad.2009.10.005>.
- [67] C. BRAY, A. PAILOUX and S. PLUMERI, *Tritiated water detection in the 2.17  $\mu\text{M}$  spectral region by cavity ring down spectroscopy*, Nuclear Instruments and Methods in Physics Research A, Volume 789, 21 July 2015, Pages 43-49, DOI: [10.1016/j.nima.2015.03.064](https://doi.org/10.1016/j.nima.2015.03.064).
- [68] M. MURAMATSU, A. KOYANO and N. TOKANUGA, *A Scintillation Probe for Continuous Monitoring of Tritiated Water*, Nuclear Instruments and Methods, Volume 54, Issue 2, October 1967, Page 325-326, DOI: [10.1016/0029-554X\(67\)90645-3](https://doi.org/10.1016/0029-554X(67)90645-3).
- [69] A. A. MOGHISSI, H. L. KELLEY, C. R. PHILLIPS and J. E. REGNIER, *A Tritium Monitor Based on Scintillation*, Nuclear Instruments and Methods, Volume 68, Issue 1, 1 February 1969, Page 159, DOI: [10.1016/0029-554X\(69\)90705-8](https://doi.org/10.1016/0029-554X(69)90705-8).
- [70] R. V. OSBORNE, *Detector for Tritium in Water*, Nuclear Instruments and Methods, Volume 77, Issue 1, 1 January 1970, Page 170-172, DOI: [10.1016/0029-554X\(70\)90596-3](https://doi.org/10.1016/0029-554X(70)90596-3).
- [71] A. N. SINGH, M. RATNAKARAN and K. G. VOHRA, *An Online Tritium-in-Water Monitor*, Nuclear Instruments and Methods, Volume 236, Issue 1, 1 May 1985, Page 159-164, DOI: [10.1016/0168-9002\(85\)90141-X](https://doi.org/10.1016/0168-9002(85)90141-X).

- [72] M. RATNAKARAN, R. M. REVETKAR, R. K. SAMANT and M. C. ABANI, *A Real-time Tritium-In-Water Monitor for Measurement Of Heavy Water Leak To The Secondary Coolant*, International congress of the International Radiation Protection Association, Volume 32, Issue 15, 14-19 May 2000, P-3a-197, Reference number: **32015986**
- [73] K. J. HOFSTETTER and H. T. WILSON, *Aqueous Effluent Tritium Monitor Development*, Fusion Technology, Volume 21, 2P2, 1992, Pages 446-451, **DOI: 10.13182/FST92-A29786**.
- [74] K. J. HOFSTETTER and H. T. WILSON, *Continuous Tritium Effluent Water Monitor at the Savannah River Site*, International conference on advances in liquid scintillation, Vienna (Austria), 14-18 September 1992.
- [75] *Tritium, Interreg Sudoe Program. Tritium website.*
- [76] GLENN F. KNOLL, *Radiation Detection and Measurement*, Third Edition, John Wiley and Sons, Inc. 1999.
- [77] WILLIAM R. LEO, *Techniques for Nuclear and Particle Physics Experiments: a how-to approach*, Second Revised Edition, Springer-Verlag Berlin Heidelberg GmbH, 1994. **DOI: 10.1007/978-3-642-57920-2**.
- [78] SAINT-GOBAIN CERAMICS AND PLASTICS, INC., *Scintillating Optical Fibers*, It's What's Inside that Counts, 2005-14. **Data sheet**.
- [79] , , .
- [80] *Plastic Scintillating Fibers*, Scintillating Fibers, Wavelength Shifting Fibers and Clear Fibers. **Data sheet**.
- [81] , , .
- [82] JAVIER PÉREZ PÉREZ, *Caracterización de los Fotomultiplicadores R8520-06SEL para NEXT*, 25-06-2010.

- [83] HAMAMATSU PHOTONICS K.K., *Photomultiplier tube R8520-406/R8520-506. Data sheet.*
- [84] DAVID LORCA GALINDO, *Tesis: SiPM based tracking for detector calibration in NEXT*, Departamento de física atómica, molecular y nuclear, Universidad de Valencia (UV), Valencia, Spain, 03/2015.
- [85] OSI OPTOELECTRONICS, *Characteristics and Applications.*
- [86] HAMAMATSU PHOTONICS K.K. SOLID STATE DIVISION, *MPPC Multi-Pixel Photon Counter S13360-6050. Data sheet.*
- [87] HAMAMATSU PHOTONICS K.K. SOLID STATE DIVISION, *MPPC Multi-Pixel Photon Counter S13360-6075. Data sheet.*
- [88] HAMAMATSU PHOTONICS K.K. SOLID STATE DIVISION, *MPPC Multi-Pixel Photon Counter S13361-6050. Data sheet.*
- [89] HAMAMATSU PHOTONICS K.K. SOLID STATE DIVISION, *MPPC Multi-Pixel Photon Counter S13361-3050. Data sheet.*
- [90] SENSL SENSE LIGHT, *Introduction to the SPM TECHNICAL NOTE*. February 2017 **Document**.
- [91] KEITHLEY, A GREATER MEASURE OF CONFIDENCE, *Model 6487 Picoammeter/voltage source, Manual reference. Data sheet.*
- [92] TENNELEC, *Model TC 952 High Voltage Supply, Manual reference. Data sheet.*
- [93] WENZEL ELECTRONIK, *Model N 1330-4 High Voltage Power Supply. Website.*
- [94] PHILIPS SCIENTIFIC, *Model 740 Quad Linear Fan-In/Out, Manual reference. Data sheet.*
- [95] ORTEC, *Model 9326 FastPreamplifier, Manual reference. Data sheet.*

- [96] ORTEC, *Model 575A Amplifier, Manual reference. Data sheet.*
- [97] ORTEC, *Model 671 Spectroscopy Amplifier, Manual reference. Data sheet.*
- [98] ORTEC, *Model CF8000 Octal Constant-Fraction Discriminator, Manual reference. Data sheet.*
- [99] CAEN, *Model 84, 4 channels discriminator. Website.*
- [100] LECROY, *Model 465 Coincidence Unit, Manual reference. Data sheet.*
- [101] ORTEC, *Model 416A Gate and Delay Generator, Manual reference. Data sheet.*
- [102] AMPTEK, *MCA8000D, Pocket MCA, Digital Multichannel Analyzer, Manual reference. Data sheet.*
- [103] PETsys Electronics. **Website.**
- [104] SAINT-GOBAIN CERAMICS AND PLASTICS, INC., *Optical fiber BCF-98, Manual reference. Manual reference.*
- [105] THORLABS, *LED430L - 430 nm LED with a Glass Lens, 8 mW, TO-18. Datasheet.*
- [106] PALL THEODÓRSSON, *Measurement of weak radioactivity*, World Scientific, 1996.
- [107] R D EVANS, *The Atomic Nucleus*, McGraw-Hill, Inc., 1996.
- [108] P.A. ZYLA ET AL., (*Particle Data Grup*), *PDG, Prog. Theor. Exp. Phys. 2020 no. 8, 083C01 (2020)*. **Website DOI:** [10.1093/ptep/ptaa104](https://doi.org/10.1093/ptep/ptaa104).

- [109] HIROYUKI SAGAWA & ITSUMASA URABE (2001), *Estimation of Absorbed Dose Rates in Air Based on Flux Densities of Cosmic Ray Muons and Electrons on the Ground Level in Japan*, Journal of Nuclear Science and Technology, 38:12, 1103-1108, DOI: [10.1080/18811248.2001.9715142](https://doi.org/10.1080/18811248.2001.9715142).
- [110] T. SZÜCS, D. BEMMERER, T. P. REINHARDT, K. SCHMIDT, M. P TAKÁCS, A. WAGNER, L. WAGNER, D. WEINBERGER AND K. ZUBER, *Cosmic-ray induced background intercomparison with actively shielded HPGe detectors at underground locations.* DOI:[10.1140/epja/i2015-15033-0](https://doi.org/10.1140/epja/i2015-15033-0).
- [111] EPIC CRYSTAL, *Plastic scintillator of Epic Crystal, Manual reference. Data sheet.*
- [112] GEANT4, *Geant4: A toolkit for the simulation of the passage of particles through matter..* Website.
- [113] THORLABS, *Guide to connectorization and polishing optical fibers,* 2006. **Manual Reference.**
- [114] INDISTROĀ˜ FIBER OPTICAL, *POF Cutter block.* Website.
- [115] DAVID SÁEZ-RODRÍGUEZ, KRISTIAN NIELSEN, OLE BANG AND DAVID JOHN WEBB, *Simple Room Temperature Method for Polymer Optical Fibre Cleaving*, Journal of lightwave technology, vol 33, No. 23, December 1, 2015. DOI:[10.1109/JLT.2015.2479365](https://doi.org/10.1109/JLT.2015.2479365).
- [116] S.H. LAW, J.D. HARVEY, R.J. KRUHLAK, M. SONG, E. WU, G.W. BARTON, M.A. VAN EIJKELNBORG AND M.C.J. LARGE, *Cleaving of microstructured polymer optical fibres.* DOI:[10.1016/j.optcom.2005.08.011](https://doi.org/10.1016/j.optcom.2005.08.011).
- [117] NANOTEC, *ST4209S1404-A - STEPPER MOTOR NEMA 17.* Data sheet.

- [118] *ARDUINO*, **Website**.
- [119] *CNC shield V3.0, Reference manual*.
- [120] *ALLEGRO Driver Pololu A4988, DMOS Microstepping Driver with Translator And Overcurrent Protection, Data sheet*.
- [121] *TEXAS INSTRUMENTS Driver DRV8825 Stepper Motor Controller IC, Data sheet*.
- [122] *Driver TMC2208, Step/Dir Drivers for Two-Phase Bipolar Stepper Motors up to 2A peak- StealthChop for Quiet Movement- UART Interface Option, Data sheet*.
- [123] ROITHNER LASERTECHNIK GMBH *LED435-03, 20 mW, 20 mA, Reference*.
- [124] , , **Reference**.
- [125] SAINT-GOBAIN CERAMICS AND PLASTICS, INC., *BC-630, Silicone Optical Grease, Website*.
- [126] THORLABS, *BK5 - Black Nylon, Polyurethane-Coated Fabric, 5'x9' (1.5m x 2.7m) x 0.005" (0.12 mm) Thick, Datasheet*.
- [127] HANNA INSTRUMENTS, *Multiparamétrico con opciones GPS, sonda autoregistradora, turbidez e ISE, Website*.
- [128] CAEN COMPANY, *Quad Scaler And Preset Counter-Timer, N1145, Datasheet*.
- [129] PHYSIKALISCH-TECHNISCHE BUNDESANSTALT, PTB, BRAUNSCHWEIG AND BERLIN, GERMANY *Calibration Certificate of tritium source, PTB-6.11-2005-1442*.
- [130] SAINT-GOBAIN CERAMICS AND PLASTICS, INC., *Scintillating Optical Fibers, It's What's Inside that Counts, 2005-14. Data sheet*.

- [131] HAMAMATSU PHOTONICS K.K., *Photomultiplier tube R2154-02 2"*. **Data sheet**.
- [132] HAMAMATSU PHOTONICS K.K., *High Voltage Power Supply C11152-01*. **Data sheet**.
- [133] MAXIM INTEGRATED, *Low-Power, Quad, 12-Bit, Voltage-Output DACs with Serial Interface*. **Data sheet**.
- [134] SAINT-GOBAIN, *Scintillating plastic grown with polymeric method*. **Data sheet**.
- [135] CREMAT INC., *CR 111-R2.1 Charge sensitive preamplifier*. **Data sheet**.
- [136] TEXAS INSTRUMENTS, *OPA656 Wideband, Unity-Gain Stable, FET-Input Operational Amplifier*. **Data sheet**.
- [137] LINEAR TECHNOLOGY, *LT111A*. **Data sheet**.
- [138] TEXAS INSTRUMENTS, *SN74AHC1G32 Single 2-Input Positive-OR Gate*. **Data sheet**.
- [139] TEXAS INSTRUMENTS, *SN74LVC1G11DBVR Single 3-Input Positive-AND Gate*. **Data sheet**.
- [140] CERN COLLABORATION, *Geant4, A simulation toolkit*. **Website**.
- [141] J. ALLISON, *Geant4 - A simulation toolkit*. DOI:[10.1016/S0168-9002\(03\)01368-8](https://doi.org/10.1016/S0168-9002(03)01368-8)
- [142] PLOT NUCLEAR DATA (NADS), *Physics simulation packages, CRY (cosmic-ray particle showers)*. **Website**
- [143] CHRIS HAGMANN, DAVID LANGE and DOUGLAS WRIGHT, *Cosmic-Ray particle Showers Generator (CRY) for Monte Carlo Transport Codes*, IEEE Nuclear Science Symposium conference

- record. Nuclear Science Symposium 2:1143-1146, January 2007.  
**DOI:10.1109/NSSMIC.2007.437209**
- [144] H. BUITEVELD, J.H.M. HAKVOORT, M. DONZE, *Optical properties of pure water, in: Proc. 2258 Ocean Optics XII, Bergen, Norway, 1994.*  
**DOI:10.1117/12.190060**
- [145] S. MAERTENS, ET AL., *Sensitivity of next-generation tritium beta-decay experiments for keV-scale sterile neutrinos, J. Cosmol. Astropart. Phys. 2015 (2015) 020.* DOI:10.1088/1475-7516/2015/02/020
- [146] J. ARGYRIADES, ET AL., *Spectral modeling of scintillator for the NEMO-3 and SuperNEMO detectors, Nucl.Instrum. Methods A 625 (2011) 20-28.*